UNIVERSITÀ POLITECNICA DELLE MARCHE
DIPARTIMENTO DI INGEGNERIA INDUSTRIALE E SCIENZE MATEMATICHE
CORSO DI DOTTORATO DI RICERCA IN SCIENZE DELL'INGEGNERIA
CURRICULUM IN ENERGETICA

Study and development of a web-based software for hybrid energy system design and solar prediction analysis

Ph.D. Dissertation of:
Gloria Puglia

Advisor:
Prof. Gabriele Comodi

Curriculum Supervisor:
Prof. Ferruccio Mandorli

XV edition - new series

UNIVERSITÀ POLITECNICA DELLE MARCHE
DIPARTIMENTO DI INGEGNERIA INDUSTRIALE E SCIENZE MATEMATICHE
CORSO DI DOTTORATO DI RICERCA IN SCIENZE DELL'INGEGNERIA
CURRICULUM IN ENERGETICA

Study and development of a web-based software for hybrid energy system design and solar prediction analysis

Ph.D. Dissertation of:
Gloria Puglia

Advisor:
Prof. Gabriele Comodi

Curriculum Supervisor:
Prof. Ferruccio Mandorli

XV edition - new series

UNIVERSITÀ POLITECNICA DELLE MARCHE
SCUOLA DI DOTTORATO DI RICERCA IN SCIENZE DELL'INGEGNERIA
FACOLTÀ DI INGEGNERIA
Via Breccie Bianche – 60131 Ancona (AN), Italy

Acknowledgements

Un sentito ringraziamento va:

Al Professor Gabriele Comodi, per avermi guidato in questo percorso di dottorato.

Ai colleghi dottorandi (e non) che mi hanno accompagnato durante questo percorso, rendendo leggero e sostenibile ogni sforzo di lavoro, anche il più difficile.

Ai colleghi della Moroni&P., per avermi dato la possibiltà di portare avanti questo lavoro.

Abstract

The challenge of integrating fluctuating power from renewable energy sources in the electricity grid cannot be looked upon as an isolated issue but should be seen as one out of various means and challenges of approaching sustainable energy systems. The presented PhD thesis project illustrates the analysis, study and development of a web-based software able to design hybrid energy systems composed of photovoltaic plant, storage and backup systems in any location of the world, able improve the reliability, availability and sustainability of both grid-connected and isolated energy systems. The software EHS (Energy Hybrid System) is programmed to evaluate the optimal design for various configuration of energy hybrid systems. The evaluation of the optimal hybrid system configuration is based on the value of the LCC (Life Cycle Cost) calculated along the potential lifetime of the entire system considering all the future costs. The thesis presents a design case study, carried out through EHS software, of a hybrid power system located in Uganda. The results of the simulation through the software EHS show that the usage of battery storage is economically crucial. Results disclose that the optimal configuration of the hybrid system (PV-storage-diesel generators), despite its high investment cost, presents an economic benefit of 25.5 and 22.2% compared to the usage of only PV array and diesel generators and only diesel generators and a reduction of fuel consumption equal to 74.7 and 77%, respectively. In order to improve the hybrid energy system efficiency, the thesis project also proposes a development of an instrument able to make a reliable prediction of PV production and a solar irradiance forecast methodology to predict the photovoltaic production through an experimental instrument called "solar predictor". Within this study a sky image system, based on a commercial digital camera, has been used and characterised with respect to get image elaboration, cloudy shape detection, motion estimation and tracking.

Contents

List of Figures

List of Tables

1

Introduction

The Renewable Energy Sources (RES) include any naturally occurring, theoretically inexhaustible source of energy, as solar, biomass, wind, tidal, wave, and hydroelectric power, that is not derived from fossil or nuclear fuel.

During the last decades, renewable energy has been considered as one of the strong contenders to improve the lives of billions of people across the world and ensure a more sustainable future by working to achieve three global objectives: (i) universal access to energy, (ii) doubling of the rate of improvement in energy efficiency, and (iii) doubling of the share of renewable energy in the global energy mix [1]. Nowadays 1.1 billion of people have such limited or unreliable access to electricity [1] and it must be kept in mind that these people live in regions of the world where the population is growing most rapidly [2]. When people have no access to electricity, even a small wind turbine or a low wattage photovoltaic panel combined with battery storage can make a very large difference in the quality of their lives. Many experts now argue that technologies such as solar, wind, and small-scale hydropower are not only economically viable but also ideal for rural areas. Renewable energy technologies (RETs) are cost-competitive with conventional energy sources in applications such as solar water heating, off-grid electrification with solar photovoltaics (PV), small-scale biomass power generation, biofuels, grid-connected and off-grid wind power, small hydropower, geothermal power, and methane utilisation from urban and industrial waste [2].

Despite technological developments and economic viability for several applications, renewable energy has been tapped only to a small fraction of its potential. This is due to the existence of several types of barriers to the penetration of renewable energy. Raising the share and the penetration of RES is a crucial aim for the policy agenda in countries around the world. Several governments have set ambitious targets and have started to implement support schemes aimed at facilitating market

implementation. The EU Heads of State and Government set a series of demanding climate and energy targets to be met by 2020, 2030 and 2050 [3] :

1. Targets for 2020:
    - A reduction in EU greenhouse gas emissions of at least 20% below 1990 levels
    - 20% of EU energy consumption to come from renewable resources
    - 20% reduction in primary energy use compared with projected levels, to be achieved by improving energy efficiency.
2. Targets for 2030:
    - A reduction in EU greenhouse gas emissions of at least 40% below 1990 levels
    - 27% of EU energy consumption to come from renewable resources
    - A 27-30% reduction in primary energy use compared with projected levels, to be achieved by improving energy efficiency.
3. Targets for 2050:
    - A reduction in EU greenhouse gas emissions of at least 80-95% below 1990 levels

Furthermore, the Roadmap 2050 project, founded by the European Climate Foundation (ECF) in 2009, set out four main routes to a more sustainable, competitive and secure energy system in 2050: (i) energy efficiency, (ii) renewable energy, (iii) nuclear energy and (iv) carbon capture and storage. The Roadmap 2050 project finds that a fully integrated Internal Energy Market in combination with a functioning Emissions Trading System is the most cost-effective and sustainable pathway to decarbonisation. However, policy makers need to take bold action to turn this vision into reality, by driving physical interconnections, activating the demand side, regionalising system operation and steering investments from high to low carbon assets. In the meantime, well-designed market interventions to support renewable technologies, energy efficiency and resource adequacy remain necessary.
Several barriers that have prevented penetration of RETs exist, these include cost-effectiveness, technical barriers, and market barriers such as inconsistent pricing structures, institutional, political and regulatory barriers, social and environmental barriers. Some barriers may be specific to a technology, while some may be specific to a country or a region.
One of the most promising RETs is the photovoltaic (PV) technology. PV systems are popularly configured as: (i)stand-alone, (ii) grid-connected, and (iii)hybrid systems. They are developing rapidly in the world, both in the developed and developing nations. In any PV system, sizing represents an important part of PV systems design, i.e. the optimal selection of the number of solar cell panels, the size of the storage battery and the size of wind- generator to be used for certain applications at a particular site is an important economical task for electrification of villages in rural areas, telecommunications,

refrigeration, water pumping, and water heating. Besides being an economic waste, an oversized system can also adversely affect further utilisation of solar cells and the pollution-free PV energy. Undoubtedly, at the present stage of the development of PV technology, the major impediment to a wider market penetration is the high investment costs of the PV systems. However, estimation of the sizing parameters PV-array area, useful capacity of battery, wind generator is very useful to conceive an optimal PV systems as well as conceiving an optimal and economic PV systems particularly in isolated sites (Sahara regions, small island archipelagos, remote areas in developing nations, mountainous locations, rural regions, etc.). Concerning energy hybrid energy systems, they use different energy resources such as solar and wind energy and diesel gen-sets and they are an economical option in areas isolated from the grid. The implementation of hybrid systems in isolate and remote rural regions can not only improve the standard of living and the economic growth of the entire region but can also reduce the greenhouse gas emissions, encouraging the environmental respect and reducing the health habitants expectations compared to the diesel generators based energy systems. Furthermore, the total absence of electric grid plants in remote villages offers an easier implementation of new grid systems and renewable energy integration compared to those places where grid connections and power plants already exist.

While some studies that look at more sectors as part of the path towards 100% renewable energy systems, including electricity, heat and transport have already been developed [4–9], there is still a predominant sectorial focus on how to integrate fluctuating resources into the electricity sector [10]. More and more focus is being placed on energy savings, renewable energy sources and the handling of fluctuating renewable energy sources. While electricity savings should be promoted heavily, an increasing focus is placed on the integration of fluctuating renewable energy into the electricity system to lower emissions [11–16]. For example, the smart grid community has a strong focus on the use of the following components: ICT, smart meters and smart grids connected to existing electricity demands, EV's and individual heating technologies [10, 17–22], flexible demand, storages and electricity storage, distributed generation [23, 24], power-to-gas [25] and transmission [26, 27]. Some authors are also connecting the smart grids to the concept of smart cities, but continues to have a focus on the electricity grid only and/or on individual buildings [28–30]. Only very few authors look at the transition as a complete redesign of the whole system [10, 17].
The issue of RES fluctuation and the inability of programming their production, generated a wide scientific research field on RES penetration but how this objective can be reached in the future and what the future power system will look like is, however, not fully clear. Many research projects, shown how the implementation of hybrid energy systems with storage may reduced the negative effect of RES fluctuation and ensure a well-balance demand-response load profile [31–33]. In [34] is underlined the importance of the load shifting effect. The customers' electricity bill consists of energy payments and power demand payments. The latest correspond to the highest power demand during a specific time period. Load shifting operation offers to the customers a way to more effectively

manage the cost of their electricity bill. This can be accomplished letting power users take advantage of the relatively low cost of the electricity during off–peak demand periods and generate their own power (through a storage source) during peak periods, when electricity energy prices are high, also avoiding high demand charges. A secondary effect of load shifting is peak-shaving. Peak shaving has been practiced, until now, by using gas turbines or diesel generators. However, today industrial users or public facilities can take advantage of battery systems capable of discharging for short periods of time during on–peak hours and charging during off–peak demand periods, also reducing peak demand charges. This application could also yield other key benefits including a reduced charge on transmission and distribution (T&D) systems and a reduced need for peak generation.

Concerning areas far from the electric grid, over the past years, the electrification of isolated rural areas has acquired more and more interest; several studies on hybrid power systems have been implemented in order to prove their higher reliability and lower cost of generation compared to power systems that employ only one source of energy. Simultaneously at the researches focused on hybrid systems connected to the electricity grid [35–37], some other studies analysed the impact of hybrid systems in isolated areas that are not reached by the grid. Some of these works presented by [38–41] analysed the implementation of hybrid power systems through the usage of H.O.M.E.R. (Hybrid Optimization Model for Electric Renewable), [42]. This tool is a micro-grid modelling software widely used to determine the technical feasibility and to perform the economical analysis of both on- and off-grid power systems. Two different types of battery dispatch strategy exist within HOMER software: *i)* the *load-following*, where the battery bank is re-charged by the exceeded PV production and the generators work only to supply the electric load and *ii)* the *cycle-charging*, where generators operate at their maximum rated power, producing extra-power that re-charges the electric storage until its nominal capacity. For instance, [38] used the software HOMER to find out that the PV-battery-diesel hybrid system using the *load-following* strategy is an economically optimal solution for a stand-alone electricity generating system in rural and semi-urban areas in the Northern part of Nigeria. Also [39] used HOMER to analyse the potential implementation of hybrid system in a southern city of Malaysia, showing that the *load-following* strategy is more suitable because of the reduction of total net present cost and of the excess electricity produced compared to the *cycle-charging* strategy. [40] simulated the dimensioning process of an stand-alone hybrid power system in Australia by the usage of two different tools: HOMER and HYBRIDS, highlighting the difference, advantages and disadvantages of the two software, [43]. In both cases the optimisation of the power system is based on the value of NPC (Net Present Cost) and on the fraction of energy supplied from renewable sources, RF (Renewable Fraction). [40] implemented the *cycle-charging* strategy, which is preferred for large scale systems, since it promotes the generators longevity, reducing the start&stop processes and electric storage lifetime, decreasing the risk of over-discharging.

[41] used HOMER to dimension an optimal PV-battery-diesel power system configuration as a replacement of an existing diesel power plant used to supply a remotely located population in Saudi Arabia.

Nevertheless, beyond the HOMER applications, some other works concerning the rural electrification were carried out. [44] implemented a model called Network Planner that algorithmically generates a comprehensive, cost-optimised electricity plan considering different technology options. This model was applied to many un-electrified communities in Ghana within a 10 years planning period. [45] developed a model to find out the optimal size of grid independent PV-battery-diesel based hybrid energy system in remote villages of Uttar Pradesh in India. The objectives of the work were to minimise the Life Cycle Cost and to reduce the CO_2 emissions from the system.
Concerning the smart-grid system and implementation of RETs, part of this thesis project points out how important is to be able to build energy systems based on the real request of supplied energy and to maximise the self consumption of energy decreasing the costs of grid duties and avoiding imbalance in the grid, especially during the distribution phase.
One of the elements that may be useful to reach this goal is the development of an instrument able to make a reliable prediction of PV production. Meteorological conditions are decisive in solar plant management and electricity generation. Any increases or decreases in solar radiation mean a plant has to adapt its operation method to the climatological phenomena. An unexpected atmospheric change can provoke a range of problems related to various solar plant components affecting the electricity generation system and, in consequence, causing alterations in the electricity grid. Therefore, predicting atmospheric features is key to managing solar plants and is therefore necessary for correct electrical grid management. For large scale solar applications, the amount of irradiance reaching the ground surface is most strongly affected by clouds, aerosols and water vapor column, with cloud effects being particularly dominant for most locations where solar power is currently produced. Different solar irradiance forecast methodologies have been proposed for various time horizons. For the forecast-ing horizon of same-day to a few days ahead, NWP models have been evaluated in various locations[46–48]. For time horizons of 1–6 h, satellite-based forecasts are competitive with NWP models [46] and, in addition to these physical model/image processing-based models, time series-based solar forecasting methods have also been extensively applied, [49–59] and validated over wide ranges of time horizons. Some of the most important work have been deeply analysed and new solar irradiance forecast methodology has been proposed and the instrument that this study aims at developing is called solar predictor.

The present PhD thesis project aims to present a software able to design hybrid energy systems composed of photovoltaic plant, storage and backup systems in any location of the world, able improve the reliability, availability and sustainability of both grid-connected and isolated energy systems. Energy hybrid systems are best suited to reduce dependence on fossil fuel by using available solar radiation and they can be divided in on-grid (or grid-connected) and off-grid systems. On-grid systems includes the PV generator, storage system grid connection and off-grid systems include PV generator, storage system and a backup system. Battery storage increases the flexibility of system control and adds to overall system availability. These energy systems are termed as one of the cost effective

solutions to meet energy requirements of remote areas. The reason behind the project is that an optimum combination of the hybrid energy system provides higher system performance than a single system, for the same system cost and battery storage capacity. It was also observed that the magnitude of the battery storage capacity has important bearing on the system performance of single PV energy systems and an optimised design can be pivotal in the system cost reduction.
The thesis project also proposes a development of an instrument able to make a reliable prediction of PV production and a solar irradiance forecast methodology to predict the photovoltaic production through an experimental instrument called "solar predictor". Within this study a sky image system, based on a commercial digital camera, has been used and characterised with respect to get image elaboration, cloudy shape detection, motion estimation and tracking. An unexpected atmospheric change can provoke a range of problems related to various solar plant components affecting the electricity generation system and, in consequence, causing alterations in the electricity grid and storage systems. Therefore, predicting atmospheric features is key to managing solar plants and is therefore necessary for correct electrical grid management. The current impossibility of predicting the supplied energy leads to the necessity to find out an instrument to predict the solar radiation with a small margin of error compare to the existing ones.
Making prediction on photovoltaic production, storage operating life, diesel cost, interest rate trend, and electric load demand over a period of 20-25 years seems ambitious and far from reliable results. Indeed the aim of the project lies in achieving optimal solution for renewable energy systems considering every current economical, social, geographical, and political factor without keeping out the possibility to conform the energy system with future requirements. For instance the project does not exclude the chance to extend the current system with modular system parts in order to satisfy a potential higher electric demand or to substitute system components with more advanced and high efficient ones. Concerning political factor, i.e. diesel cost and interest rate, sensitivity analysis has been carried out at the end of the study in order to understand the impact of these critical parameters variation on the optimal proposed model. Furthermore, compared to the past studies, this work analyses the power system by running a 15 minutes step simulation for one year, in order to evaluate the supply reliability of the system within shorter time step, and therefore to investigate the renewable energy (RE) criticality. The choice of the short time interval is moreover strictly connected with the potential implementation of a solar predictor within the hybrid system, able to forecast the weather conditions within short time period and to supply pivotal information to the final users concerning an optimal usage of stored energy.

A complete set of match calculation methods for optimum sizing of hybrid system is shown in Chapter 2, the EHS software is described with all its functions in Chapter 3, the results obtained for real study case and the sensitivity analysis on some critical parameters are shown in Chapter 4. The final section of this work describes the research activity focused on the solar predictor development an its applicability within an hybrid energy system or smart grid system, Chapter 5. Eventually, conclusion and future work are expose in Chapter 6.

2

Methodology

The presented thesis project focuses on the evaluation of the optimal hybrid system design. The considered energy systems and their main components are listed below:

- On-grid system with storage system (PV system, storage system, electric grid and backup system)
- On-grid system without storage system (PV system, electric grid and backup system)
- Off-grid system with storage system (PV system, storage system and backup system)
- Off-grid system without storage system (PV system and backup system)

Each component and its power production of the chosen hybrid energy system is evaluated according to the methodology presented in this chapter. The first evaluation concerns the solar radiation related at the geographic location where the hybrid energy system has to be designed. The data of the available solar radiation allow to estimate the supplied PV energy to the users depending on the size and the type of chosen PV plan. In the systems with storage, the size of the battery is estimated depending on the PV production and on the technical features of the chosen battery technology. Eventually, in the isolated system not reached by the electrical grid, the size of the backup system is evaluated considering the PV production, the capacity of the battery system and its potential energy supply.
The potential configurations of the hybrid power system are carried out with the backup system of diesel generators selected according to Section 2.3, 25 different photovoltaic array sizes, 25 different capacities of battery storage. The 25 simulated PV array sizes range between a minimum and a maximum value of nominal power expressed in kWp, corresponding to the 10 % and the 400 % of the maximum electrical peak load, respectively. The 25 simulated battery capacities vary between a

minimum and a maximum value of capacity expressed in kWh, that correspond to the 10 % and 150 % of the mean daily electrical consumption, respectively. This range, as the PV array size one, is selected following preliminary tests that have been performed in order to find out the more acceptable and reasonable values to simulate the optimal electric storage design. The diesel generators combinations are chosen within a database of 19 generators and they are carried out from the model exposed in Section 2.3.

The chapter presents three main sections concerning solar radiation evaluation and PV production, electric storage and backup systems. Section 2.1 presents the theory behind the solar radiation and photovoltaic production. The first part of this section illustrates the equations used to evaluate the solar radiation, the solar radiation on tilted surfaces and the fraction of beam solar radiation on tilted surfaces. The second part of Section 2.1 gives an overview on photovoltaic system technologies and illustrates the equation used within this study to evaluate the photovoltaic production. Section 2.2 explains the importance of the storage systems role in energy systems and presents the main current storage system technologies. Furthermore it presents in detail the chemical energy storage technologies providing information about economic and technological features of each type of battery. The last part of Section 2.2 illustrates the equations of charging and discharging process of batteries. In Section 2.3 the working principles of the backup system are explained and, eventually, the second part of this section presents an in-depth analysis of diesel generators, their operation and the equations used within this study to design an optimal backup system size.

2.1 Solar Radiation and Photovoltaic Systems

The sun is the most important energy source for the earth. At the center of the sun it takes place a fusion process in which two hydrogen nuclei fuse into a helium nucleus and the energy thus released is radiated into space in the form of electromagnetic waves. The solar energy propagates symmetrically in space and half a billionth of this energy invests the outer layer of the atmosphere of the earth. The total power radiated at the surface of the sun is more than $60'000\ kW/m^2$ and it decreases with increasing distance. At the distance of $143 \cdot 10^6\ km$, which separates the earth from the sun, the radiated power takes on a much smaller value that is named *solar constant* and it is theoretically considered equal to $1.367\ kW/m^2$. The considered value of the solar constant is a reference value since the radiated power oscillates because of the earth-sun distance yearly variation and the solar activity fluctuations. Variation of the earth-sun distance, however, does lead to variation of extraterrestrial radiation flux in the range of $\pm 3.3\%$, [60]. A simple equation with accuracy adequate for most engineering calculations is given by 2.1a, while [60] provides a more accurate equation ($\pm 0.01\%$) in the form of 2.1b.

$$G_{on} = \begin{cases} G_{sc}\left(1 + 0.033\, cos\frac{360n}{365}\right) & \text{(2.1a)} \\ G_{sc}(1.000110 + 0.034221\, cos B_n + 0.001280\, sin B_n & \\ \qquad + 0.000719\, cos 2B_n + 0.000077\, sin 2B_n) & \text{(2.1b)} \end{cases}$$

where G_{on} is the extraterrestrial radiation incident on the plane normal to the radiation on the n^{th} day of the year and B_n is given by Equation (2.2).

$$B_n = (n-1)\frac{360}{365} \tag{2.2}$$

Solar radiation at normal incidence received at the surface of the earth is subject to variations due to change in the extraterrestrial radiation and to two additional and more significant phenomena: (i) atmospheric scattering by air molecules, water, and dust and (ii) atmospheric absorption by O_3, H_2O, and CO_2. Generically, the relevant regulations assume the value of about $1\,kW/m^2$ as maximum value of instantaneous available solar radiation at the ground.

2.1.1 Evaluation of solar radiation

The extraterrestrial radiation that reaches the atmosphere of the earth on a normal surface to the solar radiation direction at any time between sunrise and sunset is evaluated through Equation (2.3), and it is given by [60].

$$G_o = 1.367\left(1+0.033\,cos\frac{360n}{365}\right)(cos\phi\,cos\delta\,cos\omega + sin\phi\,sin\delta) \qquad (kW/m^2) \tag{2.3}$$

Within this study, the value of the extraterrestrial radiation on a normal surface is obtained by integrating Equation (2.3) over 15 minutes in order to observe the solar radiation within a defined time period. The extraterrestrial radiation at day n, latitude ϕ, and time step i is therefore calculated through Equation (2.4).

$$He(i) = 12\frac{3600}{900}\frac{1.367}{\pi}\left(1+0.033\,cos\frac{360n}{365}\right)(cos\phi\,cosd\delta\,sin\omega(i) - sin\omega(i)) + sin\phi\,sin\delta\left(\frac{\pi}{180}(\omega(i)-\omega(i-1))\right) \qquad (kW/m^2) \tag{2.4}$$

where δ is the declination defined as the angular position of the sun at solar noon with respect to plane of the equator, north positive ($-23.45^\circ \leq \delta \leq +23.45^\circ$) and expressed by Equation (2.5)

$$\delta(n) = 23.45\,sin\left(360\frac{284+n}{365}\right) \tag{2.5}$$

and $\omega(i)$, at the i^{th} time step, is the angular displacement of the sun east or west of the local meridian due to rotation of the earth on its axis at 3.75° every 15 minutes; morning negative, afternoon positive ($-180^\circ \leq \omega \leq +180^\circ$).

The amount of solar energy that reaches the surface of the earth depends on various factors: insulation (solar exposition hours of the earth's surface), latitude, and position of the earth relative to

the sun (specific season, day and hour). The solar radiation that reaches the atmosphere is divided into two components:

- Beam radiation (B): the solar radiation received from the sun without having been scattered by the atmosphere.
- Diffuse (D): the solar radiation received from the sun after its direction has been changed by scattering in the atmosphere.

The sum of the beam and diffuse radiation measured on an horizontal surface on the earth is named global radiation G.
In order to split the total solar radiation on a horizontal surface into its diffuse and beam components, the fraction of diffusive radiation on a horizontal plane D/G is correlate with the clearness index k_T. The clearness index is defined by the ratio between the global radiation G at the ground and the extraterrestrial radiation and, within this study, is evaluated at 15 minutes time step. it expresses

$$k_T = \frac{G}{He} \tag{2.6}$$

The diffuse component D and the beam component B of solar radiation are given by:

$$D = \frac{D}{G}G, \qquad B = G - D \tag{2.7}$$

where the fraction D/G is calculated at 15 minutes time step by using the correlation proposed by Erbs et al. [61]:

$$\frac{D}{G} = \begin{cases} 1.0 - 0.09k_T & \text{for } k_T \leq 0.22 \\ 0.9511 - 0.1604k_T + 4.388k_T^2 - 16.638k_T^3 + 12.336_T^4 & \text{for } 0.22 < k_T \leq 0.80 \\ 0.165, & \text{for } k_T > 0.8 \end{cases} \tag{2.8}$$

2.1.2 Evaluation of solar radiation on tilted surfaces

Considering a tilted surface, such as photovoltaic system, solar collectors, and other passive system receivers, the directions from which the beam and diffuse components reach the surface in question are needed in order to evaluate the global radiation. The direction from which diffuse radiation is received and its distribution over the sky dome are function of conditions of cloudiness and atmospheric clarity, which are highly variable. Some sky models have been proposed in literature as mathematical representations of the diffuse radiation. Three of the most useful sky models are listed below:

- Isotropic sky, received uniformly from the entire sky dome.
- Circumsolar diffuse (anisotropic sky), resulting from forward scattering of solar radiation and concentrated in the part of the sky around the sun.

- Horizon brightening (anisotropic sky), is concentrated near the horizon and is most pronounced in clear skies.

The presented work assumes the isotropic diffuse model derived by Liu and Jordan in 1963, [62], where the radiation on the tilted surface is considered to include three components: (i) beam, (ii) isotropic diffuse, and (iii) solar radiation diffusely reflected from the ground. The choice of the isotropic sky model is due to the fact that it is easy to understand, conservative (it tends to underestimate the total radiation on the tilted surface) and makes calculation of radiation on tilted surfaces easier compared to the other two sky models, [62].

The total solar radiation on a tilted surface, R_{tot}, is obtained by summing the three components of beam, diffuse and reflected radiation as follows:

$$R_{tot} = BR_b + DR_d + (B+D)R_r \qquad (W/m^2) \tag{2.9}$$

where R_b, R_d and R_r are the fraction of beam, diffuse and reflected radiation on the tilted surface.

The ratio of beam, diffuse and reflected radiation that invests a surface depends on three main factors:

- Weather conditions: during a cloudy day, the radiation is manly diffuse, whereas, during a clear and sunny day, the beam component prevails and it can reach the 90% of the total solar radiation.

- Presence of reflective elements: the ability of an element to reflect solar radiation towards the outside is measured through a coefficient called *albedo* (ρ_g). The albedo varies depending on the material of the element and as a rule, when no measure is specified, its value is assumed equal to 0.2. The largest contribution to increment the reflected component of radiation is given by white, clear and bright surfaces; for instance the reflected component increases with the snow presence and decreases in summer for dark colours absorption effect as that of the grass or the ground.

- Tilt and orientation of the surface: considering the variation of the angle of incidence of the solar radiation during the day and the entire year, it is possible to maximise the value of captured radiation in some periods of the year if the receiving surface is tilted at a certain angle β with respect to the horizontal plane (value which depends on the latitude), and orientated at a certain angle γ with respect to the south direction.

A tilted surface with slope β from the horizontal has a view factor to the sky $F_{c-s} = (1+cos\beta)/2$ and, within the isotropic sky model, it corresponds to the ratio of diffuse on the tilted surface to that on the horizontal surface R_d. The tilted surface has a view factor to the ground equal to $F_{c-g} = (1-cos\beta)/2$, and defining ρ_g as the diffuse reflectance of the surrounding ground (albedo),

the fraction of the reflected radiation from the surroundings on the surface is $\rho_g(1-cos\beta)/2$. Therefore, the Equation (2.9) can be written as:

$$R_{tot} = BR_b + D\left(\frac{1+cos\beta}{2}\right) + (B+D)\rho_g\left(\frac{1-cos\beta}{2}\right) \tag{2.10}$$

2.1.3 Evaluation of fraction of beam radiation on tilted surfaces

Considering a surface tilted at an angle β and orientated at a surface azimuth angle γ. The ratio of beam radiation on the tilted surface to that on a horizontal surface at any time, is given by [60]:

$$R_b = \frac{B_T}{B} = \frac{\cos\theta}{\cos\theta_z} \tag{2.11}$$

and $\cos\theta$ and $\cos\theta_z$ are determined from Equations (2.12) and (2.13), respectively [60].

$$\begin{aligned}\cos\theta = \sin\delta\sin\phi\cos\beta - \sin\delta\cos\phi\sin\beta\cos\gamma + \cos\delta\cos\phi\cos\beta\cos\omega + \\ + \cos\delta\sin\phi\sin\beta\cos\gamma\cos\omega + \cos\delta\sin\beta\sin\gamma\sin\omega\end{aligned} \tag{2.12}$$

$$\cos\theta_z = \cos\phi\cos\delta\cos\omega + \sin\phi\sin\delta \tag{2.13}$$

Equations (2.12) and (2.13) mean at any time of the day except at the solar noon, when the solar angle ω equals to zero. In [60] the estimation of the ratio of beam radiation on tilted surface to that on horizontal surface at solar noon is defined for the northern hemisphere as:

$$R_{b,noon} = \frac{\cos|\phi-\delta-\beta|}{\cos|\phi-\delta|} \tag{2.14}$$

and for the southern hemisphere as:

$$R_{b,noon} = \frac{\cos|-\phi+\delta-\beta|}{\cos|-\phi+\delta|} \tag{2.15}$$

Equations (2.4) to (2.15) have been used within this study in order to evaluate the solar radiation received by photovoltaic plants and to estimate the productivity of these systems at any latitude, tilt, orientation, climate and surrounding conditions.

2.1.4 Photovoltaic systems

Through the photovoltaic effect the solar radiation is directly transform into electric energy by taking advance of the interaction between the light radiation and valence electrons of semiconductor materials. The photovoltaic effect is an intrinsic feature of these materials and the most used for this purpose are listed below:

- Silicon (Si)
- Germanium (Ge)
- Galium Arsenide ($GaAs$)
- Cadmium sulfide (CdS)
- Copper sulfide (Cu_2S)
- Multiple-junction cells (Tandem)

Nevertheless, about the 94% of photovoltaic cells on the market is made with silicon semiconductor. This material, compared to the others, presents many advantages:

- It has almost unlimited availability: over 90% of the surface of the earth is composed of silicate minerals, making silicon the second most abundant element in the earth, about 28% by mass, after oxygen.
- Silicon is widely used in the electronics industry (technological processes of refining and processing)
- It can be recycled from waste of electronics industry since the photovoltaic industry tolerates concentrations of impurities typically around $10^{-5} \div 10^{-6}$ against the values of $10^{-8} \div 10^{-9}$ related to the electronics industry.

Three main technologies of silicon cells exist on the market, they differ in molecular composition, efficiencies and costs:

- Monocrystalline silicon PV panels. It is the most efficient, though the most expensive and it presents an average efficiency of 15%.
- Polycrystalline silicon PV panels. This technology presents efficiency about 13%, because of an irregular molecular structure, but lower manufacturing time and costs.
- Amorphous silicon. Efficiency about 6%, it is a thin film with low manufacturing costs. It is applicable to various forms of economic support due to its flexibility (i.e. roof tiles and curved surfaces)

Generally, the efficiency of commercial monocrystalline and polycrystalline PV cells varies between 13% and 17%, even though, in the laboratory, it can reach the value of 32.5%. The low efficiency of PV panels is due to many factors as reflection of solar radiation on the surface, too much or too little photons energy, ambient temperature and electrical resistances.
Concerning the structural features of PV system, they can be or fixed-tilt systems (with a fixed structure) or tracking systems, with single or double axis tracking systems characterised by step

motors and control electronics.
PV systems, depending on their electric characteristics, can be divided into two categories:

- *Isolated* or *stand alone* or *off-grid* systems in which the PV energy feeds directly into an electrical load and the excess is usually stored in a storage system or wasted instead.

- *Grid connected* or *on-grid* systems in which the energy is converted into AC to supply the user load and/or introduced into the electric grid, with which the system works on an interchange regime.

The amount of electricity supplied by a PV system depends on three main factors: (i) available solar radiation, (ii) cell efficiency and size of the plant, and (iii) efficiency of BOS (Balance Of System). The characteristics and values of these factors are explained below.

- The available solar radiation has a variable value depending on several parameters: (i) the distance and position relative to the Earth-Sun, depending on the specific day of the year and time of the day; (ii) the Earth's atmosphere influence (absorption, reflection, refraction); and (iii) the position of the PV modules: tilt angle (β) and orientation angle or azimuth (γ).

- The cells efficiency (η_m) is defined as the ratio between the produced electric power and the available solar radiation at standard conditions of $1000\,W/m^2$ and ambient temperature equals to 25°C. The peak power production is than expressed as:

$$P_{peakpower} = \eta_m \cdot P_{stc} \cdot A \qquad (kW_p) \tag{2.16}$$

  where, P_{stc} is the solar radiation at standard conditions ($1000\,W/m^2$) and A is the area of the panels measured in m^2. This means that with a modules area of 8 m^2 and efficiency of 12.5 %, the system produces 1 kW_p.

- The overall efficiency is eventually affected by electronic components needed to transfer the power produced by the PV modules to the users. This efficiency is called BOS (Balance Of System) efficiency (η_{BOS}) and it takes into account the electrical losses in the inverter / converter, in the lines and electronic components. Common values of η_{BOS} range from 75% to 80%.

2.1.5 Evaluation of PV production

The evaluation of PV power production is evaluated through Equation (2.17) and it states the kWh supplied by the system for each installed kWp. This equation is than used to estimate the production

for any size of PV system.

$$PV_{prod} = R_{tot}\, PV_o\, \eta_m\, \eta_{BOS} \quad \left(\frac{kWh}{kWp}\right) \tag{2.17}$$

where, PV_{prod} is the PV power production, R_{tot} is the available solar radiation evaluated for the specific tilted surface through Equation (2.9), PV_o is the panels occupancy expressed in m^2/kWp, η_m is the cells efficiency, and η_{BOS} is the Balance Of System efficiency. The BOS efficiency refers to the components and equipment that move DC energy supplied by solar panels through the conversion system which in turn produces AC electricity. Most often, it refers to all components of a PV system other than the modules. In addition to inverters and racking, it includes the cables/wires, switches, enclosures, fuses and ground fault detectors. This efficiency is applied to all types of solar applications. Equation (2.17) is evaluated by integrating, within a defined time step, Equation (2.9). The values of PV_{prod} are needed to evaluate the photovoltaic energy released from different size of PV array at any time step of the day.

2.2 Electric Storage

Storage systems are considered a pivotal technology to achieve the european climate targets and Energy Roadmap 2050 goals. The growing penetration of RES, especially fluctuating sources as solar and wind power, will increase the need of a more flexible energy system.
Storage systems, ensuring a constant and reliable energy supply at any moment, are particularly compatible to meet the future climatic challenges. It has been estimated that storage systems will supply fundamental services to the entire chain that sets up the final energy price and they will support the transition to a safe, competitive and fossil sources independent european energy system, [63]. The main reasons behind the ability of storage systems at being a fundamental tool to improve the electric grid system are listed below:

- Balance of demand-response: the increase of power production variability, due to the increase of RES, requires new strategies and technologies to balance the electricity demand-response.
- T&D management: some studies [64] confirmed that even through the usage of the most modern transmission systems, storage systems will become an essential tool to stabilise the future electrical grid.

The need to support the storage systems penetration is due to the requirement to achieve a more flexible and stable electric grid in order to overtake some current difficulties, as the increase of peak-load and, as the same time, the increase of variability due to RES penetration. Furthermore, storage systems penetration might lead to a decrease in economic cuts on the RES by limiting the fossil sources dependence and improving the payback time of RES investments. Looking at the future, storage

systems will not be requested only for electric grid usages but also for transport and air-conditioning sectors.
Energy storage systems include many different technologies, some of the most relevant according to the European Association for Storage of Energy (EASE) [63] are listed below:

- Chemical energy storage
- Electrochemical energy storage (batteries and electrochemical capacitors)
- Mechanical energy storage (compressed air, flywheel and hydro)
- Thermal energy storage
- and, as a potentially future applicable technology, Superconducting Magnetic Energy Storage (SMES).

Within the presented PhD thesis project, a deep study as been done on battery technology and the study applications consider batteries as storage system because of their easier data availability and wider shared knowledge of the technology. Nevertheless the choice of batteries as storage systems, any other previous listed technology can be substitute for battery and used as storage in energy hybrid systems.

2.2.1 Batteries

Batteries are electrochemical energy storage devices based on a variety of different specific chemical systems. Today the most commonly used technologies, available on the market, are the followings:

- Lead-based: Lead acid, advanced lead acid.
- Lithium-based: Li-ion (Lithium ion).
- Nickel-based: $NiCd$ (nickel cadmium), $NiMH$ (nickel metal hydride).
- Sodium-based: NaS (sodium sulphur), ZEBRA (sodium nickel chloride, $NaNiCl_2$).

According to [65], batteries have been practically utilised as convenient power sources for about two centuries and the application range of rechargeable batteries has been dramatically expanding over the latest decades because of increasing demand for stationary and mobile power sources in numerous appliances and other devices, e.g. smart grid system and off-grid energy system.
Batteries are based on single electrochemical cells each having voltages in the range from below 1 V up to about 4 V. The cells can be combined in series to yield very high voltages if required. Batteries hold highly attractive power densities and their round cycle efficiency (electrical energy out over electrical energy in) is generally high, in the range up to 70-95%, depending on charge and discharge conditions. Electrochemical batteries consist of two or more electrochemical cells. The cells use

Table 2.1: Comparison among different electrochemical storage systems for the key grid, [63].
√: very suitable, ∼: less suitable, •: unsuitable

Application	Pb acid	Li-ion	NiMH	Na/S	NaNiCl_2
Time-shift	√	∼	∼	√	√
Renewable integration	√	√	√	√	
Network investment deferral	∼	√	∼	√	√
Primary Regulation	√	√	√	√	√
Secondary Regulation	√	√	√	√	√
Tertiary Regulation	√	√	∼	√	√
Power System start-up	√	√	√	√	√
Voltage support	√	√	√	√	√
Power quality	∼	∼	•	∼	•

chemical reactions to create a flow of electrons. Primary elements of a cell include the container, two electrodes (anode and cathode), and electrolyte material that is in contact with the electrodes. Current is given by the oxidation-reduction process involving chemical reactions between the cell electrolyte and electrodes. When a battery discharges through a connected load, electrically charged ions in the electrolyte that are near one of the cell electrodes supply electrons (oxidation), while ions near the cell other electrode accept electrons (reduction) to complete the process. The process is reversed to charge the battery.

Electrochemical energy storage in batteries is basically a mature technology, since it has been utilised for more than a century based on industrial products. However batteries have many shortcomings in a variety of use cases. As an example, Li ion battery technology can be called mature in the sense that it is already used widely in a spectrum of applications and yet it is immature in the sense that improved performance is demanded for other new applications, such as those in electricity grids challenge. For this reason, in order to increase the battery penetration within the electric market, significant technology and scientific breakthroughs are still needed.

Batteries are estimated to be one of the key storage technological enablers of the transition from the current mostly centralised electricity generation networks to distributed ones with increasing penetration of variable and not programmable renewable energy sources (e.g., wind and photovoltaic) and more “intelligent” management of the energy flows (with Smart Grids and “pro-users”, who are end-users with more active role in the electricity market). Different battery technologies are currently available on the market for smart grid and energy system applications, each one presenting a different effective suitability concerning the required key applications. Table 2.1 shows a schematic comparison of the effective suitability of the various battery competing technologies, [63]. The main economic and technical features of the most commercial batteries concerning the electric grid application are illustrated in Table 2.2. Those features refer to the current status and some predicted targets towards 2030, according to [63, 65, 66].

Table 2.2: Current battery features and targets towards 2030

.

Storage System	Current performance	Target 2030
Lead-acid	Life: 2000-4500 cycles Temp:-10 to +45°C Efficiency: 70-90% Self discharge: 0.1-0.3% TCC: 437 €/kWh	Life: 3000-10000 Temp:-30 to +60°C
Li-ion	Life: 1500-4000 cycles Temp: -20, +60°C Efficiency: 85-95% Self discharge: 0.1-0.3% TCC: 546 €/kWh	Life:5000 cycles Temp: -20, +70°C
Ni-Cd	Life: > 2000-2500 cycles Temp: -40 to 50 °C Efficiency: 60-73% Self discharge: 0.2-0.6% TCC: 699 €/kWh	Life: > 6000-8000 cycles Temp:-40 to +70°C
Ni-MH	Life: 500-2000 Temp: 0 to +45°C Efficiency: 70-80% TCC:	
Na-S	Life: 2500-4500 cycles Temp: -20 to +45°C Efficiency: 75-90% Self discharge: 20% TCC: 343 €/kWh	Life: >10000 cycles
NaNiCl_2 (ZEBRA)	Life: 2500-3000 Temp: -20 to +45°C Efficiency: 86-88% Self discharge: 15% TCC: 1095 €/kWh	

2.2.2 Charging and discharging process of batteries

Within the presented study batteries are charged considering their charging efficiency and the process ends when the storage reaches its nominal capacity (fully charged status). The discharging process lasts until the batteries reach the minimum capacity status defined by the depth of discharge value (DOD). Considering an interval time i equal to 15 minutes, the charging and discharging processes can be explained through Equations (2.18) and (2.19). In particular, the battery charging process from PV array begins when the PV production exceeds the electric load demand and the discharging process starts when the PV array production is no longer able to satisfy the load.

$$S_b(i) = \begin{cases} S_b(i-1) + E_{PV}(i)\,\eta_c & \text{if } S_b(i-1) + E_{PV}(i)\,\eta_c < B \\ B & \text{if } S_b(i-1) + E_{PV}(i)\,\eta_c \geq B \end{cases} \tag{2.18}$$

where $S_b(i)$ is the battery capacity at interval time i (kWh), E_{PV} is the exceeded energy form PV array at interval time i (kWh), η_c is the charging efficiency and B is the nominal capacity of the battery (kWh).

$$S_b(i) = \begin{cases} S_b(i-1) - \dfrac{D(i)}{\eta_d} & \text{if } S_b(i-1) - D(i) > B\,(1-DOD) \\ B\,(1-DOD) & \text{if } S_b(i-1) - D(i) \leq B\,(1-DOD) \end{cases} \tag{2.19}$$

where $D(i)$ is the energy requested at time i and η_d is the discharging efficiency.
Systems that consist of PV generators, storage batteries, and loads need controls to protect the battery from overcharge or deep discharge. Overcharge will damage the storage batteries used in these systems, and high-voltage cutoff or power-shunting devices are used to interrupt the current to batteries after full charge has been achieved. The voltage across a battery is a function of the state of charge of the battery. Excessive discharge will also damage the batteries, and low-voltage cutoff devices are used to detect low voltages and disconnect the batteries when the DOD is reached. This results in an interruption of power to the loads and necessitates the use of either very large batteries or an additional source of electric energy if very high degrees of reliability are required. Stand-alone systems require very high degrees of reliability and in order to ensure a continuous electricity supply a backup system is introduced. Furthermore, if AC power is needed, DC/AC inverters will be required. This may be the case if AC machinery is to be operated or if the PV system is to be tied into a utility grid. Inverters are available that will generate frequencies to match utility frequencies. The use of a DC/AC inverters is necessary to maintain the flow energy between the AC electrical load and DC components of the hybrid energy system. According to [45], the total size of the inverters must be sufficiently capable to size the maximum power of AC loads and therefore its size is chosen conservatively equal to 110% of the AC peak load.

2.3 Backup System

Backup power systems allow to continue using certain, or all, appliances when utility provided electricity is not available. Concerning on-gris energy systems, electricity can be lost due to downed lines, malfunctions at a sub-station, rush weather, planned blackouts or in extreme cases a grid-wide failure. While in off-grid energy systems, the backup system is crucial to provide electricity constantly if one, or all, the system components have an operating crash or, mostly common, if solar radiation is not sufficient and PV system, consequently, does not supply enough energy and, at the same time, the storage system is not longer able to satisfy the load because it reached the minimum level of charge. Mostly, the emergency power systems have been and are still based on generators; usually, these generators are diesel engine driven, although some smaller energy systems may use a gasoline engine driven generator and larger ones a gas turbine. However, lately, more use is being made of other technologies such as flywheel energy storage or fuel cells.
With regular generators, an automatic transfer switch is used to connect emergency power. One side is connected to both the normal power feed and the emergency power feed; and the other side is connected to the load designated as emergency. If no electricity comes in on the normal side, the transfer switch uses a solenoid to throw a triple pole, single throw switch. This switches the feed from normal to emergency power. The loss of normal power also triggers a battery operated starter system to start the generator, similar to using a car battery to start an engine. Once the transfer switch is switched and the generator starts, the building's emergency power comes back on.
Within this study, the considered backup system is made of diesel generators and the following section illustrates the equations and the methodology used to evaluate the optimal size of the system.

2.3.1 Diesel Generators

The dimensioning process of diesel generators is based on the values of the maximum and minimum peaks electric load and it consists in combinations of diesel generators. To ensure a continuos electricity supply service and to reduce the extra power produced by the diesel generators and the fuel consumption, each generator can operate at 40 %, 60 %, 75 % or 100 % of its rated power and the combinations are sized according to the following restrictions:

- The sum of the rated powers is equal or grater than the 110 % of the maximum peak electrical load demand, the excess power can be used to cover the spinning and/or reserve power as a result of temporary changes in electrical load:

$$G_1 + G_2 + G_3 + ... + G_n \geq 1.1\, P_{max} \qquad (kW) \tag{2.20}$$

  where P_{max} is the maximum electrical peak load and with
  $G_1 \leq G_2 \leq G_3 ... \leq G_n$.

In order to optimise the consumption of energy supplied by diesel generators and consequently to

reduce the wasted energy, two more conditions are needed in the backup system configuration:

- The 40 % of the rated power of the smallest generator has to be bigger or equal to the minimum electrical peak load:

$$0.4\,G_1 \leq P_{min} \qquad (kW) \tag{2.21}$$

  where P_{min} is the minimum electrical peak load. This restriction ensures that the minimum peak load is fed by the lowest consumption condition corresponding at the smallest amount of wasted energy.

- The rated power of the n^{th} generator has to be bigger or equal to the 40 % of the rated power of the $(n+1)^{th}$ generator:

$$G_1 \geq 40\%\,G_2\,,\, G_2 \geq 40\%\,G_3\,,\, \ldots\,,\, G_{n-1} \geq 40\%\,G_n \qquad (kW) \tag{2.22}$$

  This restriction ensures that there is no energy gap between two consecutive sizes of generators, and the demand is still feb by the lowest energy consumption condition.

The nominal rated powers simulated to obtain the suitable combinations are picked from a database composed of 20 different generators sizes. The simulation tries to reduce the number of diesel generators and it initially evaluates if at least one or more couples of diesel generators are able to satisfy the above restrictions, if not, it calculates combinations with a generator more until the simulation finds out at least one combination that fulfils the imposed limits. This design process does not include a spare generator, used in the case of sudden damage of the current system.

3

EHS Software

EHS (Energy Hybrid System) is a software programmed to evaluate the optimal design for various configuration of energy hybrid systems. The evaluation of the optimal hybrid system configuration is based on the value of the LCC calculated along the potential lifetime of the entire system, considering all the future costs and the interest rate, according to [67].
In order to figure out the hybrid system configuration able to satisfy the required load at the lowest LCC, the present study simulates 25 different photovoltaic array sizes, 25 different capacities of battery storage, an inverter and a backup system consisting in a combination of two or more diesel generators.

The simulated hybrid system works based on a *load-following* strategy described below:

1. If the solar radiation is adequate, PV power is used to supply directly the load and the possible surplus power is used to re-charge the electric storage.

2. When PV production is not sufficient, the load is supplied also by the battery storage.

3. If the PV power production is not sufficient and the electric storage can not longer supply the load, the power is fed by the backup system (diesel generators).

4. The combination of diesel generators is composed by a number of generators which sum of the total rated power is equal or bigger than the 110 % of the maximum electrical load, the 40 % of the rated power of the smallest one is equal or minor than the minimum electrical peak load, and, eventually, the rated power of the smaller generator is equal or larger than the 40 % of the bigger generator. Each generator can work at 40, 60, 75 or 100 % of its rated power depending on the required loads.

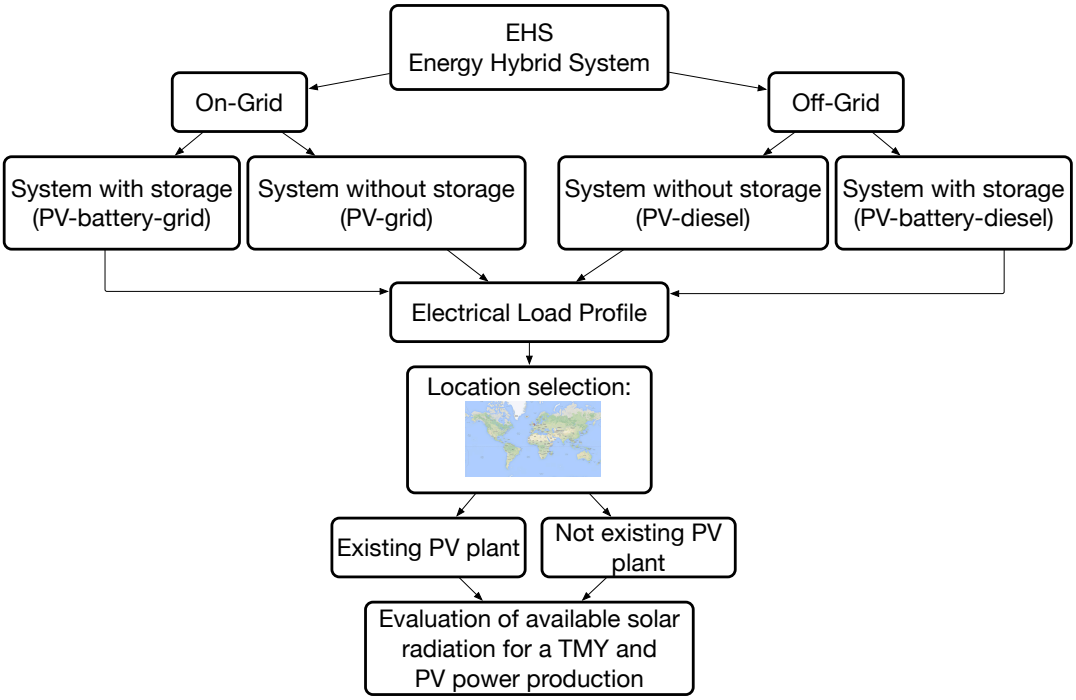

Figure 3.1: EHS model

The main structure of EHS software is illustrated in Figure 3.1 and in Figures 3.2 and 3.3 the structures for the off-grid and on-grid systems are described. As illustrated in Figure 3.1, at the beginning of the software operating system, the user can choose between the two main different systems: on-grid, if the system is connected to the electric grid, and off-grid if the system is stand-alone and not reached by the electric grid. Within this two main systems the user can select if the hybrid system has to be design with or without storage system.
Once the hybrid system is chosen, data concerning electric load profile have to be inserted. The software proposes 13 different load profiles listed below:

- Business
  - Office - option 1 (working time: 9PM-1PM; 3PM-5PM)
  - Office - option 2 (working time: 8PM-1PM;2PM-8PM)
  - Restaurant - option 1 (all day lunch&dinner)
  - Restaurant - option 2 (all days only dinner and lunch in the weekend)
  - Restaurant/Pub (evening hours)
  - Shop (shopping hour)

  - Shop (continuos hour, mall)

- Home
  - Household profile
  - Full time employment profile

- Public service
  - School/University
  - Hospital

- Factory
  - Factory 24h
  - Factory 8h

The mean daily load has to be inserted by the user; preferably al so the peak and base load have to be inserted but if those data are not available the software calculate them depending on the chosen load profile. If none of the set profiles fits with the requested load, the user can insert manually a specific load profile and therefore add the mean daily, peak and base load. The load profile can be added by season, week and day in a way that, for more detailed data, every information can be inserted in the simulation (i.e. a load that does not work in summer or during some specific months of the year, or it works only few days per week).
As a further step, the user has to chose the location where the hybrid system has supposed to be built. This step can be done in three ways: (i) inserting the city or region name, (ii) selecting a point on the map, and (iii) inserting the latitude and longitude coordinates. The user can chose the most suitable option to identify the desired location.
The selection of the location is a crucial step to obtain the most correct solar radiation data. The EHS software has a database of solar radiation for 614 locations in the world of which 316 cities in Italy, 165 cities in the rest of Europe and 133 cities in the rest of the world. The database is progressively increasing: more and more cities can be added and existing data can be updated. The current data are taken considering the Typical Metereological Year (TMY) of each of the city/area considered. Data are of global solar radiation are taken every 15 minutes for the entire year. If the simulating system has already an existing PV plant, in case the dimensioning process is run to know the optimal size of the storage, the user has to insert the data concerning that plant and specify some parameters as size, cost of investment, cost of maintenance, age, efficiency, lifetime, PV productivity, tilt and azimuth. If the PV plant does not exist and EHS has to provide the optimal size of the plant, 25 different PV array sizes, ranging between the 10% and the 400% of the maximum electrical peak load, are simulated. The user can chose the type of plant (ground-base, roof-based) and insert all the available data he has

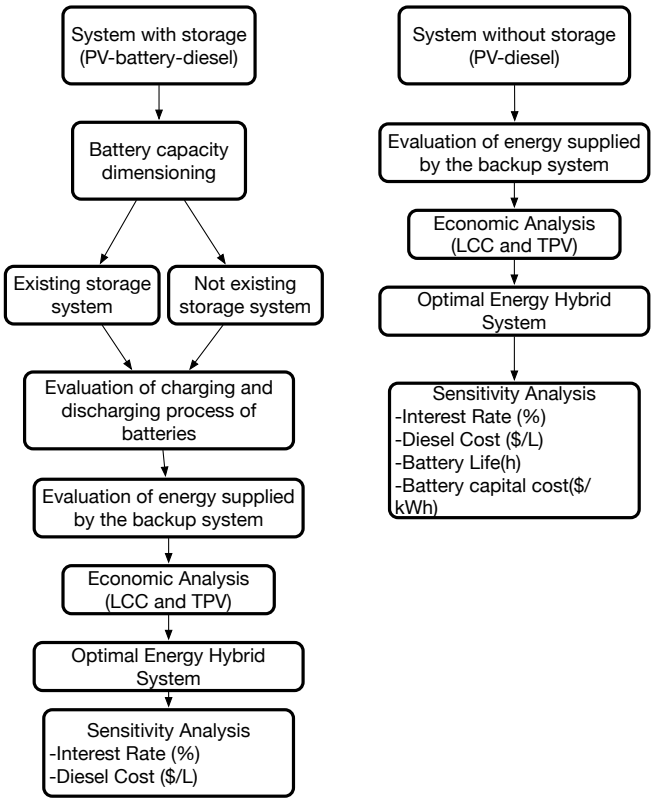

Figure 3.2: EHS model_offgrid details

concerning the plant or, in case of missing technical and economic data, he can use the default values given by the software. Once the existing PV size or the 25 sizes are set,

The simulation is carried out every 15 minutes for 366 days in order to observe in detail how a sudden variation of solar radiation affects the system reliability and, therefore, the potential system configuration. The economic evaluation considers the simulated year projected along the entire lifetime of the system, taking into account the interest rate to estimate future expenses.
Given the electric demand profile, the configuration of the hybrid system is build up through five main steps:

1. Selection of backup system combinations that satisfy the imposed restrictions
2. Evaluation of the available global solar radiation for an entire year
3. Dimensioning of the PV array
4. Dimensioning of electric storage considering the PV array energy surplus

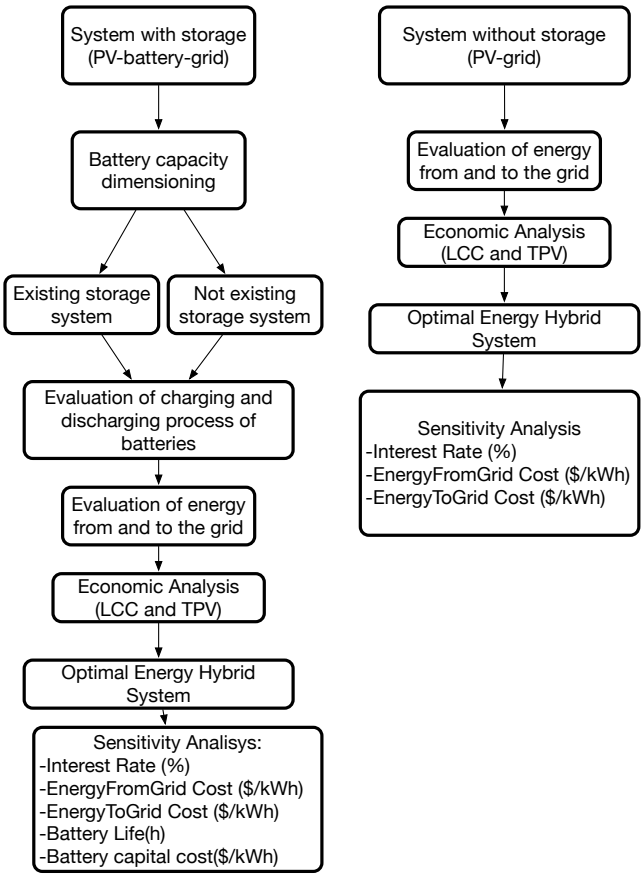

Figure 3.3: EHS model_ongrid details

5. Implementation of LCCA on each hybrid system configuration and identification of the one with the lowest TLCC as the optimal solution.

3.1 Life Cycle Cost Analysis (LCCA)

According to [67], Life Cycle Cost Analysis (LCCA) is "the total discounted cost of owning, operating, maintaining, and disposing of a facility over a period of time". LCCA is basically implemented through three variables: the *costs* of the facility, the period of *time* over which these costs are incurred, and the *discount rate*. The costs included in the LCCA evaluation are divided into two major categories: initial and future expenses. The first ones are all the expenses incurred before the facility activities start and they are considered at the beginning of the study period at "year 0". The future costs are all the expenses incurred after the activity of the facility has begun and they can be considered anytime between the "year 1" and the "year n", considering the facility lifetime equal to n years. Future expenses are by definition divided into four different type of costs: (i) the operation and maintenance

costs, involved in the yearly operation of the facility, (ii) the repair yearly costs, required to prolong the life of a system without replacing it, (iii) the replacement costs, that are typically generated by replacement of a system or one of its component that has reached the end of its useful life, and, eventually, (iv) the residual cost, that is the net value of a facility at the end of the analysis period, a negative residual cost means that there is a value associated with the system at the end of the study period while a positive residual cost indicates that there are disposal costs associated with the facility at the end of the survey period. The discount rate is defined, according to [15], as "the rate of interest reflecting the investors time value of money" and it is therefore applied to future expenses to equate them with present day costs.
The fundamental purpose of LCCA is than to estimate the total life time cost for a system through the sum of all costs associated with it. The LCC equation can be expressed as following:

$$LCC = C_{Inv} + C_{O\&M} + C_R + C_{Rep} + C_{Res} \qquad (\$) \tag{3.1}$$

Where C_{Inv} is the cost of investment of the entire system (initial expenses), $C_{O\&M}$ is the operational and maintenance costs, C_R corresponds to the repair cost, C_{Rep} the replacement cost of the components of system depending on their lifetime, and C_{Res} is the residual cost of each component at the end of the lifetime of the system. The present study allocates the investment cost at the year 0 and all the future expenses as a yearly cost depending on the single component from year 1 until the end of the system lifetime.
To accurately combine initial expenses with future expenses, the present value (PVL) of all expenses must first be determined. The PVL is defined by [67] as "the time-equivalent value of past, present or future cash flows as of the beginning of the base year". Therefore, the evaluation of thePVL of an outlay is used to compare future payments over a certain time to one point in the present time. The concept of this method is that anticipated future costs are brought back to present cost (discounted) by calculating how much would have to be invested at a market discount rate to have funds available when they will be needed. The PVL of a LCC for a single year j is calculated as follows: [67]

$$PVL_j = LCC_j \cdot \frac{1}{(1+d)^{-j}} \qquad (\$) \tag{3.2}$$

where, LCC is in \$, j is the year, and d is the discount rate. Once all pertinent costs have been established and discounted to their present value, they can be summed to generate the total life cycle cost (TLCC) of the system through Equation (3.3).

$$TLCC = \sum_{j=0}^{n} LCC_j \cdot \frac{1}{(1+d)^{-j}} = \sum_{j=0}^{n} PVL_j \qquad (\$) \tag{3.3}$$

3.2 The web-base platform

In this section some images of the web-base platform are illustrated to clarify the software operating system and how the users can manage it. The main interface of EHS is shown in Figure 3.4, the user can create a new project choosing between the four options or open an already existing project previously initialised. In Figure 3.4 four already set projects are illustrated, one for each options and for different location.

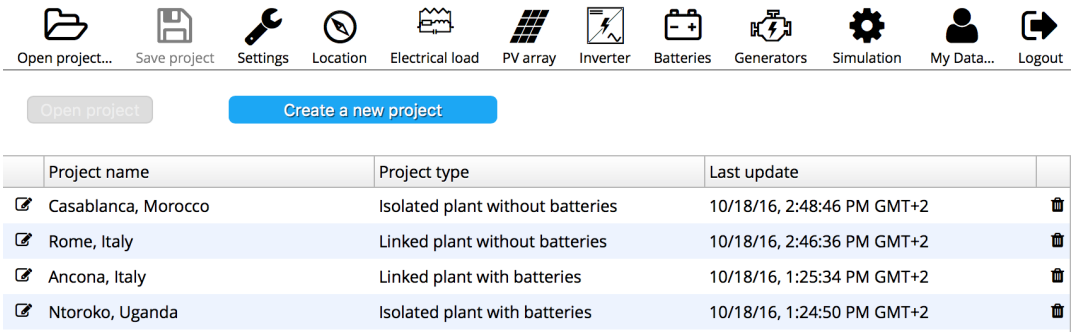

Figure 3.4: Software Main interface

Figure 3.5 shows the setting interface, where it is possibile to insert the main data concerning estimated lifetime of the entire system, the money unit that will be use to insert data of costs and carry out the economic analysis, the fuel cost related to the chosen location, the energy price to and from the grid, the interest rate related to the country where the entire system will be installed and some parameters that will be analysed at the end of the design process to carry out the sensitivity analysis.

The selection of the location where the plant has to be installed can be done in different ways as illustrated in Figure 3.6. The user has three options: (i) inserting the latitude and longitude coordinates, (ii) inserting the name of the location, and (iii) choosing a point on the map. The software will chose the closest location where solar data are available within the inner database and it will show the location where solar data belong to. For instance, in Figure 3.6, after choosing the location "Ancona, Italy", the closest data available refer to "Senigallia".

The electrical load profile is a pivotal information for the software simulation: the more detailed profiles, the more accurate results. As explained in the previous section, the user can chose 13 different load profiles or insert manually its own profiles. In Figure 3.7a the "business profile- Office 2" has been chosen between the proposed ones and data concerning the mean daily load, load-base and maximum peak have been inserted, Figure 3.7b. The software draws an estimated trend of the load during a week abide by the user data in order to give a visual and clear representation of the data that will be use within the simulation. Data concerning the mean daily load will be used to evaluate the range of storage system, while the base-load and the maximum peak load will be taken into account to

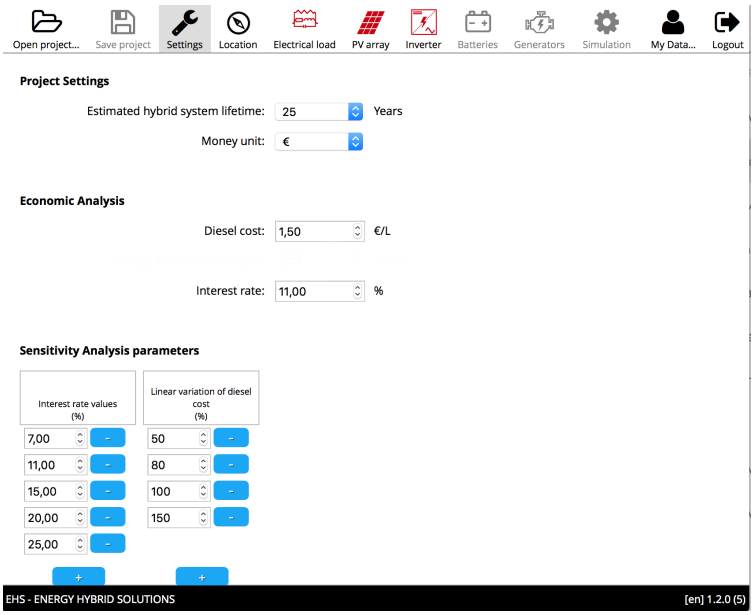

Figure 3.5: Settings interface

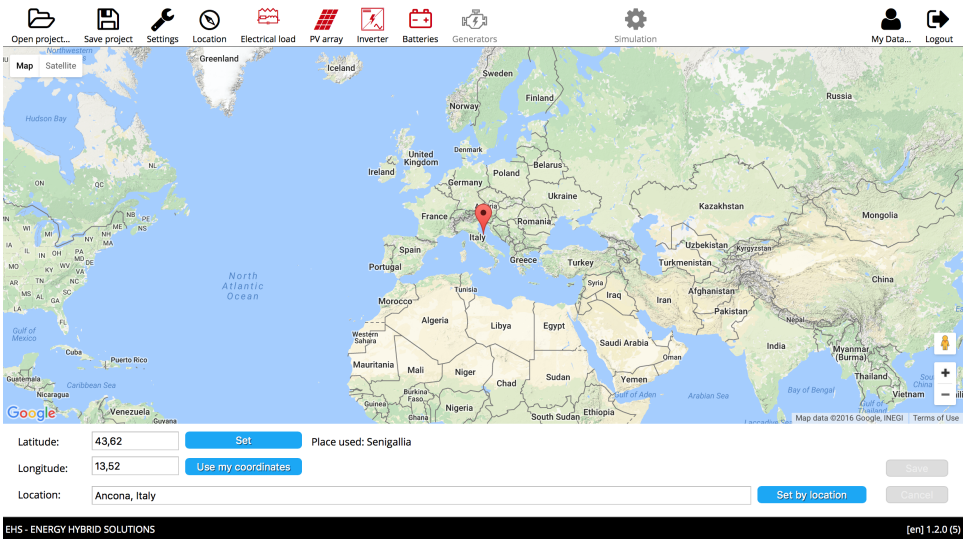

Figure 3.6: Location interface

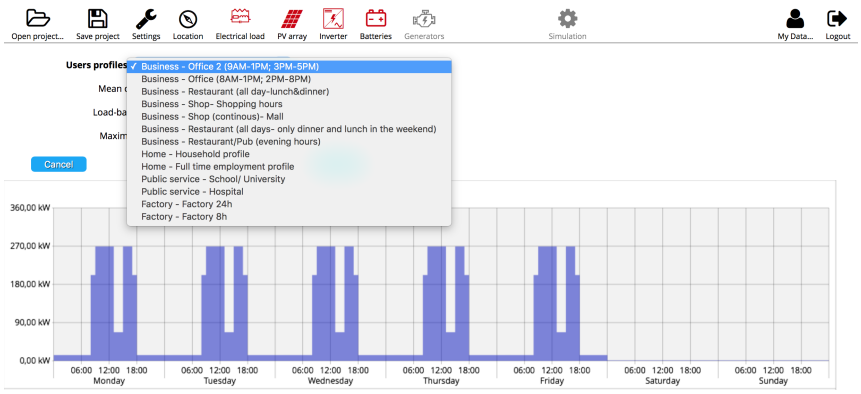

(a) Profile Interface, selection of the load profile

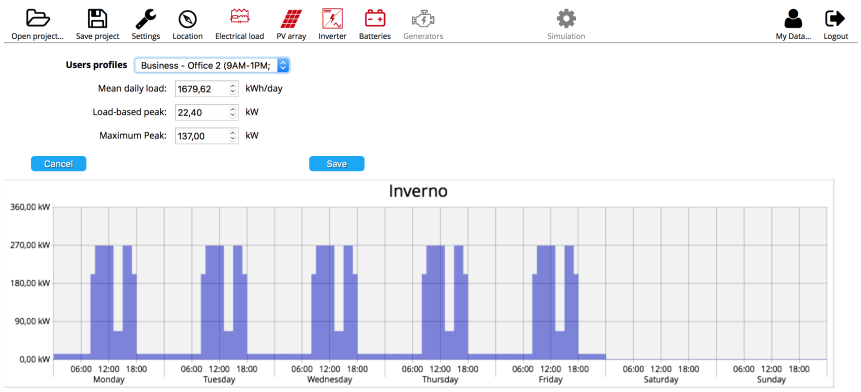

(b) Profile Interface, trend of the profile

Figure 3.7: Profile interface.

estimate the most suitable combination of backup generators in the systems isolated by the electric grid.

Successively at the main data input, the user can chose the parameters concerning the energy system components. In Figure 3.8 is illustrated the photovoltaic section where two options are proposed: (i) not existing PV plant (Figure 3.8a) and (ii) existing plant (Figure 3.8b). In the first case, the simulation will use a range of PV plant sizes as explained in the previous section and, if the model of the plant is already known, the user has the chance of choosing the installation type and insert some technical and economic parameters. If the user does not have these information the software will use the default ones. If a PV plant already exists and the simulation is mainly used to size the storage system, the user will insert the correct size of the plant in kWp and all the data related to it.

In Figure 3.9 is presented the storage system interface, where, similarly to the photovoltaic interface, the users can chose if to simulate the capacity if the system or to insert an already existing storage system. In the first case, Figure 3.9a, the battery type can be chosen between a list of different

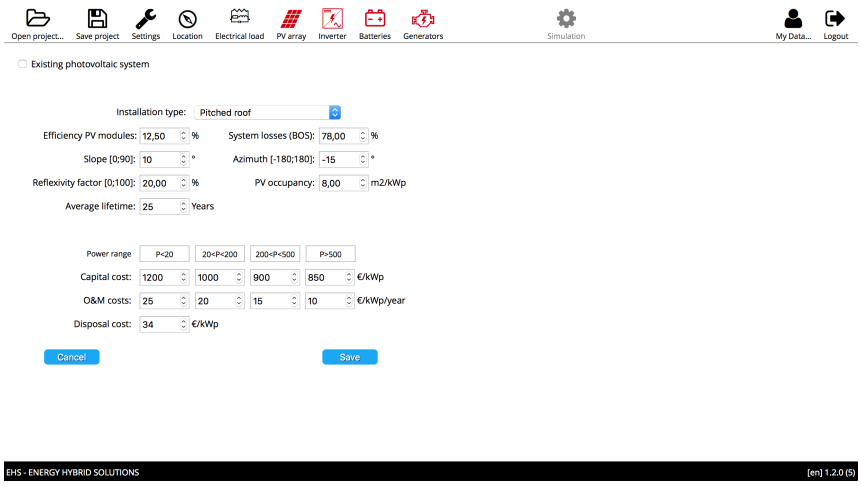

(a) Photovoltaic interface with no existing plant

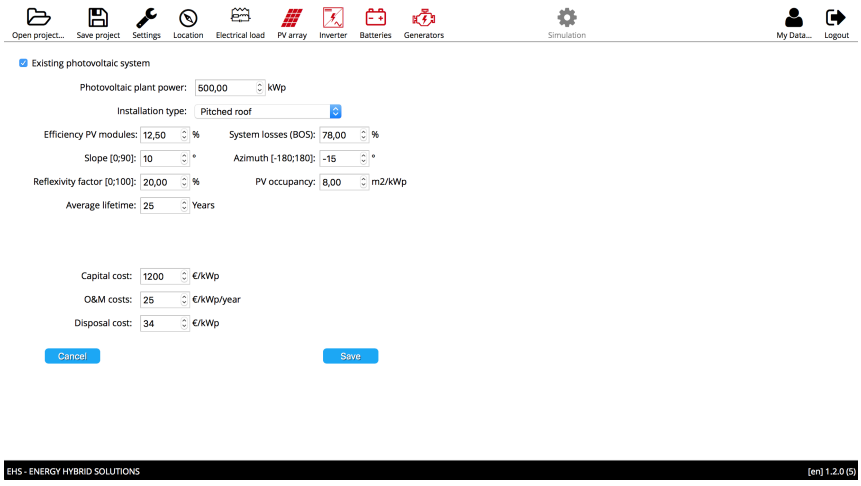

(b) Photovoltaic interface with existing plant

Figure 3.8: Photovoltaic interface

technologies explained in Section 2.2.1 and technological and economical parameters can be added or left as the default ones. In Figure 3.9b the user has to insert the data concerning the existing storage system and specify its capacity.

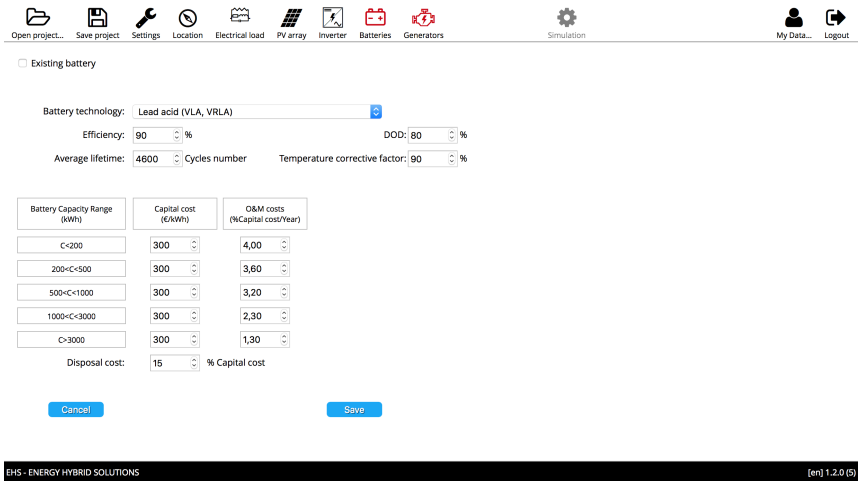

(a) Storage System interface with no existing plant

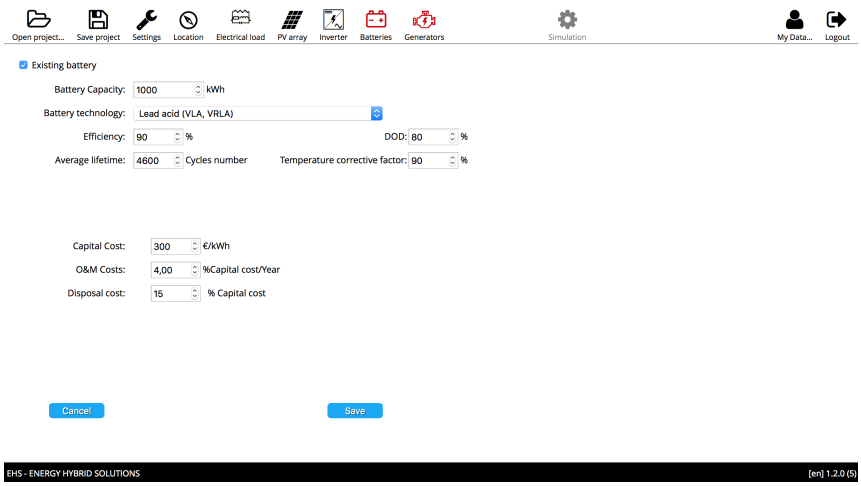

(b) Storage System interface with existing plant

Figure 3.9: Storage System interface

Concerning the hybrid systems connected to the electric grid, there is no need to design the backup system: the load that is not satisfy by the PV plant and storage system is supply by grid and, when the storage is full and the PV production exceeds the electric request, the extra power is sent to the grid. Therefore the simulation is evaluated considering the costs and the prices of electricity from and to grid initially inserted by the user.

The hybrid systems not connected to the electric grid have a further step in the design process that

regards the backup system. The backup system supplies the load when PV and storage are not longer able to satisfy it and it has to be design to supply the load in any case in order to ensure a good reliability of the system. The generators sizes are evaluated as explained in Section 2.3 and, as illustrated in Figure 3.10, a couple of generators is proposed as the optimal combination. Nevertheless, the user can modify the size of one or both generators and their data concerning fuel consumption and costs. The limit imposed by the software is that the user can vary the size of the generators as long Equation (2.20) is respected, since the sum of the rated powers has to be equal or grater than the 110 % of the maximum peak electrical load demand.

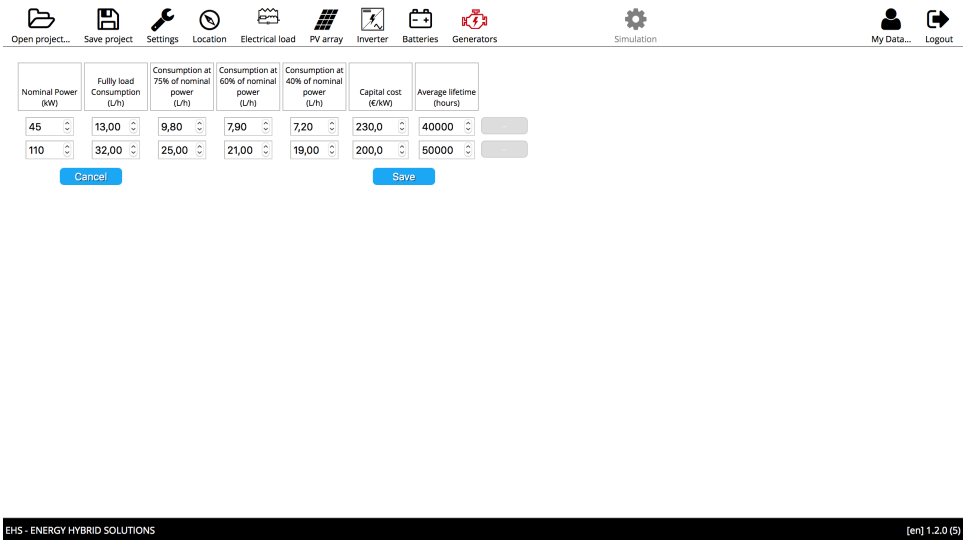

Figure 3.10: Backup System interface

4

Results

In this section an interesting case study is presented: the design processes through the EHS software of an off-grid hybrid system located in an isolated village in Uganda. The first part of the section presents the case study: the electrical load and the potential PV production related to the location. The second section illustrates the results of the design process obtained through EHS for three different situations: (i) with storage system, (ii) without storage system and (iii) the current system with only diesel generators in order to carry out a comparison with the current situation. Eventually, in the last section, the sensitivity analysis on the presented case study is shown.

4.1 Case study

The design presented in this case study aims at figuring the optimal stand-alone hybrid power system configuration for a village in Uganda named Ntoroko (Latitude 1.05, Longitude 30.53). The village counts about 2'000 habitants and currently is not reached by the national electric grid, therefore the electricity is totally supplied by diesel generators. The proposed configuration of the system is composed of a PV array, an electric storage, an inverter and a back-up system of diesel generators. The supposed lifetime of the entire system equals to 25 years. Figure 5.6 shows a schematic diagram of the stand-alone diesel generators system currently used to supply the electrical load (a) and the hybrid PV-battery-diesel energy system that the present study aims to implement (b).

4.1.1 Electrical Load Data

In order to design the hybrid system according to the village electrical demand, three main data are registered:

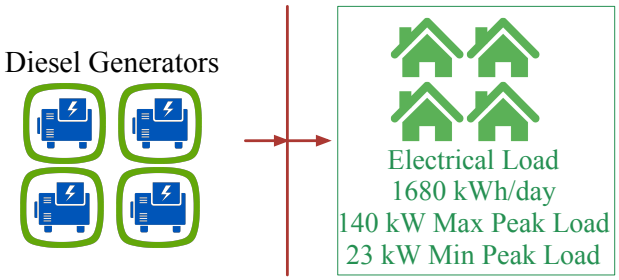

(a) Currently existing diesel generator energy system

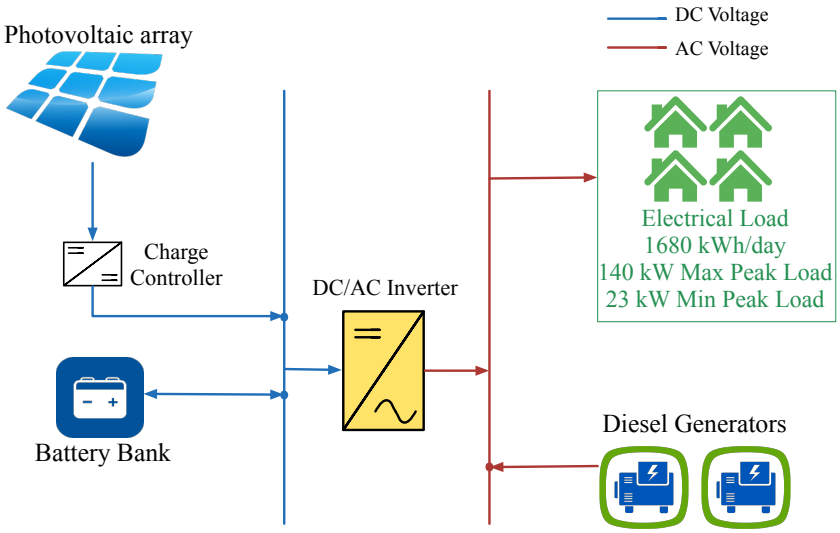

(b) Proposed hybrid PV-battery-diesel energy system

Figure 4.1: Schematic diagrams of the current (a) and the proposed (b) energy system.

- The daily electrical load profile (kWh)
- The maximum electrical peak load (kW)
- The minimum electrical peak load (kW)

Load profile data of the considered village are important to evaluate the optimal system configuration. Because of the absence of electric load monitoring systems and of the low level of electricity consumption information, the daily load profile of the village is defined considering the number of electric devices currently used and the living and working activities of the inhabitants.
Due to the extremely low information level concerning electricity consumption, two load profile trends are considered: the weekday and the weekend load profile, the last one presents a lower electricity consumption due to the factories and shops closures during the weekends. The village is located within the equatorial zone where there is little distinction between seasons and solar daily hours are constant during the entire year. This geographic peculiarity leads to assume that the two load profiles are the same for every working day and weekend of the year, because the working hours, electricity consumption and habitants activities took place almost at the same daytime during the year.
The electric load is classified in three different categories which affect the load profile at different times of the day: fridges, lights, and others (TVs, computers, and factories). The mean electrical daily consumption equals to 1680 kWh, the maximum electrical peak load corresponds to 140 kW while the base load is 20 kW. The load profile trend of weekdays, illustrated in Figure 4.2, shows two main peak demand periods occurring in the early morning around 6 AM and in the evening (7-22 PM) mainly due to the increase in usage of lights.

4.1.2 PV power production

The potential configurations of the hybrid power system are carried out with the backup system of diesel generators selected according to Section 2.3, 25 different photovoltaic array sizes, 25 different capacities of battery storage, and an inverter.

The diesel generators combinations are chosen within a database of 19 generators from 10 to 180 kW (with a 10 kW size step) and they are carried out from the model exposed in Section 2.3; the results of this simulation applied to the study case shows that two couples of generators are able to satisfy the fixed restrictions. The nominal power of the two combinations are exposed in Table 4.8. These combinations closely hinge on the maximum and minimum electric peak load and they are chosen independently from the PV array size and the storage capacity.

The generator G_s is the smallest one and it works when the requested electrical load is not met by either the PV system or the battery storage but is minor or equal to the nominal power of G_s; when this generator is not longer able to satisfy the load it stops and G_b ,the biggest generator, starts to work. When the required electrical load is bigger than the nominal power of G_b, G_s starts to

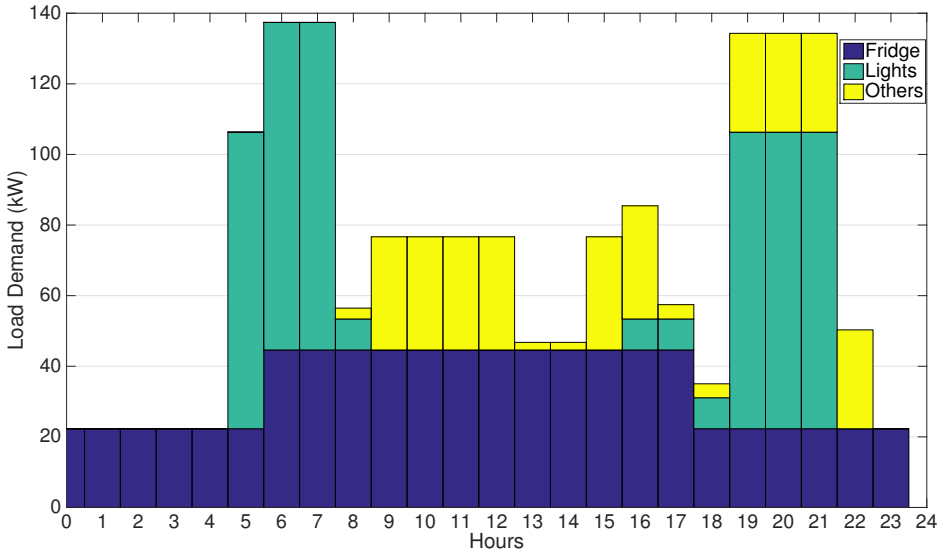

Figure 4.2: Typical electrical daily load profile during weekday at Ntoroko, Uganda.

Table 4.1: Combinations of diesel generators selected for the study

Combination	$G_b(kW)$	$G_s(kW)$
1	110	50
2	120	50

Table 4.2: Diesel generators data

Ra (kW)	Fuel consumption 40 - 60 - 75 - 100% (l/h)	Lifetime (hours)	Capital Cost ($/kW)
50	8 - 8.5 - 10.42 - 13.9	40000	230
110	19 - 21 - 25 - 32	50000	200
120	20 - 22 - 36 - 33.1	50000	200

work in parallel in order to successfully satisfy any requested electrical load. Table 4.2 shows the data, taken from [68], used to evaluate the performance and costs of the two combinations of generators.

The simulation runs with radiation solar data registered every 15 minutes for 365 consecutive days of an entire year. The global solar radiation data $G\ (W/m^2)$ registered at Ntoroko every 15 minutes from the 1st of January 2004 to the 31st of December 2004 are carry out form the SoDa-solar radiation data service [69]. The PV panels are tilted at an angle β equal to 10° and orientated at a surface azimuth angle γ equal to $-15°$ to optimise the captured solar radiation.

The 25 simulated PV array sizes range between 30 kWp and 550 kWp, corresponding to the 10 % and the 400 % of the maximum electrical peak load, respectively, and the step between consecutive sizes is equal to 20 kWp. Table 4.3 summarises all the technical data used within this study concerning the different sizes. PV production is based on the solar radiation data obtained in Section 2.1 and on the data shown in Table 4.3. Figure 4.3 illustrates the power production of four different PV array sizes during the 17th of August (blue curve) compared with the load demand profile of a weekday (green curve) and the power not satisfied (red curve). The 17th of August has been chosen as a sample day of good weather to observe how the power system works under the best conditions. Figure 4.3 shows that the PV production does not match the electrical load profile,

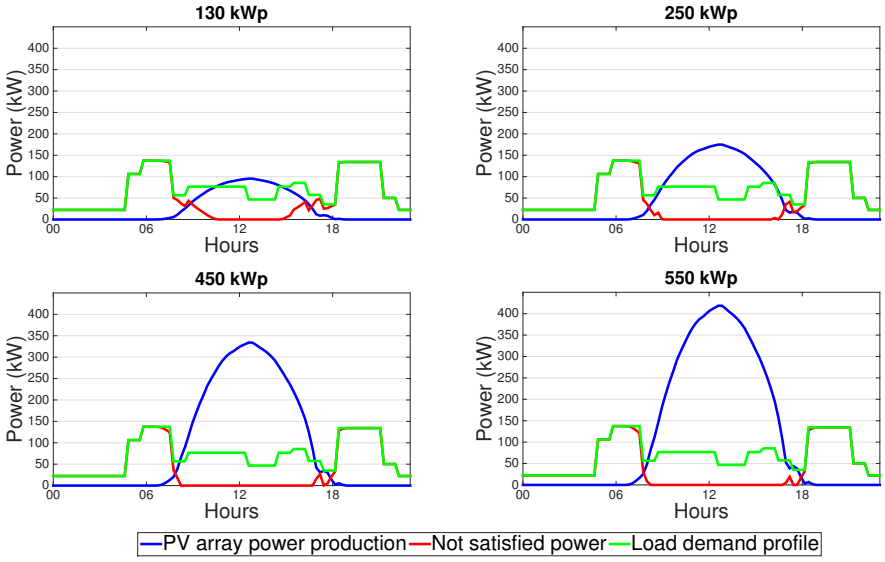

Figure 4.3: PV production at the 17th of August 2004 (blue line), daily load profile in the village of Ntoroko (green line), unsatisfied power (red line).

the load peaks are mainly in the early morning and late afternoon when the PV production is low, the excess PV energy will be wasted or stored in the electrical storage. Data concerning the costs

Table 4.3: PV array technical data used in the simulation

PV array technical data	
Efficiency (%)	12.5
Losses of BOS (%)	78
PV productivity (m^2/kWp)	8
Tilt ($0° \leq \beta \leq 90°$)	10°
Azimuth ($-180° \leq \gamma \leq 180°$)	$-15°$

of the different sizes of PV array, used to implement the economic evaluation, are exposed in Table 4.4.

Table 4.4: PV array costs

Range of PV size (kWp)	Capital costs ($/kWp)	O&M costs ($/kWp-year)	Disposal costs ($/kWp)	Lifetime (years)
$Size < 20kWp$	1200	25	34	25
$20 \leq Size < 200kWp$	1000	20	34	25
$200 \leq Size < 500kWp$	900	15	34	25
$Size \geq 500kWp$	850	10	34	25

4.2 Results

The study considers the sodium sulphur (NaS) battery storage technology. According to [70], the highly corrosive nature of sodium make this type of batteries suitable only for large-scale stationary applications and they are currently used in electricity grid related applications such as peak shaving and improving power quality. Compared to other commercial battery technologies, such as lead acid, nickel cadmium (Ni-Cd), sodium nickel chloride, and litium ion batteries, the NaS batteries present a very high number of typical cycle life that varies between 2000 and 3000 cycles at 100 % of DOD and between 4000 and 5000 cycles at 80 % of DOD, which fits appropriately with the daily battery usage and the proposed lifetime of entire hybrid energy system. The technical and economic data of NaS batteries used for the simulation are taken from [71] and exposed in Table 4.5.

Table 4.5: Battery storage technical data used in the study

Battery technical data	
η_c (Charging Efficiency)(%)	90
η_d (Discharging Efficiency) (%)	90
DOD (depth of discharge) (%)	80
Corrective temperature factor	0.9
Lifetime (charge/discharge cycles)	4500

The 25 simulated battery capacities vary between 160 kWh and 2500 kWh, that correspond to the 10 % and 150 % of the mean daily electrical consumption, respectively, and the step between two consecutive capacities is about 95 kWh. This range, as the PV array size one, is selected following preliminary tests that have been performed in order to find out the more acceptable and reasonable values to simulate the optimal electric storage design. Figure 4.4 shows the charging and discharging process of six storage capacities for four different simulated PV arrays during an entire day (0-24 hours) corresponding to the 17th of August 2004. The “left y-axis” of each sub graph refers to the batteries capacity (kWh), while the “right y-axis” is expressed in kW and refers to the PV array power and the electrical load profile. The charging and discharging process varies significantly with the PV

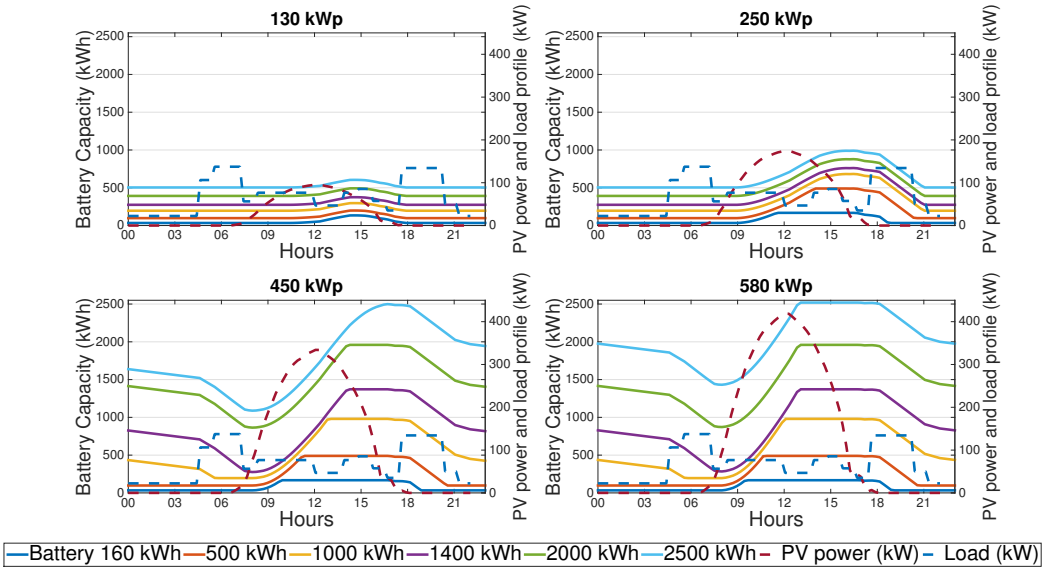

Figure 4.4: Battery charging and discharging process with different PV array the 17th of August 2004

size: when PV size is less than 250 kWp the battery does never reach its nominal capacity (except batteries with capacity equal or smaller than 500 kWh), while, when PV is equal or larger than 400 kWp (bottom figures), the battery storage is fully charged for at least three hours per day.
Data concerning the costs of the different sizes of battery storage, used to implement the economic evaluation, are exposed in Table 4.6.

Table 4.6: Battery storage costs

Range of battery capacity (kWh)	Capital cost ($/kWh)	Annual Maintenance cost (% of the capital cost)	Annual Operation cost (% of the capital cost)
$capacity < 200kWh$	350	0.7	1.3
$200 \leq capacity < 500kWh$	350	0.6	1.3
$500 \leq capacity < 1000kWh$	300	0. 4	1.2
$1000 \leq capacity < 2000kWh$	250	0.3	1.1
$capacity \geq 2000kWh$	250	0.2	1.1

The total size of the inverters must be larger or equal to 110 % of the maximum AC peak load. The case study presents a maximum electrical peak load of 140 kW and accordingly the simulation runs with a total inverters size equal to 150 kW. Specifications of the used inverters are exposed in Table 4.7.

Table 4.7: Specifications of the inverter used within the simulation

DC/AC Inverter technical data	
Efficiency (%)	90
Lifetime (years)	15
Capital Cost ($/kW)	200
Replacement Cost ($/kW)	200

4.2.1 Economic evaluation of the hybrid system through TLCC

The initial expenses considered within this equation are the cost of investment C_{Inv} of the entire system. The future expenses are: (i) the operational cost consisting of the expense of fuel used for the diesel generators, operation activities of workers and maintenance yearly costs $C_{O\&M}$, (ii) the yearly repair costs of PV array and electric storage C_R, (iii) the replacement cost of the components of system depending on their lifetime C_{Rep} and (iv) the residual cost of each component at the end of the lifetime of the system C_{Res}. The present study allocates the investment cost at the year 0 and all the future expenses as a yearly cost depending on the single component from year 1 until the end of the system lifetime. The TLCC of the hybrid system for its entire lifetime of 25 years is calculated for each possible combination of its components: 25 PV arrays, 25 electric storage capacities and 2 backup systems through Equations (3.1) to (3.3). Within the resulting matrix of 1250 values, corresponding at the TLCC of each possible hybrid system configuration over 25 years, the lowest value is picked and the corresponding combination is identified as the optimal solution to dimension the hybrid power system. The simulation refers to the costs data of diesel generators, PV array, battery storage and inverter are exposed in Tables 4.2, 4.4, 4.6 and 4.7, respectively. The value of the interest rate included within the TLCC evaluation equals to 11 %, which corresponds to the current interest rate in Uganda. Once that the TLCC of each possible hybrid system configuration over its lifetime is calculated, the lowest value is picked and the corresponding combination is identified as the optimal solution to dimension the hybrid power system.

4.2.2 Optimal design of the hybrid system

The design process ends with choosing the system configuration that corresponds at the lowest value of TLCC and with a percentage of wasted PV energy lower than 30% for both the systems with storage and without storage. Figure 4.5 illustrates the trend of the TLCC for all the simulated hybrid systems with storage at Ntoroko village and the best configuration is located at the lowest value of TLCC (green spot). It can be observed that the larger PV array size, the less economic impact of the increasing battery capacity. Until capacity is minor than 1400 kWh, the increase in battery size leads to a minor total cost for large PV array sizes; if battery capacity is larger than 1400 kWh the increase in battery capacity leads to a larger and larger total cost even for the maximum simulated PV array

size. The simulation finds out also the total cost and diesel consumption in case the system works only with diesel generators, which corresponds to the corner with PV array equal to 0 kWp and battery capacity equal to 0 kWh (yellow spot). The TLCC of the configuration with only diesel generators is very high but still lower than the option with PV array equal to 0 kWp and maximum battery capacity (red spot). Table 4.8, shows the optimal component sizes, TLCC, litres of fuel per year and the energy

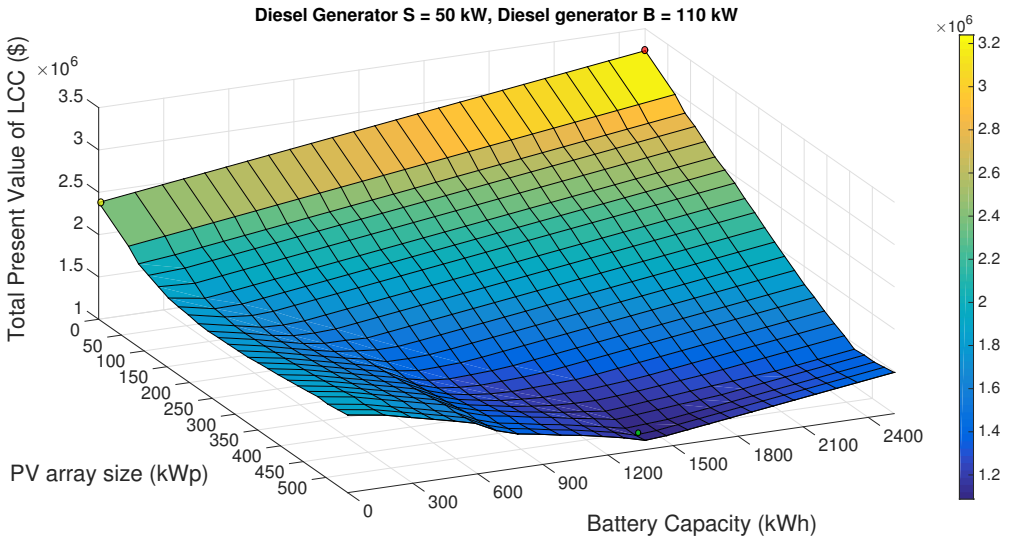

Figure 4.5: Total Present Value of Life Cycle Cost for different PV array sizes and battery capacities with diesel generators combination of 150 and 15 kW

consumption of the hybrid system with a without electric storage and also in case of a system with only diesel generators.
Unfortunately, the solution with the lowest value of TLCC presents a percentage of PV wasted energy grater than 30%. EHS considers only those solutions within this limit and, between them, chooses the one with lower TLCC. The optimal solution for both systems with and without storage are illustrated in Table 4.8.

These results are carried out considering the diesel cost in Uganda equals to 1 $/L (including cost of transport and any other extra costs) and a fixed value of interest rate over the years equal to 11% (current value). Table 4.8 shows that, compared to the current power system S3, the usage of S1 reduces the TLCC over the entire system lifetime of 22.2% and fuel consumption has a reduction of about 77%. On the other hand, the configuration S2, compared to S3, presents a small reduction of fuel consumption (about 8%) and, due to the high investment cost of the PV plant, it does not bring about an economic improvement and the TLCC is 4.4% larger than the one of the S3. In S1 the electric storage has a crucial role for energy saving and cost reduction especially in the presented case study where the peak loads arise in the early morning and late evening when the solar radiation is low and

Table 4.8: Design of the optimal combinations

	With storage (S1)	Without Storage (S2)	Only Backup system (S3)
Diesel Gen. (kW)	110 - 50	110 - 50	110 - 50
PV size (kWp)	340	160	-
Bat. size (kWh)	880	-	-
TLCC (25 yrs) ($)	1'228'800	1'649'600	1'580'100
Diesel Consumption (L/y)	41'026	162'070	176'510
Tot PV energy (kWh/y)	808'420	391'400	-
PV wasted energy (kWh/y) (%)	166'210 - 21 %	172'220 - 44 %	-
Yearly PV productivity (kWh/kWp)	1'600	1'600	-
In&out yearly battery energy (kWh/y)	751'480	-	-
Yearly energy from Diesel Gen. (kWh/y)	35'099	434'455	672'672

PV array has a reduced power production. In S1 the storage spreads the PV energy in the evening and, for larger capacities, also in the early morning reducing drastically the fuel consumption with a reduction 74.7% of compared to S2 and a resulting reduction of TLCC equal to 25.5%.

In order to observe how the operation of the optimal configurations works, the systems, with and without electric storage, are simulated during five days of September (20th-24th September 2004) and illustrated in Figure 4.6. The simulated period has been chosen specifically to observe how the two systems work in case of some consecutive bad weather days, when PV production suddenly decreases and the electric storage is not properly charged during the day. The Figure 4.6a indeed shows on the 21st a large decrease in PV production due to a wide shade of clouds. During the shade the battery charging process stops earlier than the previous day and the resulting storage state of charge implies an increase in energy supplied by the diesel generators during the following day. In this case, the 22nd of September the backup system supplies 300 kWh/day, which is significantly high compare to the 20th of September when energy is not supplied by the diesel generators at all. The energy wasted during the 20th of September equals to 1'067 kWh/day over the supplied 2360 kWh/day and this result points out that during a sunny day about the 37 % of PV energy is wasted and not storage in the battery bank. Figure 4.6b shows that, without an electric storage, an over-size PV array is not longer needed and the optimal PV array size is much smaller. The backup system works every day in the early morning and late evening independently from the weather conditions and a consistent percentage of PV power is wasted during sunny days. In particular, the 20th and the 22nd of September the energy supplied by the backup system is equal to 971 and 1'050 kWh/day, respectively even if there is a large meteorological difference between the two days. The wasted energy from PV on a sunny day (20th of September) is 707 kWh/day over the supplied 1'365 kWh/day and this result points out that during a sunny day the 52 % of PV energy is wasted without the usage of electrical storage. In any case, the backup system is always able to guarantee power production to the final electricity users.

In order to illustrate the mean monthly energy supplied by PV array and diesel generators in the configuration S1, S2 and S3 during a year, Figure 4.7 is presented.

The percentage of wasted energy (light blue bars) is always below 30% of the energy supplied by the PV plant and the mean monthly value of wasted energy corresponds to 27.36% and 29.3% for S1 and S2 respectively. It can be observed that the system S1, besides the low percentage of wasted energy, presents a significant lower values of energy supplied by the diesel generators (red bars) compared to the S2 and S3. Concerning the configuration S2, it can be observed that each month the energy supplied by diesel generators exceeds the energy supplied by PV, during a year the 67% of energy is supplied by generators and 33% by PV array. Figure 4.7c shows the monthly energy supplied by S3, where diesel generators are the only power source. The presented results have been evaluated through constant values of parameters that might change during the lifetime of the system, as the fuel cost and the interest rate.

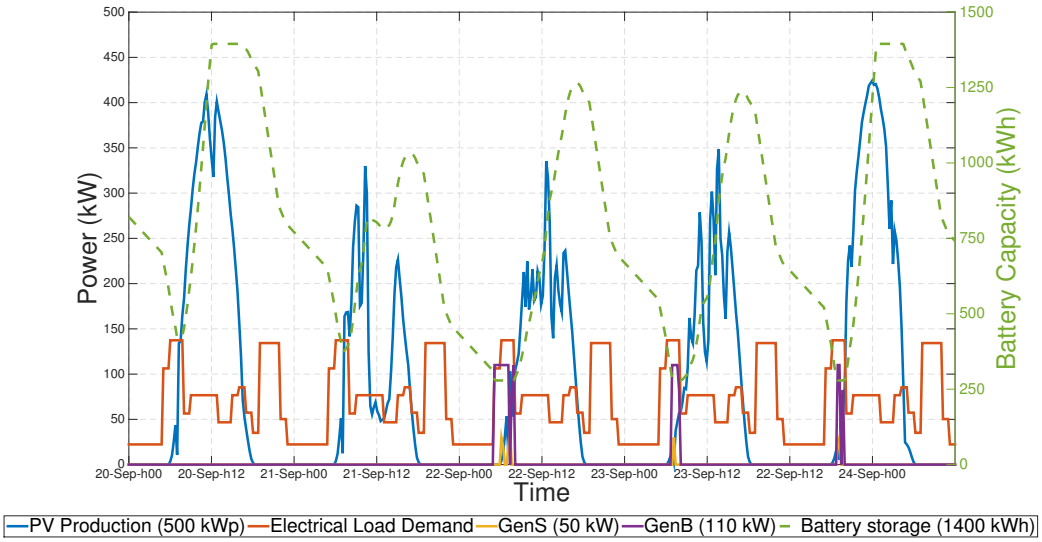

(a) Optimal configuration with electrical storage

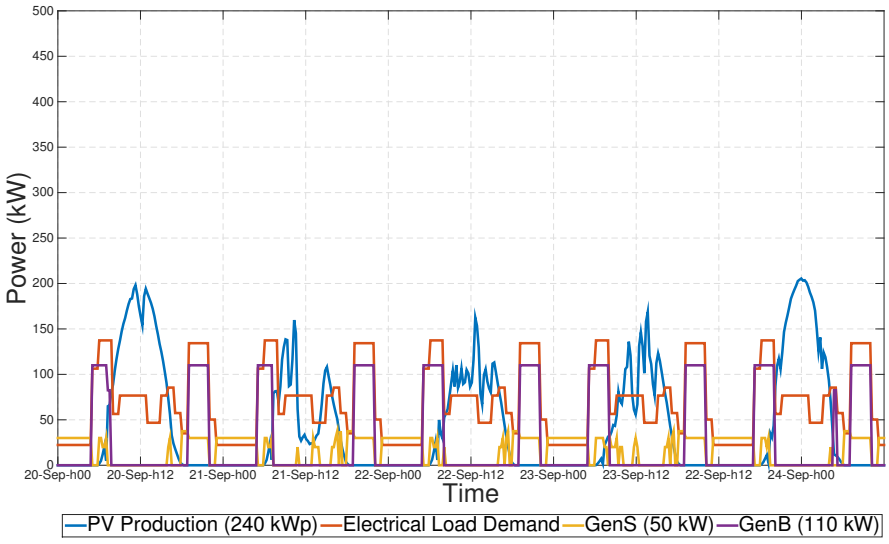

(b) Optimal configuration without electrical storage

Figure 4.6: Operation of optimal configurations from 20th to 24th of September 2004

4.3 Sensitivity Analysis

At the end of the simulation, results are shown with some other data concerning the economic analysis of the energy system considering different variation of some critical parameters. This evaluation is called Sensitivity Analysis and it takes into account the potential variation of data that might change

along the lifetime of the designed energy system. One of the first steps of the software (see Figure 3.5), requires the integration of data concerning Sensitivity Analysis. The parameters that may be changed are listed below.

- Interest rate of the country,
- Energy from grid cost *(only for on-grid systems)*
- Energy to grid price *(only for on-grid systems)*
- Fuel cost *(only for off-grid systems)*
- Battery lifetime
- Battery capital cost

Sensitivity analysis is an useful tool to understand the impact of these critical parameters variation on the proposed model and to have a wider overview of the future energy system operating function and costs. Within this section, the Sensitivity Analysis concerning the case study of the off-grid hybrid system in Uganda, shown in Section 4.1, will be presented. The case study in Uganda shows results that have been obtained considering a diesel cost equal to 1 $/l, interest rate of 11 % and battery storage capital cost and lifetime amounting 250-350 $/kWh and to 4500 charge/discharge cycles, respectively. Diesel price, for instance, might vary significantly within short time period because of unpredictable social and political causes, the interest rate might change its value for economic reasons and eventually the lifetime of the battery storage is defined by the manufactures within a certain range and not as a specific value. Since the capital cost and lifetime of the battery storage varies depending on the different manufactures and technologies, their values might significantly affect the TLCC of the system, and therefore they are considered crucial parameters for the design process of the optimal hybrid system.

4.3.1 Effect of diesel fuel cost variation

According to [72], the diesel in Uganda had an increase in price of around 145 % in 21 years, from 0.55 $/l in 1991 to 1.35 $/l in 2012 and in 2016 it is equal to 1 $/l. This data can be reasonably used to infer that the diesel price will not keep constant for the entire lifetime of the dimensioned hybrid power system. Consequently, within the sensitivity analysis, the diesel price is supposed to increase proportionally during the lifetime of the system by 50, 80, 100, and 150 %. The effect that these variations in diesel price have on the TLCC of the optimal hybrid power systems with and without electric storage during their entire lifetimes are illustrated in Figure 4.8. It is clearly observable that the optimal system configuration without electric storage is largely more affected by the variation of diesel price because of the greater usage of generators and the configuration with electric storage seems constant with diesel price variation, even if is not, due to the slight increase compare to the

one without storage. In particular, the TLCC of the optimal hybrid systems with and without electric storage would have an increase of 4.3 % and 36.2 %, respectively, if the diesel price raised of 150 % from the current value (1 $/l), which means that the impact of diesel price variation on the system with storage is 8 times smaller than the one without electric storage.

4.3.2 Effect of interest rate variation

The trend of the interest rate in Uganda during the past decades had large variations to high values compared to the current one. Therefore the sensitivity analysis is implemented considering three higher and one smaller values of the current interest rate. The effect of the interest rate on the TLCC of the two optimal hybrid system configurations is shown in Figure 4.9. Similarly to Figure 4.8, the system without electric storage is more affected by the variation of interest rate, due to its higher yearly cost. From Figure 4.9 is visible how the gap of costs between the two configurations is affected by the interest rate variation; this gap decreases with increases of interest rate and the two system have a TLCC more and more similar.

4.3.3 Effect of battery bank lifetime and capital cost variation

In Figures 4.10 and 4.11 are illustrated the values of TLCC over 25 years for the optimal configuration of hybrid system with electrical storage evaluated for different values of battery lifetimes and capital costs. The lifetime of the battery slightly affects the TLCC; in the first case of 3000 hours, for instance, the storage will be replaced 4 times during the lifetime of the system, and this will increase its TLCC. Nevertheless the residual cost takes into account the net value between the disposal cost and the value associated with the system at the end of the system operating period. This consideration implies that when the battery lifetime is equal to 4600 or 5000 or 6000 hours and, during the 25 years the storage is replaced once in all the cases, the TLCC decreases with the increasing lifetime value because at the end of the survey period the battery will worth as much its lifetime is longer.

On the other hand, the capital cost of the battery storage strongly affects the value of TLCC. Due to the high variability of the battery capital cost, depending on the manufactures, technology and size, the sensitivity analysis is evaluated within a wide range of battery costs, from one third to the three times the price considered in the simulation (300 $/kWh). Figure 4.11 shows that the TLCC of the hybrid system with electric storage can exceeds the TLCC of the system without storage when the price is bigger than about 700 $/kWh. The capital cost of the battery bank can condition the hybrid system configuration (with and without electric storage), while its lifetime can varies without influencing this choice. Figure 4.10 shows indeed that even with the smallest value pf battery lifetime, the TLCC of the system with storage is smaller than the case without storage. This means that the price of the electric storage can be considered a crucial parameter for the economical evaluation of the power system and its value has to be accurately chosen from reliable manufacturers.

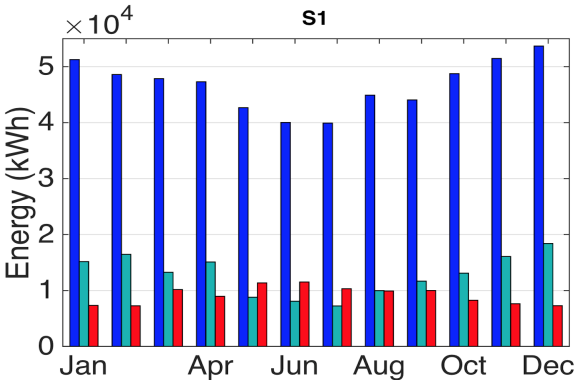

(a) Hybrid system with electric storage (S1)

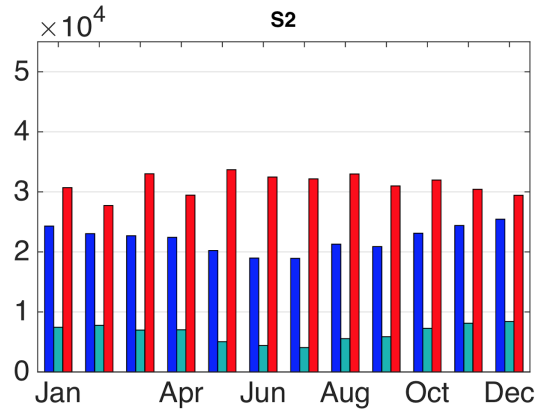

(b) Hybrid system without electrical storage (S2)

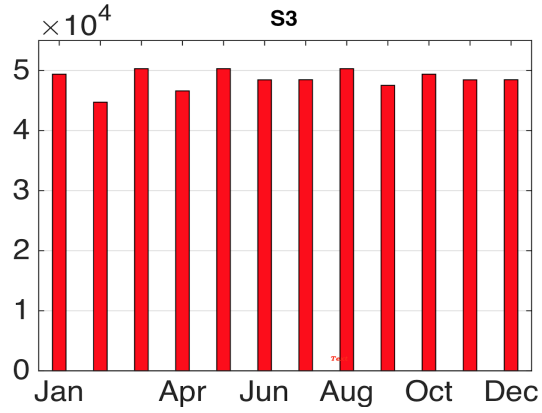

(c) Current generator system (S3)

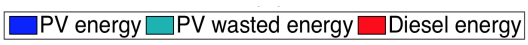

Figure 4.7: PV array energy, PV wasted energy and diesel generator energy of each month

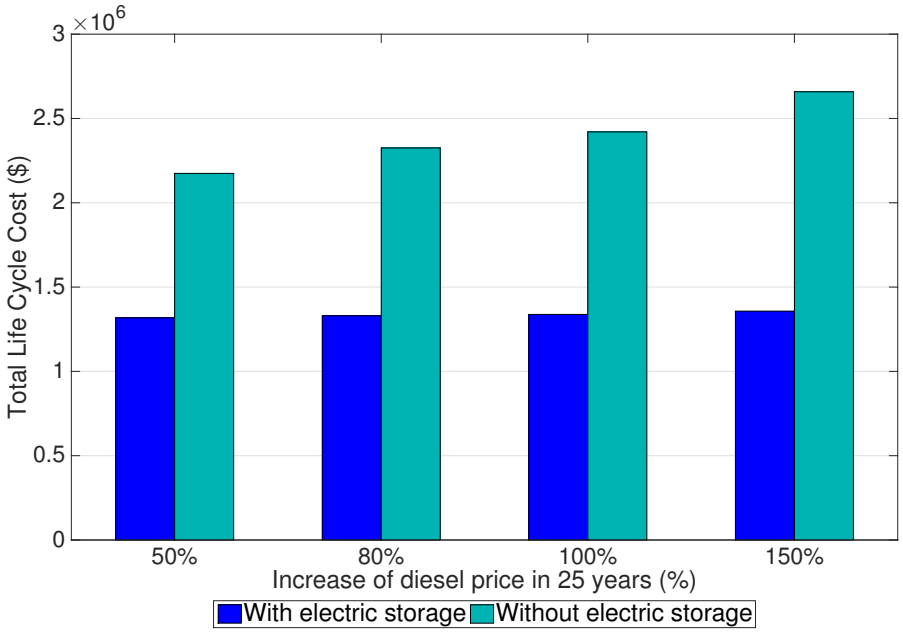

Figure 4.8: Total Life Cycle Cost of the two optimal hybrid systems affected by diesel price variation.

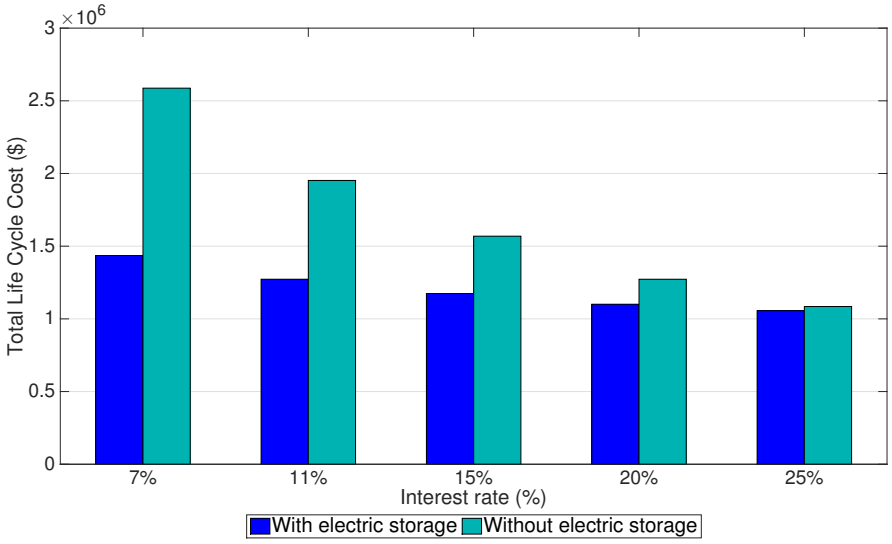

Figure 4.9: Total Life Cycle Cost of the two optimal hybrid systems for different values of interest rate.

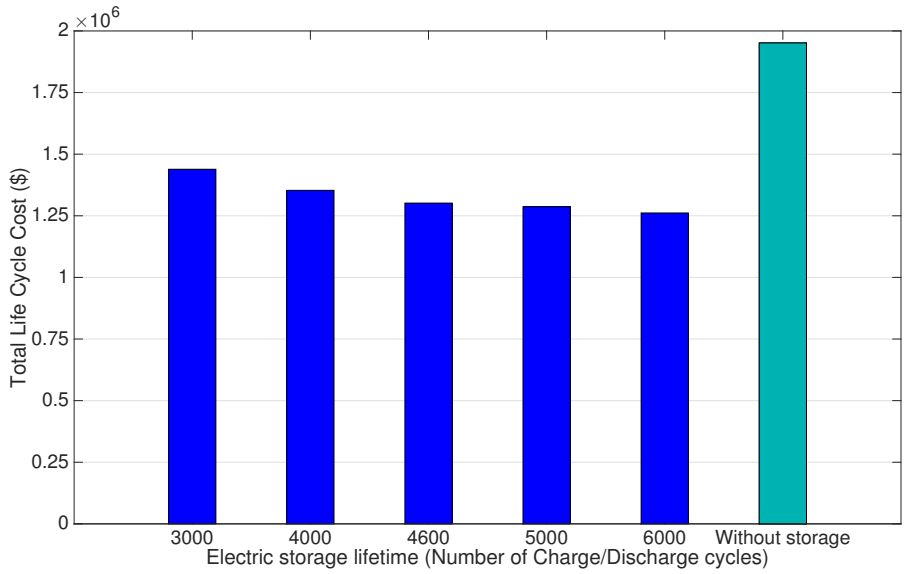

Figure 4.10: Total Life Cycle Cost of the optimal hybrid system for different values of battery storage lifetime. (Capital cost equal to 300 $/kWh)

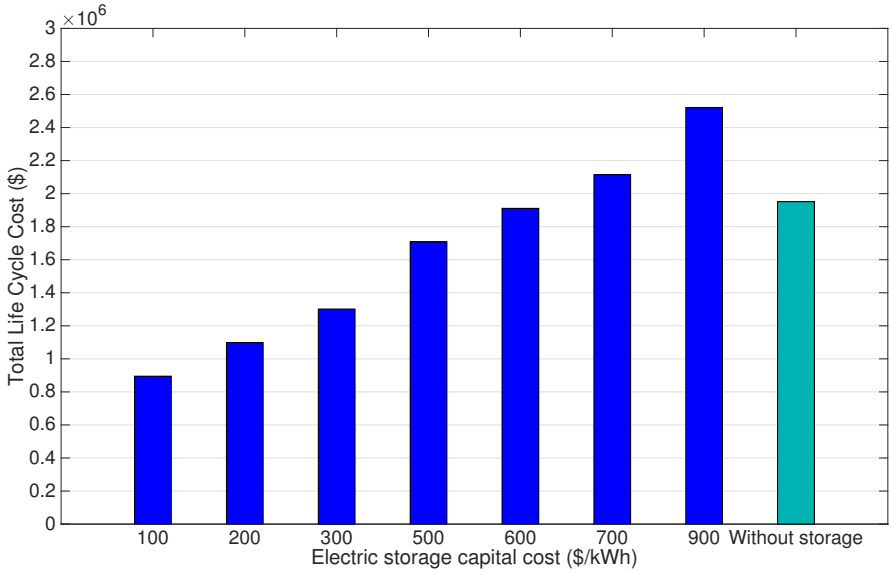

Figure 4.11: Total Life Cycle Cost of the optimal hybrid system for different values of battery capital cost. (Lifetime equal to 4'600 cycles)

5

Solar Prediction

One of the elements that may be useful to reach the goal of improving the hybrid energy system efficiency is the development of an instrument able to make a reliable prediction of PV production. An hybrid energy system able to maximise the electric consumption during the hours of maximum PV production can further improve the renewable fraction, to unload the storage operation, spreading out its the lifetime along the lifetime of the system, and last but not least, decreasing the consumption from the grid and from the backup system.
Meteorological conditions are decisive in solar plant management and electricity generation: any increases or decreases in solar radiation mean a plant has to adapt its operation method to the climatological phenomena. An unexpected atmospheric change can provoke a range of problems related to various solar plant components affecting the electricity generation system and, in consequence, causing alterations in the electricity grid. Therefore, predicting atmospheric features is key to managing solar plants and is therefore necessary for correct electrical grid management. The current impossibility of predicting the supplied energy leads to the necessity to find out an instrument to predict the solar radiation with a small margin of error compare to the existing ones. As a consequence of the recent changes in the Italian legislation about photovoltaic systems, the need of installing small size plants directly connected to the users has been increased during the last years.
Part of this thesis project points out how important is to be able to build energy systems based on the real request of supplied energy and to maximise the self consumption of energy decreasing the costs of grid duties and avoiding imbalance in the grid, especially during the distribution phase. The prediction of supplied energy from photovoltaic systems is one of the biggest challenges for the achievement of future smart grids, which represent the smart system to organise in a preventive way the in and out electric energy flows, avoiding technical and economic damages due to imbalance and

not programmed power flows. It is known that with a decentralised system would be easier to control those power flows but it is necessary to have the use of instruments with a smaller margin of error compare to the current ones. Concerning smart grids, the instrument able to predict the generated power might be installed by the local grid (district, town) in order to supply and exchange information with others single plants.
Furthermore, the combination of an accurate system to predict photovoltaic production and a hybrid energy system, would lead a power system to be able in ensuring a higher RE fraction with a smaller PV plant and a globally cheaper energy system compared to a hybrid system without solar predictor. The implementation of storage systems and solar predictor on a PV systems would reduce the imbalance in the electricity grid, shaving the load peaks and levelling off the electricity demand and supply trends. Within this thesis a deep study of the state of art of a solar prediction has been made and the most relevant and recent studies have been described in Section 5.1. Results and future research activities are shown in Section 5.2.

5.1 State of Art

A state of art about clouds detection and forecasting studies developed by research groups in the past decade through different techniques and instrumentation availabilities has been reported in this thesis. Most of the projects are carried out by the use of a camera developed by the Yankee Enviromental Systems, called Total Sky Imager (TSI), [49–55] A similar camera, called Whole-Sky Imager (WSI) has been developed by the Climate Research Facility (U.S. Department of Energy) for assessing and documenting cloud fields and cloud field dynamics. Some other works are implemented with a simpler and more economically feasible instrumentation, as a normal digital camera with no shadow band [56–59].

5.1.1 Cloud detection using a commercial camera without sun shadow band

In 2005, [59] tested different texture feature extraction approaches for automatically training a classifier system to recognise five different classes of clouds:

- Cumulus
- Towering cumulus
- Cumulo-nimbus
- Clear sky
- Other clouds

The authors claimed that "no feature extraction method is best suited for recognising all classes" and they suggest five different extraction methods: (i) autocorrelation, (ii) co-occurrence matrices,

(iii) edge frequency, (iv) Law's features, and (v) primitive length. Once the image is classified by an expert, a texture feature vector is extracted from each region that describes its surface properties. These feature vectors are used to teaching a classifier to learn characteristic patterns associated with corresponding classes. The classifiers used for identifying cloud types are the *k*-nearest neighbour and neural network. The test was made on 122 images using a color digital camera, bitmap format with a resolution of 720x576 pixels and converted into grey scale format with 256 grey levels. Images were segmented into separate regions on the basis of four image segmentation methods: (i) fuzzy c-means clustering (FCM), (ii) region split and merge, (iii) seeded region growing, and (iv) histogram-based thresholding. The authors found out that the FCM algorithm performs the best on cluster validity index and also the segmented regions correspond well with experts visual interpretation of distinct regions. In order to identify region boundaries (since they are not smooth on FCM segmented image due to its noisy nature), median filtering is applied to remove the noise in segmented images. Once that the boundary information is extracted, by the use of Susan algorithm, the texture features are extracted from the complete segmented regions using each of the chosen feature extraction methods and they are mapped in a text file, called map file, to generate the feature set containing each region as a row vector appended at the end with its class name. Eventually the feature sets are presented to the classifier for the analysis.
The use of the *k*-nearest neighbour classifier has shown that the cumulus clouds are the easiest to recognise, whereas the recognition of towering cumulus and other clouds is poor. In particular, cumulo-nimbus clouds are recognised with an accuracy of 83.3% correct, towering cumulus with 79.6%, cumulus clouds with 86.3%, and clear sky with 31.2%. These results are compared with those obtained using linear discriminant analysis and the authors found that the *k*NN classifier significantly outperforms the linear method. In order to improve the performance of the classifier, a rejection threshold has been used. The classifier automatically uses a threshold to filter image samples on which recognition must be performed, giving a better recognition rate on a smaller subset of the test data. Samples considered difficult for the analysis have been labeled by human observers.
The authors have also demonstrated a pilot study on the recognition of clouds using neural networks and, in particular, they have used a simple back-propagation with momentum based network for cloud classification using Stuttgart Neural Network Simulator where the number of input nodes is feature-set dependent. They claimed that the quality of the results depends on three factors: (i) quality of segmentation, since clouds do not always have a sharp contrast near the boundaries for an accurate segmentation and the quality of texture features is likely to suffer; (ii) the quality of image data, and (iii) quality of the experimental set-up.
Conclusions of this project are that the use of multi-stage classification can yield better results rather than training the classifier on all classes at time. Using multi-stage classification a number of classifiers can be trained that separate classes in an interactive manner.

In 2006, [56] used a professional digital camera (model PCS20232) mounted on the roof of a

building and connected to a PC for data acquisition and storage. The images were collected on a 24-bit red-green-blue (RGB) JPEG format at a resolution of 640x340 pixels. Since images were shot with the field of half view (36°) pointing to the camera's zenith, the instrumentation did not have a shadow system on the camera lens because the solar elevation never reached an angle high enough to let the direct solar beam reach the camera lens. The presented methodology takes into account the different wavelengths captured by the the camera and encompasses the transformation of images from RGB color space to the intensity, hue, and saturation (IHS) space. The authors claim that clouds have high reflectance and show color shades varying from blue to red diluted in a white matrix, which characterises a mix of several wavelengths. A clear sky shows manly blue tones, with color shades ranging from green to red which typically results in high saturation values. The pixel classification is based on the observation that colors with high saturation are said to be pure, such as clear skies; and colors with low saturation (much grey) are pastel colors, such as clouds. Three classes were defined to classify image pixels: clear sky, cloud sky, and undefined. The classifying algorithm is the simplified parallelogram, where each class is represented by an upper and a lower threshold for each attribute used in the classification process. A pixel is then classified as belonging to a class in a region whose attributes are within predefined ranges between the upper and lower threshold of each attribute. To determine these thresholds, the average and standard deviations of the values of the saturation attributes were used in the training area. This type of training works only if averages of each class are well separated.

- a pixel belongs to the class "cloud" if $x < \mu_n + 3\sigma_n$,
- a pixel belongs to the class "clear sky" if $x > \mu_c - 3\sigma_c$,
- a pixel belongs to the class "undefined" if $\mu_n + 3\sigma_n \leq x \leq \mu_c - 3\sigma_c$

This simple method was tested by using a package of 29 images with different situations of cloud cover and the results show that the method was capable of defining the cloud cover status with an accuracy of better than 94% for clear skies and 99% for cloudy skies. These accuracies were determined from the percentage of pixels that the algorithm correctly identified according to human observers. The classifier produces an overestimation for low values of cloud cover in comparison with that of the observer's.

In 2010 [57] developed an automatic algorithm based on a set of mainly statistical features describing the color as well as the texture of an image. This work distinguishes seven different sky conditions:

- High thin clouds,
- High patched cumuliform clouds,
- Stratocumulus clouds,

- Low cumuliform clouds,
- Thick clouds
- Stratiform clouds,
- Clear sky

The images used to develop the algorithm have been taken through commercially available components, designed to be location-independent and run during adverse weather conditions. The basic component is a digital camera equipped with a fisheye lens to provide a field of view larger than 180°, enclosed by a water and weather resistant box. The camera is programmed to acquire one image every 15 seconds, store in 30-bit color JPEG format with a resolution of 3648x2736 pixels. The whole sky mapped is circular where the center is the zenith and the horizon is along the border. In order to acquire data of a wide rage of possible sky conditions and solar zenith angles, images have been taken in different climate zones in several seasons. The final image set used to train the cloud type classifier consists of 1'500 selected all-sky images from the 75'000 obtained. This image set includes a large variety of different cloud forms as well as image of different daytimes and consequently different states of solar zenith angle. In order to classify the images the k-nearest-neighbor (kNN) is chosen. It has been shown in [59, 73] that, in the specific field of cloud type recognition, some results for comparison with liner classifiers and neural networks underlines the high performance of kNN classifiers. This method is supported by the authors also because is very simple (low computational cost) and quite powerful. The assignment of an image to a specific class using kNN classifier is performed by majority vote. After pre-processing, several spectral and textural features are extracted from an image. In the following step, the computed and normalised feature vector x is compared with the known feature vectors x^i of each element in the training data by means of a distance measure (in this work the manhattan Distance has been used). The class associated with the majority of the k closest matches determines the unknown class. The pre-processing step consists of excluding the interfering regions by the use of a location dependent image-mask. Thereafter the remaining area is divided pixel by pixel into clear and cloudy regions, utilising their red and blue pixel values. Differently from previous works [74, 75] where the ratio R/B has been used to differentiate these areas, the present work considers the difference R-B, since the comparisons showed that segmentation using such a difference threshold still results in minor errors, but outperforms the ratio method. The optimal threshold that has been found for this application equals to R-B=30. The authors selected 12 features and the choice was based on the Fisher Distances F_{ij}^x, a selection criterion used in cloud classification work relating to satellite images presented in 1995 by [76]. The features best suited to separate the defined classes are those which have the largest Fisher distances. The selected features are the following:

- Seven spectral features (describe the average color and tonal variation of an image):
  - Mean R and Mean B

  - Standard deviation (B)
  - Skewness (B)
  - Difference (R-G, R-B, and G-B)
- Four textural features:
  - Energy (B)
  - Entropy (B)
  - Contrast (B)
  - Homogenity (B)
- Cloud cover

In order to identify the textural features Grey Level Co-occurence Matrices (GLCM) have been used. A GLCM is a square matrix for which the number of rows equals the number of grey levels in the considered image. Every matrix element represents the relative frequency $P^{\Delta}(ab)$ that two pixels occur, separated in a defined direction by a pixel distance $\Delta = (\Delta x, \Delta y)$, one with grey value a and the other with grey value b. For each pre-processed image the presented features have been computed and stored with their assigned cloud class. To estimate the performance of the selected features and the created algorithm, the authors applied the Leave-One-Out-Cross-Validation (LOOCV) that, in cloud type recognition, it has been applied also by [77, 78]. The main results reported an accuracy of about 75% on a test run of random images. The best recognised classes were clear sky and cirrus, while confusions between cirrus and cumulus occurred primarily in case of low cloudiness. This is caused by thin and transparent parts of cirrus clouds which cannot be detected by the algorithm and, consequently, such images are classified as clear sky. Another error occurs between stratocumulus, stratus and the class of thick clouds; these classes appear frequently as transitional forms from one on the other and the automatic classification can be difficult. Furthermore, misclassification of some images displaying stratus and thick clouds appear to be caused by raindrops on the camera protecting dome. The drops are naturally also mapped on the image and lead to texture feature values similar to those representing patchy altocumulus and cirrocumulus.

Based on the result obtained by [57] , in 2012 [58] has improved the algorithm previously proposed using a multi-color criterion for the determination of total cloud coverage, taking into account also the visible percentage of sun and including a solution for the recognition of rain drops in the digital images. The images used in this study have been collected by the use of a commercial compact digital camera set on a building roof, a fish-eye lens (field of view=180°) and a water and weather resistant box with a glass dome and connected to a PC for external automated control. The camera is programmed to acquire one image every 5 minutes, stored in 8-bit JPEG format with a resolution of 640x480 pixels. No shadowing mechanism for obscuring the direct solar radiation is used. The areas

close to the horizon are identified and excluded from further analysis and images do not include solar zenith angles below 10°. A dataset of 50'000 images collected in 2 years has been used to implement this study. This method is mainly based on the starting point that "color is the primarily property that allows the visual detection of clouds on the sky" and that the use of a ratio or a difference of R and B intensities results in errors for cases of broken or overcast cloudiness under large solar zenith angles, as it has been shown is previous work [57, 75, 79]. The propose cloudy pixels detection is based on three threshold including the value of the G intensity:

$$B < R + 20 \quad \& \quad B < G + 20 \quad \& \quad B < 60 \tag{5.1}$$

Three images with thin, thick and overcast thick cloudiness have been taken to compare this method to the R-B criterion exposed in [57] and for all the cases the multi-color criterion gives better results in the cloud cover recognition. The authors claim that, although the use of a multi-color criterion could generally improve the accuracy of the total cloud cover from a digital image, the detection and identification of very thin cirrus or cumulus is still problematic. Another uncertainty of the presented method is the pixel discrimination in the areas close to the sun. The study proposes to convert the original image into a full scale color image and to isolate high color density pixels (corresponding to those close by the sun) and to apply the a threshold for the detection of pixels that do not contain the solar disk. The following threshold is based on the visual inspection of several images:

$$R < 140 \quad \& \quad R > G + 70 \quad \& \quad R > B + 120 \tag{5.2}$$

When the sun is totally visible or not visible at all are the cases when the image can be successfully detected, while the accuracy of the method when the sun is partially covered has not been confirmed yet. By the way, the overall error, due to the presence of clouds close or in front of the sun, is estimated to be less than 3% of the total cloud fraction. The proposed method uses the same cloud classification proposed in [57] (6 classes of clouds + clear sky) and the same cloud classifier based on the k-Nearest-Neighbor Method. The slight difference is that three of the four textural feature have been used, leaving out the feature called "entropy" because its value seemed to have a negligible effects on the results.

An interesting improvement of the algorithm of [57] is the detection of raindrops in the images. It has been observed that raindrops standing on the perimeter of the hemispheric dome, distort the circular shape of the perimeter of the image. The "circle factor" CF is so evaluated through the equation $CF = 4\pi A/P^2$, with P is the perimeter and A is the area of the image. A perfect circle has CF equal to 1, the images without raindrops present a CF equal to 0.88 (this value is considered a reference number for the specific camera and specific location) and when raindrops are present, CF is lower than this reference value suggesting the presence of rain and consequently the identification of certain cloud types. This method could lead to false conclusions when the sun is close to the horizon, when raindrops stay on the dome for long time although the weather conditions have been improved,

and during cases with morning drizzle.

Furthermore, this work created a number of subclasses for every cloud class: for every image of each cloud class all the 12 features were measured and than separated in sub-classes based on the value of the following three parameters:

- Solar zenith angle: $< 40, 40-65, > 65°$
- Cloud coverage: $< 3, 3-6, 7-8 \quad octas$
- Visible fraction (%) of the solar disk: $< 20, 20-80, > 80$.

The final number of subclasses depends on the cloud class:

- Stratus-altostratus: 4 sub-classes
- Cumulonimbus-nimbostratus: 6 sub-classes
- Cumuls: 8 sub-classes
- Cirrocumulus-Altocumulus: 9 sub-classes
- Stratocumulus: 10 sub-classes
- Cirrus-cirrostratus: 12 sub-classes
- No sub-classes for clear sky

According to this presented method, 83% and 94% of the analysed images agree within ± 1 and ± 2 octas respectively with visual weather observations at a close-by meteorological station. The total cloud cover could be significantly underestimated only when thin cirrus clouds appear.

5.1.2 Cloud detection using a Total Sky Imagery (TSI)

In 2011, [49] presented an interesting study on the classification of different sky conditions considering the attenuation of direct solar radiation. This attenuation has been quantified according to a dimensionless index k_b, obtained from radiation data and images taken from a full-color sky imager system TSI-880. Images have been used to characterise the situations associated with the different values of k_b. The data images were taken for an entire year in order to guarantee a complete range of seasonal conditions, the sampling period was set to 1 minute to detect fast changes in cloud cover and radiation data were simultaneously registered by the use of pyranometers. The radiometer domes and the TSI-880 were cleaned on a daily basis and the radiation quality.control processing applied was the following:

- Check and discard missing or negative values of solar radiation
- Check and discard solar global or direct solar radiation values higher than solar constant

- Check and discard diffuse solar radiation higher than global radiation

In addition, data logger were synchronised to achieve an homogenous database.
This study characterises the cloud cover according to the levels of direct solar radiation attenuation using the beam transmittance index k_b. This index is evaluated as the ratio of direct solar radiation (B_n) to the extraterrestrial radiation (I_{0n}).

$$k_b = \frac{B_n}{I_{0n}} \tag{5.3}$$

The extraterrestrial radiation is calculated through the following equation:

$$I_{0n} = I_{sc} \cdot E_0 \tag{5.4}$$

where I_{sc} is the solar constant and E_0 is the eccentricity (a parameter that considers sun-earth distance during the year). High k_b values were associated with clear sky conditions, whereas low values of k_b might have been due to either overcast skies or scattering caused by aerosols.
The calculation of k_b was performed over the whole radiation database and all the TSI images were classified according to the resulting k_b values at the moment of their capture. The image classification process is the following:

1. For a given minute, direct solar radiation measured is used to calculate the k_b index,
2. The all-sky image captured in that minute is classified in a group depending on the k_b value,
3. Images were also checked to create an additional set of cloudless sky situations.

All images were grouped in four attenuation group corresponding to different k_b thresholds selected for the classification. The next step was to extract the most common features of each group that could be detected in the image, these features include the form, color, size, opacity, edges and type of clouds. The attenuation groups were divided as follow:

- Group 1, G1 ($k_b < 0.2$) - Altocumulus, Nimnostratus
  The attenuation produced in direct solar radiation by G1 clouds is over 80% and is mainly due to the presence of very opaque clouds blocking the sun's disk. The authors found that such levels of attenuation is caused by clouds with several different features, as Figure 5.1a shows. Within this group altostratus clouds appear Figure 5.1a (A) with a hazy and slightly blue base as well as nimbostratus Figure 5.1a (B) characterised by a dark grey base. The clouds classified within this group cause a strong attenuation and at time close to noon the direct solar radiation reaching the surface is also negligible. The authors observed this attenuation measuring the direct solar radiation when G1 clouds are observed, the resulting radiation can be seen in Figure 5.1b.

- Group 2, G2 ($0.2 < k_b < 0.4$) - Cirrostratus, Altocumulus, Cirrus castellanus
  This group is characterised by mid-level and high-level clouds, they attenuate direct solar

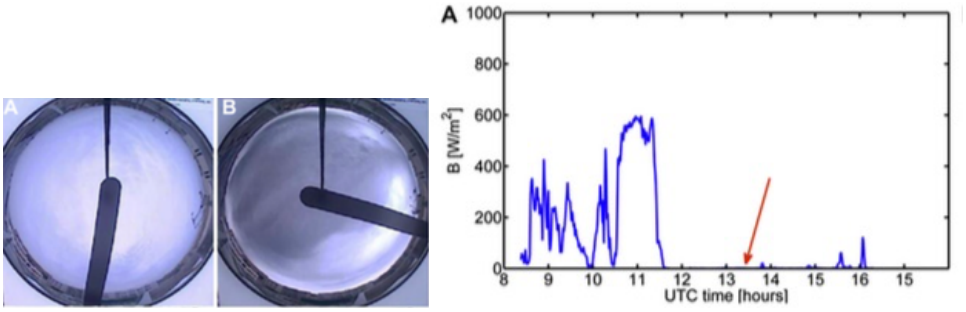

(a) Images from TSI-880 *(b) Direct normal radiation*

Figure 5.1: Attenuation group 1 and corresponding direct normal radiation, [49].

radiation between 60% and 80% and different sky conditions can be found, see Figure 5.2. One type of clouds is the cirrostratus Figure 5.2C, thin, uniform and whitish clouds where the sun can shine trough. Another type of clouds that show a similar attenuation is altocumulus Figure 5.2D which are small cloud with a cottony appearance, characterised by globular masses with individual elements that are slightly smaller, less dark, and more ordered than other types included in this group.

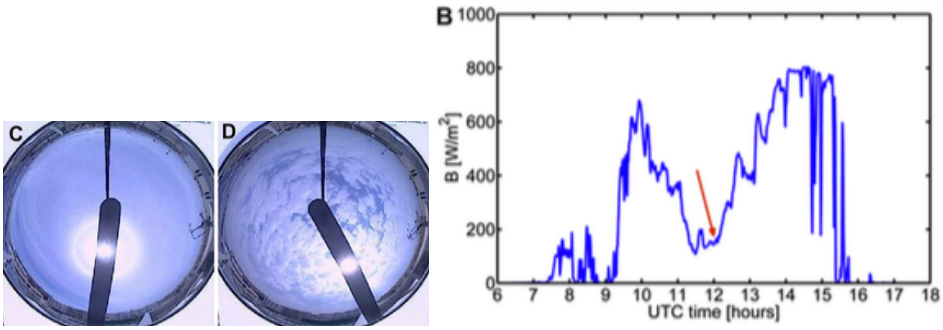

(a) Image from TSI-880 *(b) Direct normal radiation*

Figure 5.2: Attenuation group 2 and corresponding direct normal radiation, [49].

- Group 3, G3 ($0.4 < k_b < 0.6$) - Cirrus, Cirrostratus
  This group includes a variety of different cirrus clouds. In Figure 5.3E the cirrus clouds are thin, uniform and the sun can be seen through them, they might form halos, their color is whitish, edges are not well defined ("cottony" appearance) and normally they do not cover the whole sky. Figure 5.3F shows another type of cirrus included in this group: they are very thin and elongated blocking the sun's disk and producing mild attenuations, they are often accompanied by tufts and color is usually whitish.

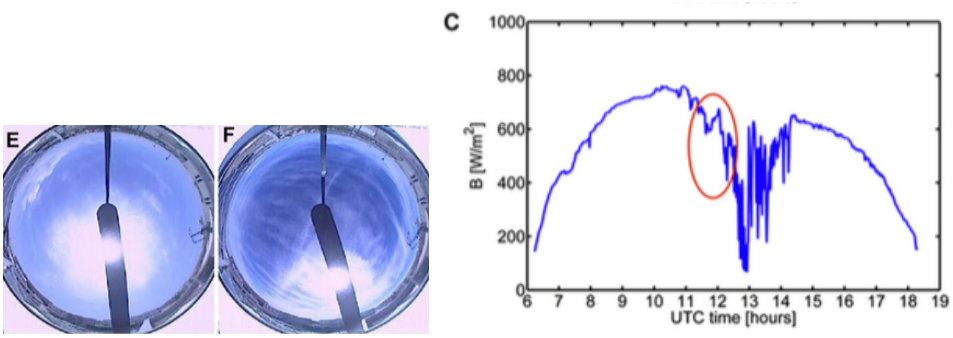

(a) Image from TSI-880 *(b) Direct normal radiation*

Figure 5.3: Attenuation group 3 and corresponding direct normal radiation, [49].

- Group 4, G4 ($k_b > 0.6$) - Cirrus fibratus, Altostratus
  Clouds included in this group are characterised by poorly defined edges and sometimes are too thin to be discernible and can be observed only when illuminated with direct or circumsolar radiation. Furthermore, there have been some special situations in which certain clouds increase the global radiation values to levels close to the extraterrestrial radiation, this type of clouds are generally Altostratus situated near the solar disk, their edges are well defined and are usually white broken clouds.

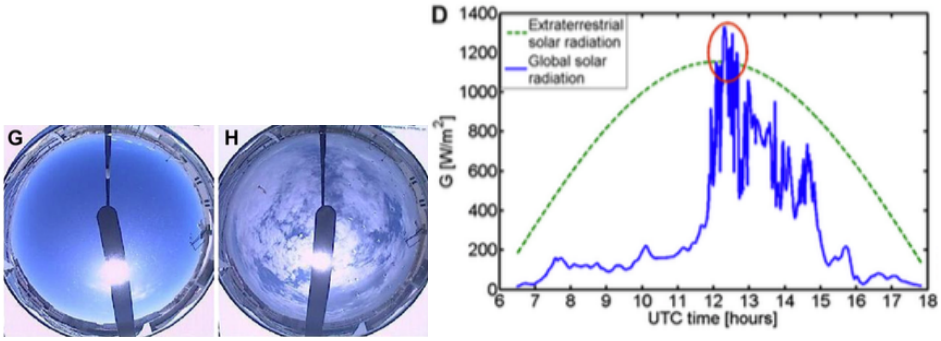

(a) Image from TSI-880 *(b) Direct normal radiation*

Figure 5.4: Attenuation group 4 and corresponding direct normal radiation, [49].

Finally, two frequency analysis were conducted: (i) the occurrence of each sky condition was examined both along the entire study period and seasonally, and (ii) the duration of another frequency study for the duration set.

In 2012, [55] classified digital images of sky pixel by pixel into clear sky, optically thin and

optically thick clouds. A new algorithm was developed to compare the pixels Red-Blue Ratio (RGR) to the RGR of a Clear Sky Library (CSL), generated from images captured in clear days. Thresholds for clear and thick clouds were chosen based on training image set and validated with set of manually annotated images. Images were taken with a TSI-440 every 30 seconds for seven months, with a resolution of 640 by 480 pixels and, within each image, pixels at a Filed of View (FOV) greater than 140° were excluded due to distortion. Since the value of the Aerosol Optical Depth (AOD) affects the channel magnitudes of the camera, a Haze Correction Factor (HCF) is added to account this effect on the RGR values.
The diagram of the presented cloud detection and opacity classification (CDOC) algorithm is illustrated in Figure 5.7. The image RBR and CSL RBR are input, the HFC is determined, the $Diff$, $Diff^{HFC}$, Prt and Prt^{HFC} are computed and finally, based on the thresholds values, pixels are classified into clear sky, thin cloud and thick cloud classes.

The clear sky library, used to compare the RGR values and classify the sky images, provides reference RBR for each pixel and time from historical clear day images. The RGB intensities for each pixel are stored in a matrix as a function of Image Zenith Angles (IZA), Sun Pixel Angle (SPA) and Solar Zenith Angle (SZA) from historical images on a clear day. The CSL is updated on every clear day throughout the year because changing solar position and its projection on the TSI mirror and aerosol climatology affects RGB magnitudes and RBR.
A sample image and its RBR equivalent are shown in Figure 5.5a and b. Figure 5.5c shows CSL image obtained as a function of SPA and IZA for each pixel. A pixel is classified as thick cloud if the difference between the RBR and CLS ($Diff = RBR - CSL$) is greater than the thick cloud threshold. This difference value is calculated for each pixel and illustrated in Figure 5.5d.

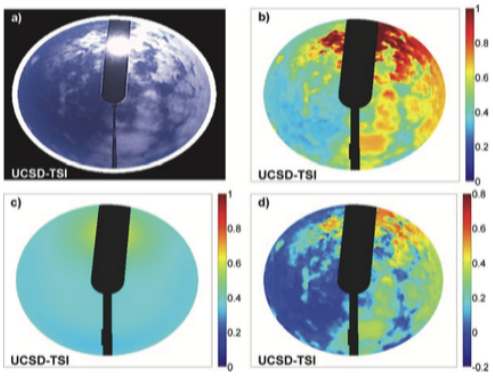

Figure 5.5: (a) True-color image captured by the TSI (b) RBR of the image for FOV$<$ 140°, (c) Clear Sky RBR generated from the CSL. (d) RBR difference (Diff) between image RBR and CSL RBR, [55].

Concerning the thin clouds, the authors claimed that more consistent threshold should be chosen to distinguish this second type of pixel clouds. If the CSL was generated on a day with small AOD and compare to a clear day with large AOD, the difference would have a positive value and the pixel

identified as a cloud. In orde to avoid this, a Haze Correction Factor (HCF) to the CLS is introduced. HCF has been determined iteratively at each time step as Figure 5.6 shows.

Eventually the difference between the image and the CSL corrected by the HCF is calculated as:

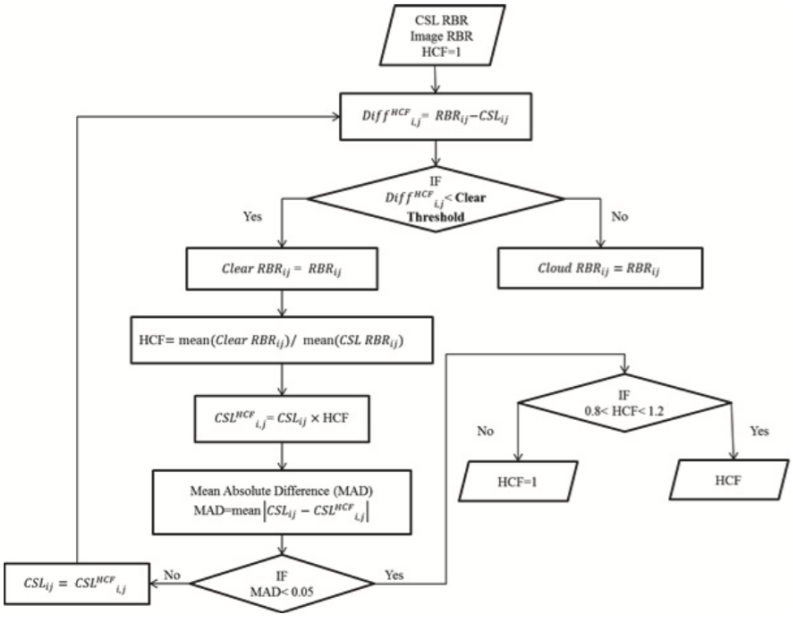

Figure 5.6: Flow chart for determining HCF which is executed pixel-by-pixel. The first box represents the initialisation of HCF, RBR, and CSL. Since the selection of clear pixels also depends on HCF, the HCF must be obtained iteratively. (i, j) denote the pixel number in the image, [55].

$$Diff^{HCF} = RBR - (CSLxHCF) \tag{5.5}$$

Another method to control the AOD effect was proposed by [80] with the introduction of the perturbation ratio, which is the ratio of the current pixel RBR to the CSL pixel RBR.

$$Prt = RBR/CSL \tag{5.6}$$

$$Prt^{HCF} = RBR/(CSL \cdot HCF) \tag{5.7}$$

The perturbation ratio was used only for thin clouds, not for thick clouds and the spatial variance in this perturbation was used to distinguish between heavy haze and thin clouds.

The thresholds for the three different sky conditions are evaluated through a training set of 60 images collected in 5 different days chosen to represent different atmospheric conditions. Each pixel in the image was manually classified into clear, thin, and thick clouds. The training set was used to

determine the thick cloud and clear sky difference threshold values through trial and error.

The diagram of the presented cloud detection and opacity classification (CDOC) algorithm is illustrated in Figure 5.7. The image RBR and CSL RBR are input, the HFC is determined, the $Diff$, $Diff^{HFC}$, Prt and Prt^{HFC} are computed and finally, based on the thresholds values, pixels are classified into clear sky, thin cloud and thick cloud classes. In order to evaluate the performance of the

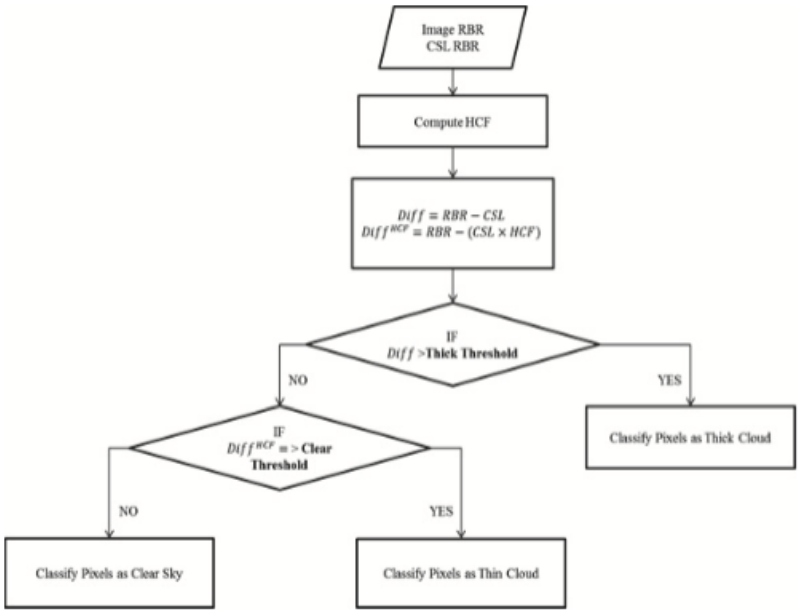

Figure 5.7: Flowchart of the CDOC algorithm which is executed pixel-by-pixel, [55].

CDOC algorithm based on both Diff and Prt, the authors used confusion matrixes with and without the application of the HCF for the three cloud classes. The results shown that the decision algorithm based on Diff outperforms the algorithm based on Prt. In particular, the Diff algorithm shown a high accuracy in classifying thick cloud and clear sky pixels, less than 2% of clear pixels were classified as thick clouds and less than 3% of thick clouds were classified as clear. On the other hand, results shown a smaller accuracy for pixels of thin clouds even with the introduction of the HCF. This low accuracy is partly related to the biases in the manual classification due to human error since it is hard to delineate the cloud edges of thin cloud that usually have gaps of clear skies and do not have uniform textures.

In conclusion, this method provided a significant improvement over the TSI's original software in pixel classification accuracy; the HCF, method avoided the need to constantly adjust the threshold values for cloud classification. Eventually, it has been shown that using the difference between the image RGR and the CSL's RBR to identify pixels rather than the ratios, provides better results.

In 2014, [50] presented three different models based on previous sky classification using radiometric data and representative sky conditions parameters in order to obtain accurate image processing and to classify different types of sky in cloudless, partially-cloudy and overcast.
The detection and analysis of clouds has been made from images taken by a TSI-880 camera, two pyranometers to measure the diffuse and global irradiance and a pyrheliometer to measure the direct irradiance installed in a two-axes solar tracker. The distance between the TSI camera and the solar tracker was less than 1.5 meter, data were collected every minute and the images were taken with a 352x288 pixel resolution. Data from 2010 to 2011 were used and the images were only collected when the solar altitude was higher than 5°.
The objective of the work presented by [50] was to compare the real radiation value, from real-time measurements, to a theoretical and reliable model of each radiation component (diffuse, direct and global) in order to determine the sky conditions. The real time measurement are I, D and G: direct, diffuse, and global irradiance. The theoretical values depending on the solar altitude, γ, and the the zenith angle, θ_z, were identified as follow:

- The direct normal irradiance (DNI) for clear skies:

$$I_{est} = 0.0040\gamma^3 - 0.6857\gamma^2 + 39.0661\gamma + 32.9153 \tag{5.8}$$

- The diffuse component estimation:

$$D_{est} = \frac{0.79 I_{sc} \cos\theta_z \tau_o \tau_g \tau_w \tau_{aa} 0.5(1-\tau_g)}{1 - m_a + m_a^1 .02} \tag{5.9}$$

  where I_{sc} is the normal incidence extraterrestrial irradiance, τ_o the ozone transmittance absorption, τ_g the uniform mixed atmospheric gases transmittance, τ_w the water-vapour transmittance, τ_{aa} the DNI transmittance due to aerosols and m_a is the relative optical air mass.

- The global horizontal irradiance:

$$G_{est} = D_{est} + I_{est}\sin(\gamma) \tag{5.10}$$

For a better evaluation of the sky conditions, two dimensionless indices were also used:

- Hourly diffuse fraction, k, defined as:

$$k = \frac{Dest}{Gest} \tag{5.11}$$

- Hourly clearness index, k_t, defined as:

$$k_t = \frac{G_{est}}{I_{sc} E_0 \sin(\gamma)} \tag{5.12}$$

where E_0 is the correction factor due to the eccentricity of the earth's orbit around the sun.

Generally, a high value of k value means that the atmosphere is not clear whereas a low mean value and a high value of k_t corresponds to cloudless sky while a low value supposes an overcast sky.
In order to identify whether the sky is cloudless, partially cloudy or overcast, the authors evaluated some ranges of values of the parameters k, k_t, I, D, G, I_{est}, D_{est} and G_{est} within which different sky conditions can be identified. These values were obtained by carrying out a complex study of modelling data, where the value of radiation components was extracted and the sky condition parameters were calculated.
The processing of images consisted of defining different value combinations from RGB and HSV color spaces. The values of RGB and HVS were divided into different blocks to correctly identify the pixels given that one pixel can represent either blue sky or a cloud white having the same RGB and HVS value. For this reason, other variables were introduced for identification of pixels such as GR-R, B-G, *dis* and solar altitude γ. The solar altitude is involved in the image processing because, depending on the time of the day, the RGB and HSV values change for the representation of sky or a cloud (for example the RGB value for blue sky is not the same for 10° as for 50°). The parameter *dis* is the distance of a pixel to the solar pixel it was calculated as follows:

$$dis = \sqrt{a^2 + b^2} \tag{5.13}$$

5.1.3 Solar radiation forecasting

In [51] is presented a study of cloud cover and short and medium-term solar radiation forecasting where cloudiness is predicted for the following three hours. The methodology is divided in two main blocks: one centered on cloudiness forecasting using remote-sensing techniques (Meteosat Second Generation satellite imagery) and the other on forecasting using sky-camera images combined with radiometric data. The prediction with a sky camera is carried out collecting an image every minute by the use of a TSI-880 and measuring the diffuse and global irradiance from two pyranometers and the direct irradiance from a pyrheliometer installed on a two-axes solar tracker. The forecasting process consists of three steps:

1. The images are processed to identify clouds
2. Three consecutive images were taken to study the cloud motion
3. The future scenarios to identify the cloud presence over the next three hours were reproduced

The clouds identification followed the methodology exposed in [50] where the sky is classified as cloudless, partially-cloudy, and overcast.
Since cloud motion behaviour depends on the cloud position in the image (clouds which appear at the image edges are further away than clouds appearing at the image center) the images are split into

sectors which can represent different types of cloud motion. The image is divided in four main areas observable in Figure 5.8:

- Red area: clouds that move slowly
- Green area: clouds that have intermediate motion
- Blue area: clouds that move quickly
- White area: clouds that are perpendicular to the camera mirror center

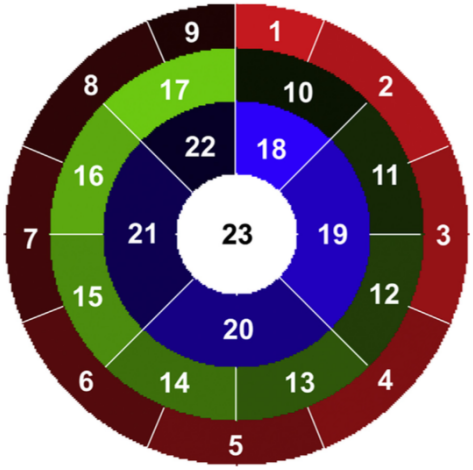

Figure 5.8: Sector divisions for sky-camera imagery, [51].

Each area was divided in 23 sectors: 9 sectors in the red area, 8 sectors in the green area, 5 sectors in the blue area and one sector for the white area. Three consecutive images were collected with a minute time step and one scene was made between the first and the second image, and another between the second and the third. Thun, each sector is analysed in one-minute sequence obtaining two possible vectors: $V_{sector,1-2}$ and $V_{sector,2-3}$. The motion identification for each scene is carried out using the Maximum Cross-Correlation method. The distance between the pixel position in the first image sector to that in the secondo image sector determines the cloud displacement and a total of 23 vectors for each sector were carried out. The authors claimed that unfortunately it is not always possible to generate correct cloud motion and three different quality tests were applied to confirm the motion vectors accuracy:

- Spatial coherence test: this test attempts to remove situations (with an error code) where sectors have an opposite displacement to the majority. In particular, the phase between $V_{sector,1-2}$ and $V_{sector,2-3}$ had to be lower than 60° to be considered in the calculations. This test was applied for each area, in the red area each sector had to have the same direction of its six neighbours,

while, for the green and blue areas, each sector had to have at least the same direction as at least seven neighbours. The white area is permanently covered by the shadow band and it was not considered in the calculations.

- Temporal coherence test: this test is focused on the detection of motion errors that occur when the cloud motion in the first scene is far lower than in the second. In particular if the difference between the vector coordinate of the first scene ,$V_{sector,1-2}$, and the vector coordinate of the second scene $V_{sector,2-3}$ is higher than 5 pixels, the vector is defined as incorrect.
- Final test: the final test is applied when vectors appear with an error code or with no displacement. The test procedure varies depending on the different areas of the image:
  - Red area: If the final vector within the red area has an error value, the mean value of the two adjacent sectors in the same area is assigned. If the final vector does not detect any movement it is necessary to check that there are no more than 7 sectors within the internal areas (green and clue) with the same value; if this occur the sky is cloudless and there is no motion, otherwise it is assigned the mean values of the two internal areas (green and blue) with a reduction of 20% to take into account the slower motion in the external area due to the mirror deformation.
  - Green area: If the final vector has an error value and the number of valid vectors in the green area is equal or more than 3, it is replaced by the mean of the valid vectors from the green and blu areas. If the number of valid vectors in the green is less than 3, the algorithm check that the total valid vectors in the green and blue are higher than 5, if this occur, the previous mean value is assigned; otherwise, cloudless sky condition are identified and the incorrect vector is substituted with the [0,0] vector.
  - Blue area: The incorrect vector is replaced by the mean of the valid vector from the green and blue areas. If the number of valid vector in the blue area is less than 2, the algorithm check if the number of valid vector in the green and blue area is higher than 5, in this case the mean value is assigned to the incorrect vector, otherwise, as in the green area, cloudless sky is assigned with the [0,0] vector.
  - White area: This sector has always the [0,0] vector since correspond to the area cover by the shadow band. The authors assign the mean vector of the blue area increased by 20% because the cloud motion in the white area is higher than in the rest of the image due to the mirror curvature.

Once the motion vectors have been defined for each sector, the motion vectors are reproduced to generate future scenarios. Since the frequency between the image is one minute, new motion vectors are determined every minute. In order to obtain the cloudiness forecasting to 180 minutes (3 hours) the motion vectors are applied to each sector 180 times to have three hours forecasting.

The results carried out with the methodology proposed by [51] shown a success probability of about 83% for the first 15 minutes decreasing to 60% for the next three hours, the authors claimed that this decrease is mostly due to the high cloud motion, provoking situations where the motion was so high that it caused problems with the image limits. Concerning the results on each individual sky condition, the results obtained over a period of an entire year presented forecasting success probability of about 83% for cloudless skies, 63% for partially-cloudy skies and 91% for overcast skies. The partially-cloudy skies are the most complex to analyse because the are fast-moving clouds, having many changes in DNI values in a short period of time, while the high success of overcast skies forecasting is manly due to the slow variation of the cloud motion.

One of the most recent work on short term solar forecasts is presented by [53] in 2013. The authors proposed and tested cloud-tracking methods for predicting future values of Direct Normal Irradiance (DNI) using processed images taken by the TSI-880 at one minute intervals and a pyrheliometer located within 5 meters of the camera for the DNI measurements. An interesting approach presented in this work is the transformation of the image from a spherical to a rectangular grid using a set of equations where the radial distance of solar position to the center of the image and the solar zenith angles have been used. In order to obtain the cloud velocity fields, the MPIV computer software has been used. The software was developed in 2003 by [81] and it uses particle image velocimetry (PIV) to create a vector field; it performed qualitatively well apart from the less defined clouds. PIV works by first setting up a grid of interrogation windows. The algorithms calculate how particles in each interrogation window move by comparing two images, in our case sequential frames of the video. This system can only work if the particles travel small distance between frames; if all the particles leave the interrogation window it can no longer accurately track them. Applying the PIV algorithm to each image, several velocity vectors have been computed depending on the local motions of cloud points and, in order to simplify the analysis, a representative vector have been chosen for each image by the use of k-means clustering on the distribution of velocity vectors. When the sky is cloudless, the velocity vectors of zero magnitude are computed. Once the representative velocity vector is chosen, from its velocity, the authors estimated the time that it takes for a cloud to pass through the observable range of the sky (seen by the camera) by taking the total number of pixels and dividing by the horizontal velocity (in pixels/mins).
Concerning the cloud pixel identification, the authors followed the adaptive threshold scheme approach presented by [82] in 2011 where the MCE (Minimum Cross Entropy) algorithm has been used. In [53] two modifications of the MCE algorithm have been applied compare to the previous study: an interval of values to define if the optimal threshold (τ^*) is satisfactory or not have been chosen and the the optimal threshold evaluation have been made not for the entire image but for each of the four regions in which the authors divided each image.
The solar irradiance is carried out through a construction of grid elements originating from the sun's position and orientated in the opposite direction of the cloud flow field, this grid orientation allows the

identification of cloud fraction for each grid element considering only the sky region useful for the irradiance forecast (the rest of the clouds does not need to be identified since will not cover the sun anyway). An example of element grid can be observed in Figure 5.9 where the element dimension is 20x20 pixels.

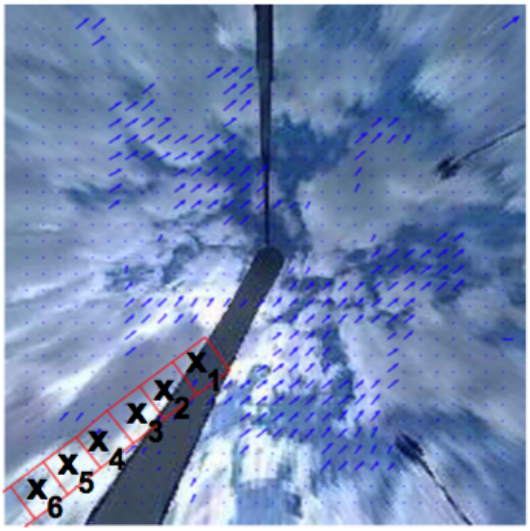

Figure 5.9: Each square indicate regions of interest where the cloud fraction is computed, [53].

The orientation of the grid elements allows for making solar forecast predictions at several time-horizons, for instance, the grid elements further away from the sun's position (X_5, X_6) may be more useful for longer forecast horizons. The number of element is obviously limited by the size of the image, and within this study up to 6 elements are used. An explicative example for this methodology is the following: if the average cloud speed is 10 pixel/min, then the grid element which contains the best information for a 5 minutes forecasting horizon should be a distance of 10 pixels/min x 5 min = 50 pixels. This distance corresponds to the third grid element (its midpoint is at 50 pixel from the sun's position). Concerning the size of the grid elements, the authors found that a smaller dimension (10x10 pixels) gave too erratic results and a larger dimension did not yield any noticeable forecasting difference. The calculation of the error in the direct normal irradiance forecast is evaluated through the Root-Means-Squared Errors (RMSEs). In particular, to compare the cloud fractions with DNI values, the following equation is applied:

$$X_i(t)' = DNI_{max}(1 - X_i(t)) \tag{5.14}$$

where each variable of the grid for a given time step $X_i(t)$ is subtracted from 1 because of the inverse relationship between cloud fraction and DNI intensity and the DNI_{max} is the maximum DNI of the analysed period (within this study is set at 900 W/m^2). The RMSE for each variable and for each

forecasting horizon is defined as:

$$RMSE(\Delta t, i) = \sqrt{1/N \sum_{t \in T} (DNI(t+\Delta t) - X_i(t)')^2} \tag{5.15}$$

The authors also considered the persistence forecast because they claimed that is the simplest forecasting model available and can be remarkably accurate (in the statistical sense) for short term horizons. In [83] the RMSE of the persistence model is used to represent the variability of the solar irradiance and in [84] the authors claimed that, when the variability is low, an appropriately defined persistence model produces very accurate forecast and therefore any forecast model which shows improvement over the persistence is improving the estimation over random variability. The RMSE for the persistence is:

$$RMSE_p(\Delta t) = \sqrt{1/N \sum_{t \in T} (DNI(t+\Delta t) - DNI(t))^2} \tag{5.16}$$

The RMSE errors are calculated for each variable X_i at different forecasting horizons and their evaluation demonstrate that the presented methodology is useful for 3-15 minutes ahead forecasting horizons and, comparing with a persistent model, it appears that the most significant forecast accuracies are for 5 minutes ahead. Furthermore, this methodology propose to focus on the ability to identify the preferential cloud motion and process the information quickly contained in the image, for this reason it may not be strictly applicable to cases where distinct cloud layers move in different directions, especially if these situations occur frequently, and it presents main weaknesses in case of steady state cloud cover.

5.2 Results and further research

The research activity on the solar predictor can be subdivided in four stages:

1. Image acquisition through a camera
2. Acquired images analysis, this stage is composed of 3 different studies:
   (a) Image elaboration,
   (b) Cloudy shape detection,
   (c) Motion estimation and tracking
3. Hourly-forecast of solar radiation on the PV system
4. Validation of the prototype through the evaluation of the prediction error

5.2.1 Images analysis and Cloudy shape detection

This part of the research project carried out many trials to find a reliable and easy solution to use for image processing by the use of two software: LabView and MatLab.

- LabView (Vision package): "NI Vision Assistant" is a package of LabView software widely used for acquisition, analysis and image processing. The package provides some functions for pre-processing, those used in this project are:
  - *Extraxt HSL*
  - *Threshold*
- MatLab (Image Processing Toolbox): This toolbox of Matlab is widely used for pre-processing and image processing. Features designed for image processing using this toolbox are:
  - *Impixelinfo*
  - *Edge*
  - *Labelmatrix*
  - *Imsubtract*

Extraxt HSL-LabView

The *extraxt HSL* function is able to convert an RGB image in a HSL image (Hue Saturation Brightness), the image is thus "broken" in 3 levels: plane Hue (Hue), Saturation plane (saturation) and Brightness plane (brightness). In this case it was decided to process the image in the brightness level, Figure 5.10, to be able to apply the THRESHOLD function. The *threshold* function selects a certain range of values

(a) Original image *(b) Brightness Plane.*

Figure 5.10: Extraxt HSL function for image elaboration

of pixels in an image in gray scale (in this case Brightness plane) and creates a chromatic division between the areas which lie above and below the set threshold. The threshold can be set manually or by automatic functions. In this case it has chosen a threshold automatic call "Local Threshold: Background correction" that among all able to better identify the portion of the sky and divide it by cloudy mantle. The result of applying this function can be observed in Figure 5.11.

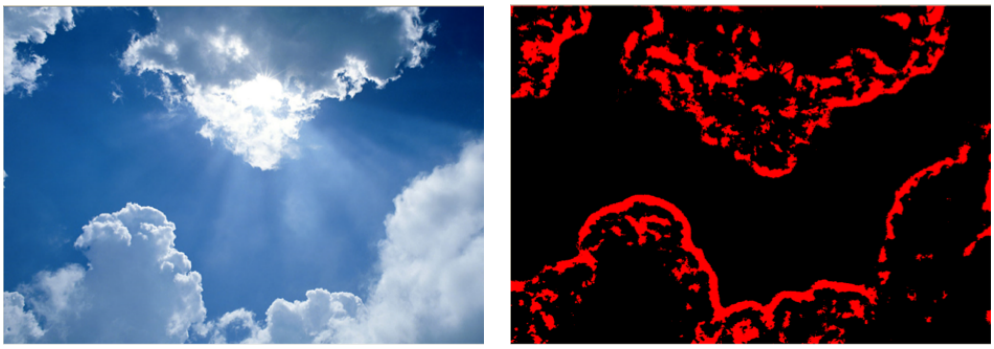

(a) Original image *(b) Brightness Plane.*

Figure 5.11: Local Threshold, Background correction for Brightness Plane

A second image has been considered to apply the*extraxt HSL* function to extract the Saturation Plane.

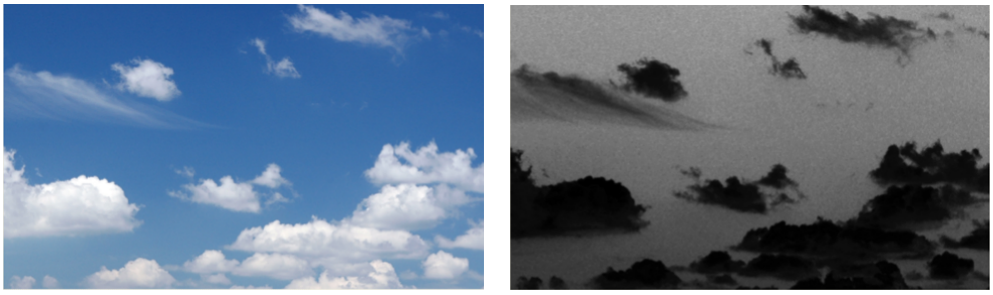

(a) Original image *(b) Saturation Plane.*

Figure 5.12: Extraxt HSL function for image elaboration, image 2

Threshold-LabView

Once the saturation level is obtained, two different thresholds can be applied to for image processing: "Manual threshold" (in Figure 5.12b is set at 52) and the "Local Threshold: Background correction". Both methods give good results in the identification of cloudy mantles, as can be seen in Figure 5.13.

Impixelinfo - MatLab

The *impixelinfo* function creates an information panel where you can see the pixel values for each point by moving the cursor over the image. This function can be applied on different types of image: RGB, grayscale and binary image. As can be seen from Figure 5.14 Three different sky images have

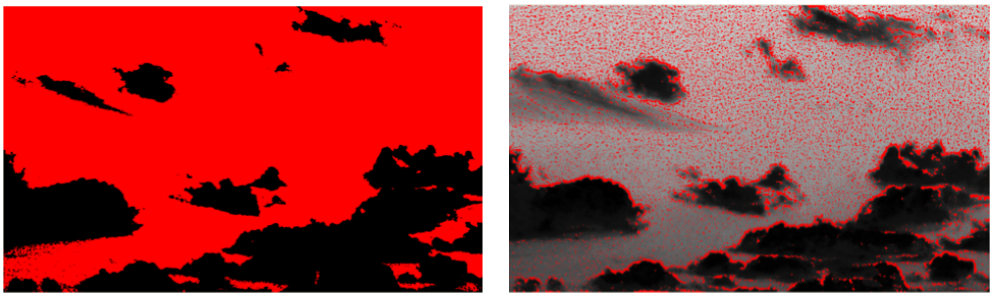

(a) Manual Threshold *(b) Local Threshold, Background correction*

Figure 5.13: Manual and Local Threshold for Saturation Plane

been considered, the first with the absence of direct sunlight, the second and the third with direct sunlight in different weather conditions.

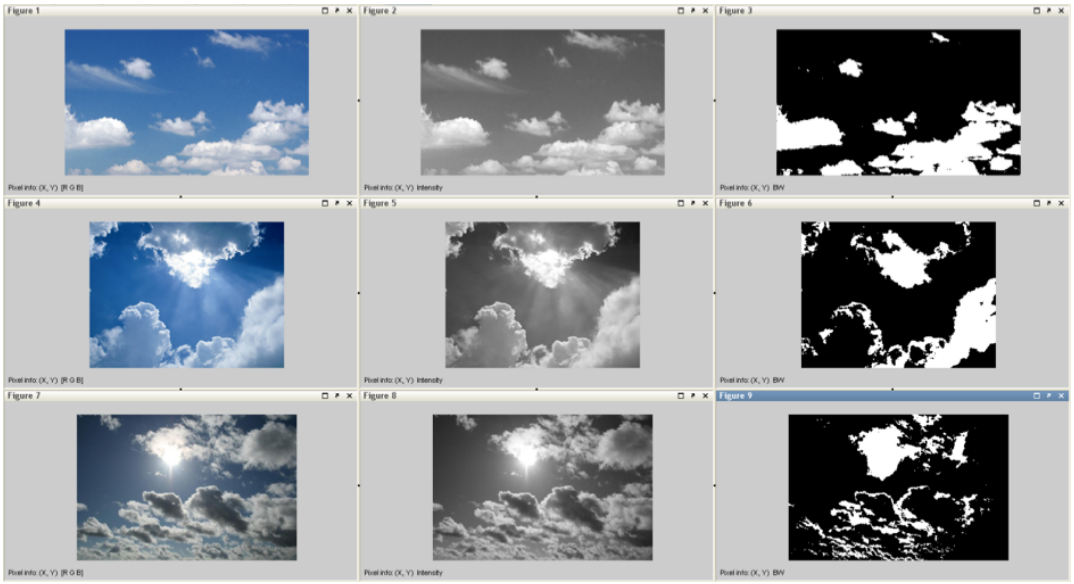

Figure 5.14: Impixelinfo function

In Figure 5.15a and Figure 5.15b it is possible to see that in the case of a grayscale image of the grey values assume a range of values from 0 to 255 (0 = black, 255 = white). The higher values of intensity will have for the clouds while lower values for the portions of the sky. In Figure 5.15a the cursor (red dot) is located on the portion of the sky, and the pixel value is 92, and Figure 5.15b the cursor is located on a portion of the cloud and the pixel value is 216. In the case of binary image the possible values of the individual pixels are further reduced to 0 and 1 (0 = black, 1 = white) as can be seen from Figure 5.16a and Figure 5.16b. In many binary images it is possible to get a value of zero in

(a) Sky grey values *(b) Clouds grey values*

Figure 5.15: Impixelinfo on grey scale image

the portion of the sky and equal to 1 in the portion of the cloud.

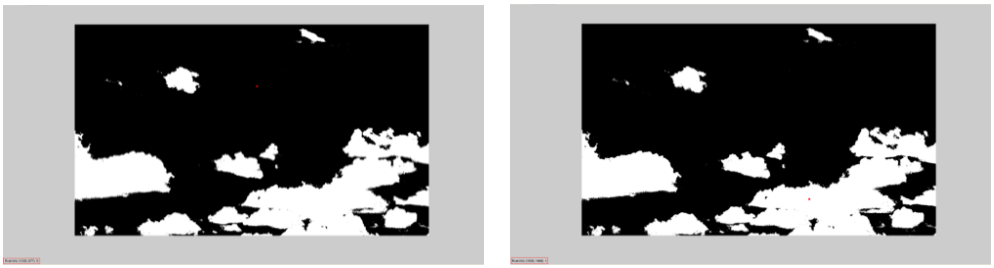

(a) Sky grey values *(b) Clouds grey values*

Figure 5.16: Impixelinfo on binary image

The *impixelinfo* function appears to give excellent results of distinction cloud-sky for images where this is not a high degree of solar refraction. As can be seen from Figure 5.14 the third analysed image, where the solar refraction is very clear and the color scale of the cloudy mantle assumes very different values (it changes from white to dark grey due to shading), this system is not able to distinguish with accuracy the sky and those portions of the cloudy mantle, as can be observed in detail in Figure 5.17a and Figure 5.17b.

Edge- MatLab

Concerning the *edge* function, the purpose of this system is to identify the "edges" of the objects within the image to be able to divide the cloudy layer from the sky and study its shape. To implement the *edge* function is necessary to pre-process the image as this function can only read in grayscale images or binary images. Figure 5.18 illustrates the processing of the image to the original (top left), grayscale (upper right), grayscale adjusted with the "contrast sterch" (bottom left), and finally the binary image in black and white (bottom right).

Once the image has been processed, the *edge* function can be implemented. The method used by

(a) *Original image* (b) *Binary image*

Figure 5.17: Impixelinfo on high solar refraction image

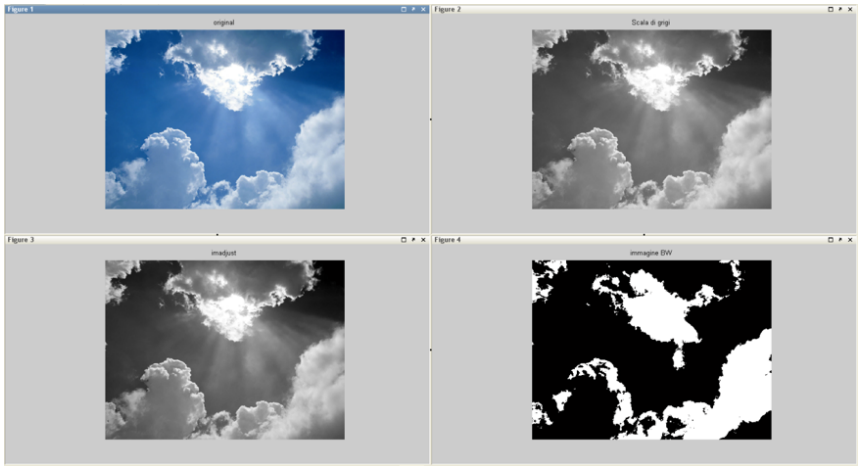

Figure 5.18: Edge function, image pre-processing

this function is not unique, there are six different methods to find the "edges" within an image. The methods used by this function are the following:

- Sobel method
- Prewitt method
- Roberts method
- Laplacian of Gaussian
- Zero-cross method
- Canny method

Each of these methods adopt a different evaluation to determine the contour points within the image. All the six methods have been applied to different "cloudy sky images" to find the method

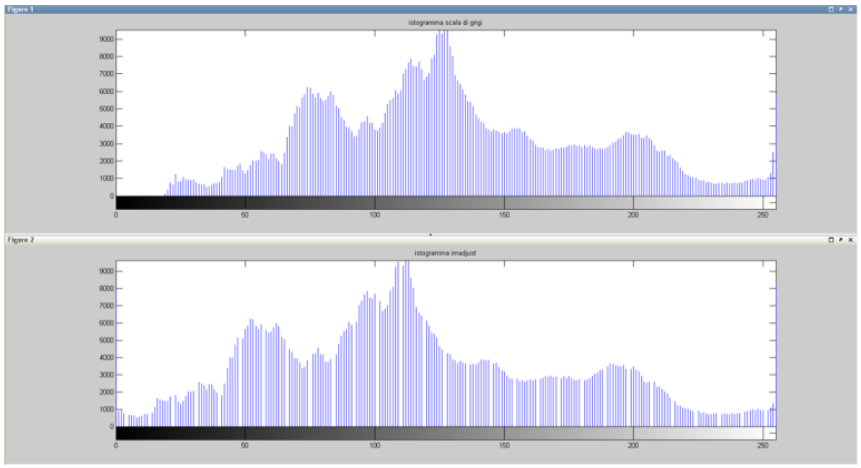

Figure 5.19: Edge function, Histogram of image pre-processing

that best analyses and recognises images of this type. In Figures 5.20 and 5.21 are exposed all the six methods applied to the grayscale "adjusted" and the binary image, respectively.

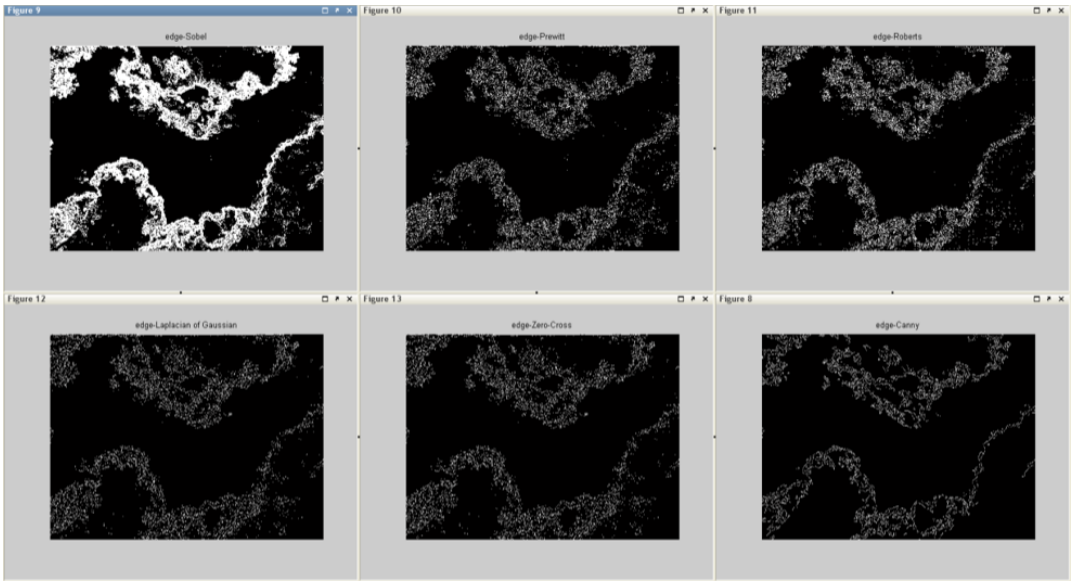

Figure 5.20: Edge function, grey scale "adjusted" images

The methods are very similar, especially in the analysis of the image binary. The method that among all seems to be the most effective is the Sobel method when applied to the image to grayscale "adjusted". As can be seen in Figure 5.20 at the top left the contours of the cloudy layer are well defined and fairly accurately correspond to the visible contours in the original image (Figure 5.18). A second method that could be taken into account is the Canny method (widely used in the literature)

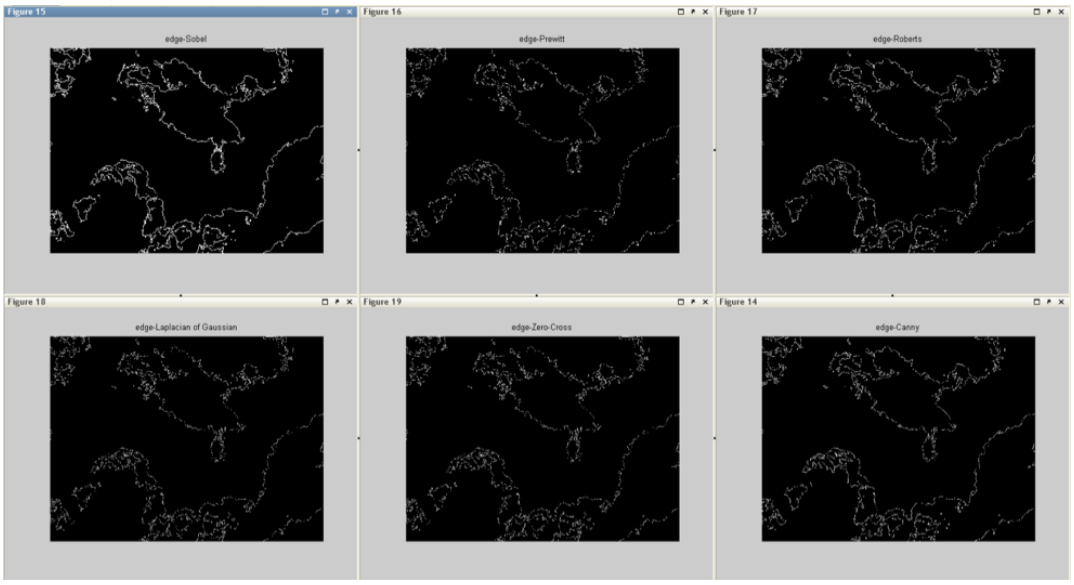

Figure 5.21: Edge function, binary images

that can be observed in the lower right in Figure 5.20. This method generates outlines of the very "clean" and well defined than the other methods. To test the validity of the *edge* function different images have been analysed. A second example of this application can be seen in Figure 5.22 which shows the original image, the Sobel and Canny method applied to the image in grayscale "adjusted".

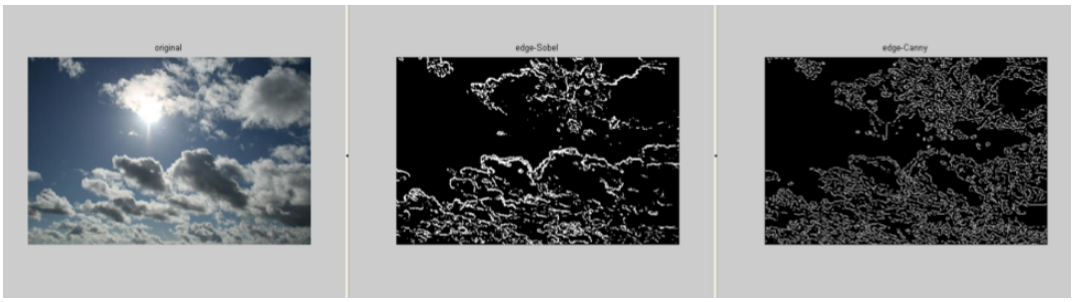

Figure 5.22: Edge function, Sobel and Canny methods

Labelmatrix - MatLab

Concerning the *labelmatrix* algorithm, the original image has been processed through the use of some functions:

1. *Im2bw* function: The original image has been "turned" into a binary image in black and white, see Figure 5.23.

2. *Bwareaopen* function: it remove from the binary image all the objects connected each other that present a small difference in pixel values, producing a "cleaner" second binary image.
3. *Bwconncomp* function: creates a matrix CC where the elements connected to the original binary image after the cleaning process are combined.
4. *Labelmatrix* function: it starts from a matrix CC and creates a matrix L whose elements are integer values greater than or equal to zero. The pixels equal to zero represents the background. The pixels having the value of 1 represent an object, those that have value equal to 2 representing a second object, and so on, see Figure 5.24
5. *Label2RGB* function: it starts from the matrix L and transforms the binary image in a 'color image (RGB) where the background (pixels = 0) remains in a fixed color, which in this case is black was chosen, and the remaining pixels with a value greater than zero is associated with a certain color on the basis of a choice of "colormap" available in the Toolbox of MatLab. See Figure 5.25

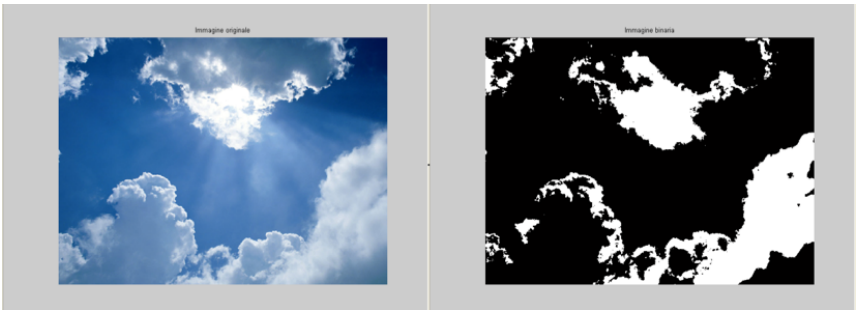

Figure 5.23: IM2BW function

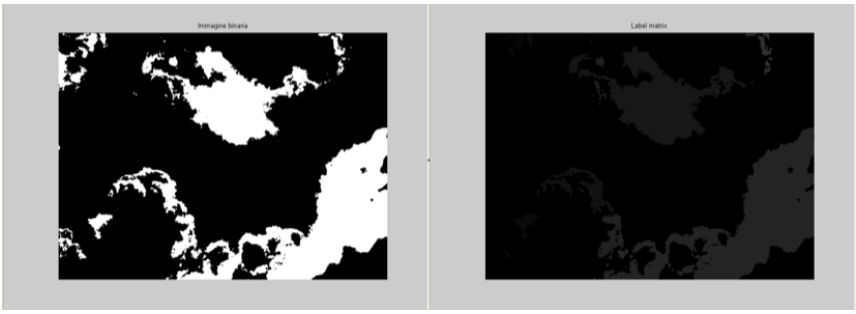

Figure 5.24: Labelmatrix function

The series of above as functions has also been applied to a second image of cloudy sky with no direct sunlight. The results, which can be observed in Figure 5.26 appear best respects to the first case and objects (clouds) appear distinct and defined.

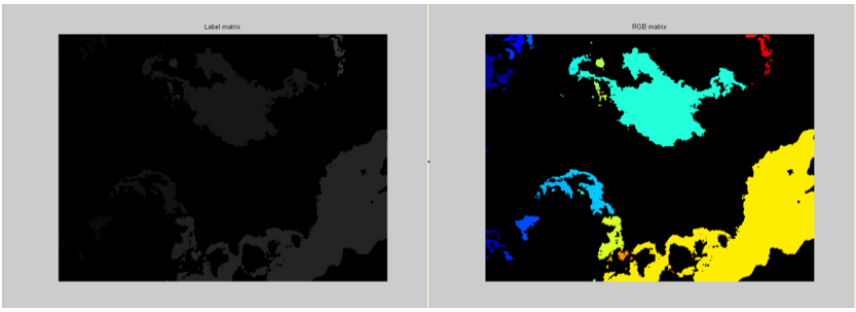

Figure 5.25: Label2RGB function

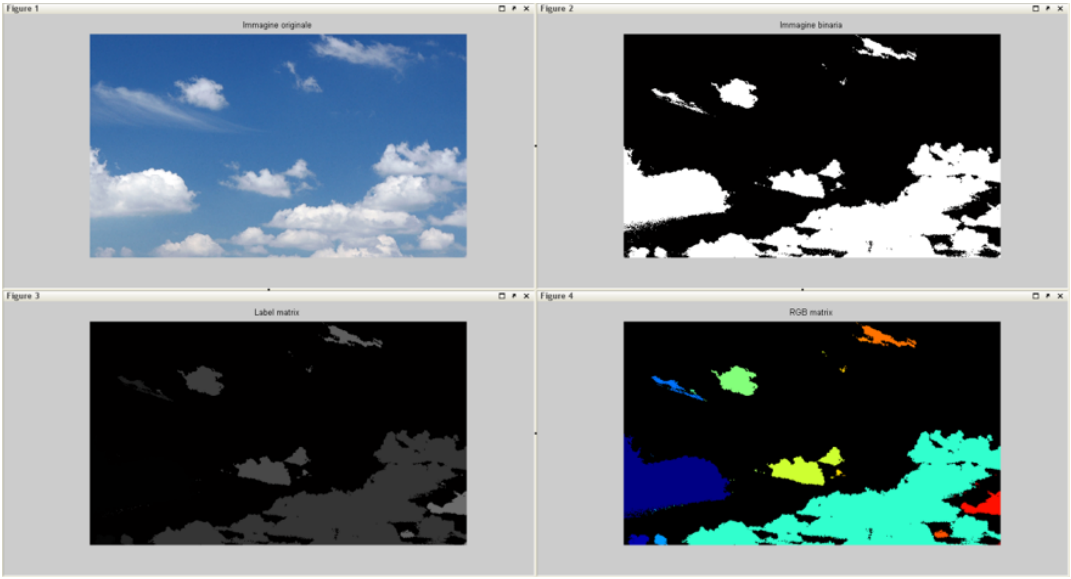

Figure 5.26: Label2RGB function, absence of direct sunlight

Imsubtract - MatLab

Imsubtract is a function of Image Processing Toolbox for Matlab that allows to cut the parts of an image that result to be different as compared to a second image. The idea is to use the image of a portion of clear sky (total absence of clouds) and compare it with an image of the same portion in different weather conditions (presence of clouds) to obtain a third image composed only of the clouds. The basic concept of the function is to consider the values of pixels, from 0 to 255, contained in the considered two images and isolate the resulting values differ between the two. The concept is further clarified by the histograms of the images considered and found to be that which can be observed in Figure 5.27.

The final goal of this first step is therefore to obtain a matrix (view image as a matrix) where the sky (background) assumes a constant value (equal to 0) and the cloudy mantle assumes variable

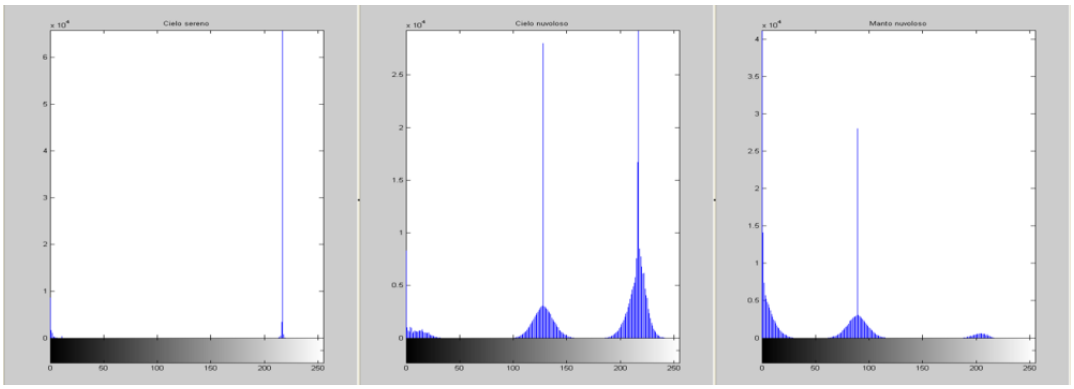

Figure 5.27: Imsubtract function, histogram

values (0 to 255) on the basis the intensity of the same cloud; in this way it is possible to classify the different types of cloud and study for which values overcast bodies are more or less intense and at what height are positioned with respect to the acquisition system. The methods outlined above have shown advantages and disadvantages according to the type of image used. One conclusion of this study is that a possible union of different methods could generate more satisfactory results; one of these could be the union of the EDGE method and the LABELMATRIX method, or implement the function IMSUBTRACT with real images and with a pre-treatment of the image to be able to "isolate" the cloudy mantle. The use of "Labview" software could also be more thorough (as a secondary road) to find further solutions.

5.2.2 Motion estimation and tracking

Once the cloud and its shape is identified, the second step of elaborating images concerns in estimate the motion of the cloud, its direction and velocity, and, eventually, to track it and make an estimation on where will move in a certain time period. This step has been analysis through two different MatLab functions: *MatchingPoints* and *Motion Based Multiple Object Tracking*.
The first method is shown in Figure 5.28 and it consists in comparing two images of the same cloud taken with a time step of 2 minutes. The algorithm is able to identify the "matching points" of the same cloud in the two different images. Using the time step as input data, the algorithm can evaluate the velocity of the cloud and its direction. Since clouds move fast and their shape is permanently changing, the faster motion of the cloud, the shorter time step has to be chosen between two sequential images.

Another interesting algorithm is called *Motion Based Multiple Object Tracking* and its application on cloud motion can be observed in Figure 5.29

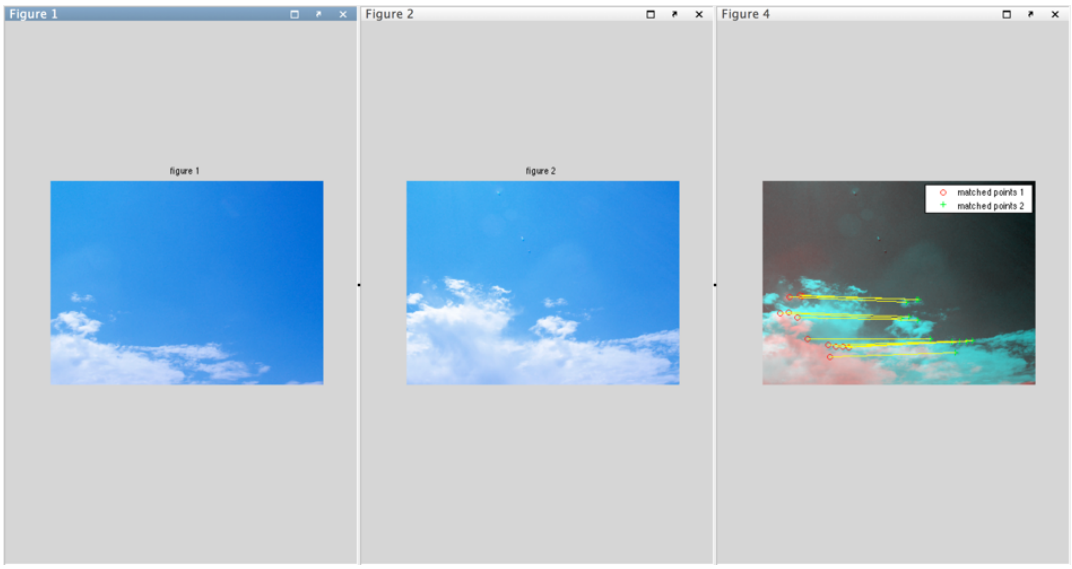

Figure 5.28: Motion estimation and tracking

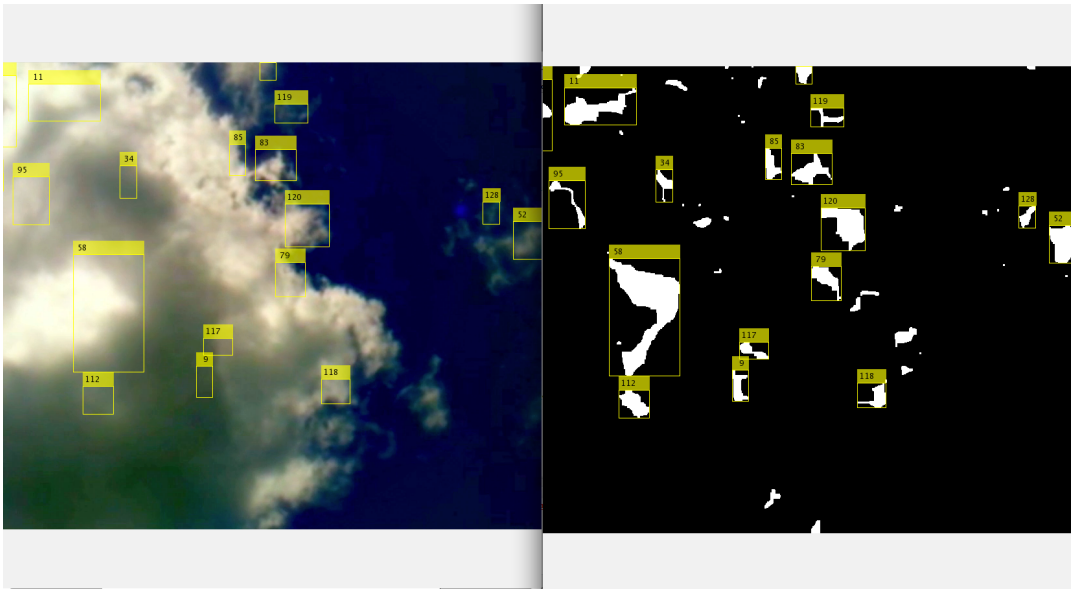

Figure 5.29: MultiObjectTracking

5.2.3 Prediction of available solar radiation

Once that the velocity and direction of the cloud motion is identified, its trajectory is compared to the sun daily path. In order to evaluate the sun motion during a day, some parameters are needed:

- Delclination, δ. Introduced in Chapter 2 by Equation (2.5)
- Zenith Angle, θ_z. Introduced in Chapter 2 by Equation (2.13)
- Hour angle, ω. Introduced in Chapter 2
- Solar altitude angle, α_s
- Solar azimuth angle, γ_s

The Solar altitude angle, α_s is the angle between the horizontal and the line to the sun, that is, the complement of the zenith angle and can be defined from Equation (2.13):

$$\cos\theta_z = \sin(90 - \theta_z) = \sin\alpha_s \tag{5.17}$$

$$\alpha_s = \sin^{-1}(\cos\phi\cos\delta\cos\omega + \sin\phi\sin\delta) \tag{5.18}$$

The solar azimuth angle, γ_s, is the angular displacement from south of the projection of beam radiation on the horizontal plane. Displacements east of south are negative and west of south are positive. γ_s can have values in the range of +180° to 180°. For north or south latitudes between 23.45° and 66.45°, γ_s will be between 90° and 90° for days less than 12 h long; for days with more than 12 h between sunrise and sunset, γ_s will be greater than 90° or less than 90° early and late in the day when the sun is north of the east-west line in the northern hemisphere or south of the east-west line in the southern hemisphere. For tropical latitudes, γ_s can have any value when $\delta - \phi$ is positive in the northern hemisphere or negative in the southern, for example, just before noon at $\phi = 10$ and $\delta = 20$, $\gamma_s = -180$, and just after noon $\gamma_s = +180$. Thus γ_s is negative when the hour angle is negative and positive when the hour angle is positive. The sign function in Equation (5.19) is equal to +1 if ω is positive and is equal to 1 if ω is negative:

$$\gamma_s = \text{sign}(\omega)\left|\cos^{-1}\left(\frac{\cos\theta_z\sin\phi - \sin\delta}{\sin\theta_z\cos\phi}\right)\right| \tag{5.19}$$

Through the equations shown above and in Chapter 2, the sun trajectory is exactly defined for any point in time, every day of the year at a particular latitude, ϕ, declination δ, and hour angle ω. The sun position is identified by the parameters: the zenith angle θ_z, the solar altitude angle α_s and the solar azimuth angle γ_s. A solar position plot of θ_z and α_s versus γ_s for latitudes of ±45° can be observed in Figure 5.30, where lines of constant declination are labeled by dates of mean days of the months from Table 5.1. Figure 5.30 shows the lines of constant hour angles labeled by hours.

Once the sun trajectory is exactly known at any time, the next step is to interpolate the data of the estimated cloud position in a certain time and the sun position at that time. In order to interpolate the

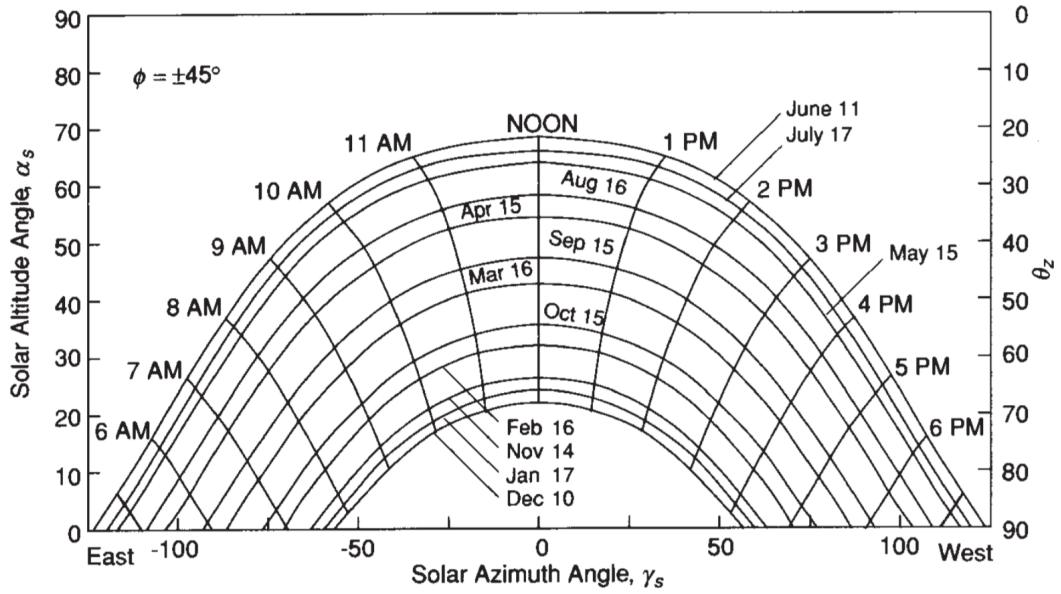

Figure 5.30: Solar position plot for ±45 latitude. Solar altitude angle and solar azimuth angle are functions of declination and hour angle, indicated on the plot by dates and times. The dates shown are for northern hemisphere

Table 5.1: Average days for months and values of n by months

Month	Day of the Month	For Average Day of the Month		
		Date	n	δ
January	i	17	17	-20.9
February	$31+i$	16	47	-13.0
March	$59+i$	16	75	-2.4
April	$90+i$	15	105	9.4
May	$120+i$	15	135	18.8
June	$151+i$	11	162	23.1
July	$181+1i$	17	198	21.2
August	$212+i$	16	228	13.5
September	$243+i$	15	258	2.2
October	$273+i$	15	288	-9.6
November	$304+i$	14	318	-18.9
December	$334+i$	10	344	-23.0

trajectories, data concerning the exact position of the clouds is needed, and this would be possible by the use of professional instrumentation able to give as the image and evaluate at the same time the position of the cloud (altitude and azimuth angles).
If the predicted path of the cloud does not intersect with the trajehe sun, the available solar radiation will be evaluated with equations of Chapter 2. If the predicted path of the cloud will intersect the sun trajectory, the available solar radiation at that time will be estimated considering a lower value of the previous situation and the decreasing percentage will depend on the type of cloud.
The suitable equipment to carry out this evaluation is a camera developed by the Yankee Enviromental Systems, called Total Sky Imager (TSI) and used by many authors previously cited.

5.2.4 Further work

The solar prediction could be a pivotal tool in an hybrid energy system and it could lead to a reduction in peak loads, cost of energy and increase of RE fraction. Some prototypes already exist and have been presented in the cited works but currently the accuracy and reliability of these instruments is not high enough to predict the solar radiation (and the PV plants production) within a useful time step and in any weather conditions. The further step of the presented research will be to carry out tests on images captured with the professional instrumentation mentioned in the previous paragraph and to get experimental results to validate and improve the current work.

6

Conclusion and future research

The issue of RES fluctuation and the inability of programming their production, generated a wide scientific research field on RES penetration, but how this objective can be reached in the future and what the future power system will look like is, however, not fully clear. Concerning the smart-grid system and implementation of RETs, part of this thesis project pointed out how important is to be able to design energy systems based on the real request of supplied energy and to maximise the self consumption of energy decreasing the costs of grid duties and avoiding imbalance in the grid, especially during the distribution phase.

The software presented within this PhD thesis project is able to design hybrid energy systems composed of photovoltaic plant, storage and backup systems in any location of the world, able improve the reliability, availability and sustainability of both grid-connected and isolated energy systems. Energy hybrid systems are best suited to reduce dependence on fossil fuel by using available solar radiation in both on-grid and off-grid systems.

The reason behind the project is that an optimum combination of the hybrid energy system components provides higher system performance than a single system, for the same component cost and lifetime. It was also observed that the capacity of the storage system has an important bearing on the system performance of single PV energy system and an optimised design can be pivotal in the system cost reduction. It can be claimed that the storage system increases the flexibility of system control and adds to overall system availability.

Furthermore, one of the elements that may be useful to reach the goal of improving the system energy efficiency is the development of an instrument able to make a reliable prediction of PV production. Meteorological conditions are decisive in solar plant management and electricity generation. Any increases or decreases in solar radiation mean a plant has to adapt its operation method to the climato-

logical phenomena. An unexpected atmospheric change can provoke a range of problems related to various solar plant components affecting the electricity generation system and, in consequence, causing alterations in the electricity grid. Therefore, predicting atmospheric features is key to managing solar plants and is therefore necessary for correct electrical grid management. For large scale solar applications, the amount of irradiance reaching the ground surface is most strongly affected by clouds, aerosols and water vapour column, with cloud effects being particularly dominant for most locations where solar power is currently produced.

Making prediction on photovoltaic production, storage operating life, diesel cost, interest rate trend, and electric load demand over a period of 20-25 years seems ambitious and far from reliable results. Indeed the aim of the project strived for achieving optimal solution for renewable energy systems considering every current economical, social, geographical, and political factor without keeping out the possibility to conform the energy system with future requirements. For instance the project does not exclude the chance to extend the current system with modular system parts in order to satisfy a potential higher electric demand or to substitute system components with more advanced and high efficient ones. Concerning political factor, i.e. diesel cost and interest rate, sensitivity analysis has been carried out at the end of the study in order to understand the impact of these critical parameters variation on the optimal proposed model. Furthermore, compared to the past studies, this work analyses the power system by running a 15 minutes step simulation for one year, in order to evaluate the supply reliability of the system within shorter time step, and therefore to investigate the renewable energy (RE) criticality.

The project has presented an interesting case study of a village in Uganda located in an isolated and remote area not reached by the electricity grid. The EHS software has been used to design an off-grid hybrid energy system for this village and to compare the current energy situation of the village with the proposed one. The results of the case study disclose that the optimal combination of PV array, electric storage and back-up system, despite its high investment cost, is the most convenient. The hybrid system presents a reduction in both total costs and fuel consumption compared with the PV-diesel generators and only diesel generators system. This conclusion leads the authors to claim that the electric storage is a fundamental tool to take advantage of renewable and not programmable energy sources, to reduce power production costs (22.2%) and drastically decreasing the fuel consumption (77%), especially in isolated areas where the over- produced power can not be put into the grid and it is wasted. These results are obtained at the current interest rate and diesel price of Uganda; in order to observe if the hybrid system is still economically advantageous compare to the usage of a generators only at the variation of these unpredictable parameters, sensitivity analysis is implemented on the interest rate variation and diesel price increase during the lifetime of the system. Results show also in this case that the hybrid system solution is still a cheaper solution. Sensitivity analysis is further carried out to observe the effect of a different investment cost of the electrical storage and its lifetime. The decrease in the lifetime of the storage presents a higher TLCC but still lower than the TLCC of the system without storage. On the other hand the capital cost of the battery bank seems to

influence significantly the cost of the system and the hybrid system with storage is not longer the most advantageous configuration when the capital cost of the battery bank is 3 times the cost considered within the present study. This parameter is therefore crucially important and it has to be chosen property during the dimensioning process. A potential further development of the presented thesis is the introduction of micro-wind turbines contribution to the presented hybrid power system with PV, storage and diesel generators and to observe the changes of total cost of the system, fuel consumption and storage effect. Furthermore, the hypothesis of simulating the same daily load profile for 25 years implies that any increase in the electric devises number involves an extension of the load demand and therefore the inability of the hybrid system to entirely supply the village load. The purpose of the presented study is indeed to achieve a dimensioning approach of a power system able to satisfy a current load without keeping out the possibility to extend the current system with modular system parts in order to satisfy a potential higher electric demand.

In order to implement the efficiency of the hybrid system, a methodology to predict and to take advantage of solar radiation has been proposed. It has been shown that the application of automatic digital image-processing techniques on sky images is a useful method to complement, or even replace, traditional human observations of sky cover, and there is likely potential for inferring cloud type. Although many uncertainty exists in fractional sky cover retrievals from sky images, previous work has shown this uncertainty is no greater than that attached to human observations for the commercially available sky imager and processing technique. Unlike human observations, current sky condition descriptions from digital images do not include cloud typing in the traditional way (using cloud genera). However, other equally interesting, for solar radiation studies, sky characteristics can be implied, such as cloud brokenness and distinction between optically thin and thick clouds. Within this project a sky image system , based on a commercial digital camera, has been used and characterised with respect to get image elaboration, cloudy shape detection, and motion estimation and tracking. The further step of the presented research will be to carry out tests on images captured with the professional instrumentation mentioned in the previous paragraph and to get experimental results to validate and improve the current work. The presented software analyses the power of a hybrid system by running a 15 minutes step simulation for one year, in order to evaluate the supply reliability of the system within shorter time step, and therefore to investigate the renewable energy (RE) criticality. The choice of the short time interval is moreover strictly connected with the potential implementation of a solar predictor within the hybrid system, able to forecast the weather conditions within short time period and to supply pivotal information to the final users concerning an optimal usage of stored energy.

6 Conclusion and future research

Bibliography

[1] D. Puig and T. C. Farrell. *The Multiple Benefits of Measures to Improve Energy Efficiency: A Summary Report*. 2015.

[2] J. P. Painuly. "Barriers to renewable energy penetration; a framework for analysis". In: *Renewable energy* 24.1 (2001), pp. 73–89.

[3] *https://ec.europa.eu/energy/en/topics/renewableenergy*.

[4] B. V. Mathiesen, H. Lund, and K. Karlsson. "100% Renewable energy systems climate mitigation and economic growth". In: *Applied Energy* 88.2 (2011), pp. 488–501.

[5] B. Ćosić, G. Krajačić, and N. Duić. "A 100% renewable energy system in the year 2050: The case of Macedonia". In: *Energy* 48.1 (2012), pp. 80–87.

[6] H. Lund and B. V. Mathiesen. "Energy system analysis of 100% renewable energy systems—The case of Denmark in years 2030 and 2050". In: *Energy* 34.5 (2009), pp. 524–531.

[7] G. Krajačić, N. Duić, Z. Zmijarević, B. V. Mathiesen, A. A. Vučinić, and M. da Graça Carvalho. "Planning for a 100% independent energy system based on smart energy storage for integration of renewables and CO 2 emissions reduction". In: *Applied thermal engineering* 31.13 (2011), pp. 2073–2083.

[8] D. Connolly and B. V. Mathiesen. "A technical and economic analysis of one potential pathway to a 100% renewable energy system". In: *International Journal of Sustainable Energy Planning and Management* 1 (2014), pp. 7–28.

[9] D. Connolly, H. Lund, B. V. Mathiesen, and M. Leahy. "The first step towards a 100% renewable energy-system for Ireland". In: *Applied Energy* 88.2 (2011), pp. 502–507.

[10] H. Lund, A. N. Andersen, P. A. Ostergaard, B. V. Mathiesen, and D. Connolly. "From electricity smart grids to smart energy systems–a market operation based approach and understanding". In: *Energy* 42.1 (2012), pp. 96–102.

[11] H. Ryu, S. Dorjragchaa, Y. Kim, and K. Kim. "Electricity-generation mix considering energy security and carbon emission mitigation: Case of Korea and Mongolia". In: *Energy* 64 (2014), pp. 1071–1079.

[12] P. Meibom, R. Barth, B. Hasche, H. Brand, C. Weber, and M. O'Malley. "Stochastic optimization model to study the operational impacts of high wind penetrations in Ireland". In: *IEEE Transactions on Power Systems* 26.3 (2011), pp. 1367–1379.

[13] I. Mason, S. Page, and A. Williamson. "A 100% renewable electricity generation system for New Zealand utilising hydro, wind, geothermal and biomass resources". In: *Energy Policy* 38.8 (2010), pp. 3973–3984.

[14] G. Krajačić, N. Duić, and M. da Graça Carvalho. “How to achieve a 100% RES electricity supply for Portugal?” In: *Applied energy* 88.2 (2011), pp. 508–517.

[15] B. Elliston, M. Diesendorf, and I. MacGill. “Simulations of scenarios with 100% renewable electricity in the Australian National Electricity Market”. In: *Energy Policy* 45 (2012), pp. 606–613.

[16] M. Z. Jacobson and M. A. Delucchi. “Providing all global energy with wind, water, and solar power, Part I: Technologies, energy resources, quantities and areas of infrastructure, and materials”. In: *Energy Policy* 39.3 (2011), pp. 1154–1169.

[17] F. Orecchini and A. Santiangeli. “Beyond smart grids–the need of intelligent energy networks for a higher global efficiency through energy vectors integration”. In: *International Journal of hydrogen energy* 36.13 (2011), pp. 8126–8133.

[18] C. Clastres. “Smart grids: Another step towards competition, energy security and climate change objectives”. In: *Energy Policy* 39.9 (2011), pp. 5399–5408.

[19] M. Wissner. “The Smart Grid–A saucerful of secrets?” In: *Applied Energy* 88.7 (2011), pp. 2509–2518.

[20] P. Bajpai and V. Dash. “Hybrid renewable energy systems for power generation in stand-alone applications: a review”. In: *Renewable and Sustainable Energy Reviews* 16.5 (2012), pp. 2926–2939.

[21] A. Chauhan and R. Saini. “A review on integrated renewable energy system based power generation for stand-alone applications: configurations, storage options, sizing methodologies and control”. In: *Renewable and Sustainable Energy Reviews* 38 (2014), pp. 99–120.

[22] F. Mwasilu, J. J. Justo, E.-K. Kim, T. D. Do, and J.-W. Jung. “Electric vehicles and smart grid interaction: A review on vehicle to grid and renewable energy sources integration”. In: *Renewable and Sustainable Energy Reviews* 34 (2014), pp. 501–516.

[23] U. K. Debnath, I. Ahmad, D. Habibi, and A. Y. Saber. “Energy storage model with gridable vehicles for economic load dispatch in the smart grid”. In: *International Journal of Electrical Power & Energy Systems* 64 (2015), pp. 1017–1024.

[24] F. Fattori, N. Anglani, and G. Muliere. “Combining photovoltaic energy with electric vehicles, smart charging and vehicle-to-grid”. In: *Solar Energy* 110 (2014), pp. 438–451.

[25] M. Jentsch, T. Trost, and M. Sterner. “Optimal use of power-to-gas energy storage systems in an 85% renewable energy scenario”. In: *Energy Procedia* 46 (2014), pp. 254–261.

[26] P. A. Ostergaard. “Transmission-grid requirements with scattered and fluctuating renewable electricity-sources”. In: *Applied Energy* 76.1 (2003), pp. 247–255.

[27] P. A. Ostergaard. “Modelling grid losses and the geographic distribution of electricity generation”. In: *Renewable Energy* 30.7 (2005), pp. 977–987.

[28] A. Kylili and P. A. Fokaides. “European smart cities: The role of zero energy buildings”. In: *Sustainable Cities and Society* 15 (2015), pp. 86–95.

[29] P. D. Lund, J. Mikkola, and J. Ypyä. “Smart energy system design for large clean power schemes in urban areas”. In: *Journal of Cleaner Production* 103 (2015), pp. 437–445.

[30] H. Lund, A. Marszal, and P. Heiselberg. “Zero energy buildings and mismatch compensation factors”. In: *Energy and Buildings* 43.7 (2011), pp. 1646–1654.

[31] A. J. Lamadrid. “Optimal use of energy storage systems with renewable energy sources”. In: *International Journal of Electrical Power & Energy Systems* 71 (2015), pp. 101–111.

[32] G. Graditi, M. G. Ippolito, E. Telaretti, and G. Zizzo. “An innovative conversion device to the grid interface of combined RES-based generators and electric storage systems”. In: *IEEE Transactions on Industrial Electronics* 62.4 (2015), pp. 2540–2550.

[33] P. Fortenbacher, A. Ulbig, S. Koch, and G. Andersson. “Grid-constrained optimal predictive power dispatch in large multi-level power systems with renewable energy sources, and storage devices”. In: *IEEE PES Innovative Smart Grid Technologies, Europe*. IEEE. 2014, pp. 1–6.

[34] L. Dusonchet, M. Ippolito, E. Telaretti, G. Zizzo, and G. Graditi. “An optimal operating strategy for combined RES-based generators and electric storage systems for load shifting applications”. In: *Power Engineering, Energy and Electrical Drives (POWERENG), 2013 Fourth International Conference on*. IEEE. 2013, pp. 552–557.

[35] H. M. Al-Masri and M. Ehsani. “Feasibility investigation of a hybrid on-grid wind photovoltaic retrofitting system”. In: *IEEE Transactions on Industry Applications* 52.3 (2016), pp. 1979–1988.

[36] H. Gharavi and M. Ardehali. “Imperialist competitive algorithm for optimal design of on-grid hybrid green power system integrated with a static compensator for reactive power management”. In: *Journal of Renewable and Sustainable Energy* 5.1 (2013), p. 013115.

[37] M. Athari and M. Ardehali. “Operational performance of energy storage as function of electricity prices for on-grid hybrid renewable energy system by optimized fuzzy logic controller”. In: *Renewable Energy* 85 (2016), pp. 890–902.

[38] M. S. Adaramola, S. S. Paul, and O. M. Oyewola. “Assessment of decentralized hybrid PV solar-diesel power system for applications in Northern part of Nigeria”. In: *Energy for Sustainable Development* 19 (2014), pp. 72–82.

[39] M. S. Ngan and C. W. Tan. “Assessment of economic viability for PV/wind/diesel hybrid energy system in southern Peninsular Malaysia”. In: *Renewable and Sustainable Energy Reviews* 16.1 (2012), pp. 634–647.

[40] G. Dalton, D. Lockington, and T. Baldock. “Feasibility analysis of stand-alone renewable energy supply options for a large hotel”. In: *Renewable energy* 33.7 (2008), pp. 1475–1490.

[41] S. Rehman and L. M. Al-Hadhrami. “Study of a solar PV–diesel–battery hybrid power system for a remotely located population near Rafha, Saudi Arabia”. In: *Energy* 35.12 (2010), pp. 4986–4995.

[42] HOMER. *http://homerenergy.com*. 2015.

[43] HYBRIDS. *http://www.hybridsoftware.com*. 2015.

[44] F. Kemausuor, E. Adkins, I. Adu-Poku, A. Brew-Hammond, and V. Modi. “Electrification planning using Network Planner tool: The case of Ghana”. In: *Energy for Sustainable Development* 19 (2014), pp. 92–101.

[45] N. Agarwal, A. Kumar, et al. “Optimization of grid independent hybrid PVdieselbattery system for power generation in remote villages of Uttar Pradesh, India”. In: *Energy sustainable development* 17.3 (2013), pp. 210–219.

[46] R. Perez, S. Kivalov, J. Schlemmer, K. Hemker, D. Renné, and T. E. Hoff. “Validation of short and medium term operational solar radiation forecasts in the US”. In: *Solar Energy* 84.12 (2010), pp. 2161–2172.

[47] E. Lorenz, J. Hurka, D. Heinemann, and H. G. Beyer. “Irradiance forecasting for the power prediction of grid-connected photovoltaic systems”. In: *IEEE Journal of selected topics in applied earth observations and remote sensing* 2.1 (2009), pp. 2–10.

[48] P. Mathiesen and J. Kleissl. “Evaluation of numerical weather prediction for intra-day solar forecasting in the continental United States”. In: *Solar Energy* 85.5 (2011), pp. 967–977.

[49] M. Martinez-Chico, F. Batlles, and J. Bosch. “Cloud classification in a mediterranean location using radiation data and sky images”. In: *Energy* 36.7 (2011), pp. 4055–4062.

[50] J. Alonso, F. Batlles, G. Lopez, and A. Ternero. “Sky camera imagery processing based on a sky classification using radiometric data”. In: *Energy* 68 (2014), pp. 599–608.

[51] J. Alonso and F. Batlles. “Short and medium-term cloudiness forecasting using remote sensing techniques and sky camera imagery”. In: *Energy* 73 (2014), pp. 890–897.

[52] C. W. Chow, B. Urquhart, M. Lave, A. Dominguez, J. Kleissl, J. Shields, and B. Washom. “Intra-hour forecasting with a total sky imager at the UC San Diego solar energy testbed”. In: *Solar Energy* 85.11 (2011), pp. 2881–2893.

[53] R. Marquez and C. F. M. Coimbra. “Intra-hour DNI forecasting based on cloud tracking image analysis”. In: *Solar Energy* 91 (2013), pp. 327–336.

[54] P. Ferreira, J. Gomes, I. Martins, and A. Ruano. “A Neural Network Based Intelligent Predictive Sensor for Cloudiness, Solar Radiation and Air Temperature”. In: *Sensors* 12.11 (2012), pp. 15750–15777.

[55] M. Ghonima, B. Urquhart, C. Chow, J. Shields, A. Cazorla, and J. Kleissl. “A method for cloud detection and opacity classification based on ground based sky imagery”. In: *Atmospheric Measurement Techniques* 5.11 (2012), pp. 2881–2892.

[56] M. Souza-Echer, E. Pereira, L. Bins, and M. Andrade. “A simple method for the assessment of the cloud cover state in high-latitude regions by a ground-based digital camera”. In: *Journal of Atmospheric and Oceanic Technology* 23.3 (2006), pp. 437–447.

[57] A. Heinle, A. Macke, and A. Srivastav. “Automatic cloud classification of whole sky images”. In: *Atmospheric Measurement Techniques Discussions* 3.1 (2010), pp. 269–299.

[58] A. Kazantzidis, P. Tzoumanikas, A. Bais, S. Fotopoulos, and G. Economou. “Cloud detection and classification with the use of whole-sky ground-based images”. In: *Atmospheric Research* 113 (2012), pp. 80–88.

[59] M. Singh and M. Glennen. “Automated ground-based cloud recognition”. In: *Pattern analysis and applications* 8.3 (2005), pp. 258–271.

[60] J. A. Duffie and W. A. Beckman. *Solar engineering of thermal processes*. Third. John Wiley and Sons, 2006.

[61] D. Erbs, S. Klein, and J. Duffie. “Estimation of the diffuse radiation fraction for hourly, daily and monthly-average global radiation”. In: *Solar energy* 28.4 (1982), pp. 293–302.

[62] B. Y. Liu and R. C. Jordan. “The long-term average performance of flat-plate solar-energy collectors: with design data for the US, its outlying possessions and Canada”. In: *Solar Energy* 7.2 (1963), pp. 53–74.

[63] J. Durand, M. Duarte, P. Clerens, et al. *Joint EASE/EERA recommendations for a European energy storage technology development roadmap towards 2030*. Tech. rep. Brussels: EASE/EERA, 2013.

[64] J. Eyer and G. Corey. “Energy storage for the electricity grid: Benefits and market potential assessment guide”. In: *Sandia National Laboratories* 20.10 (2010), p. 5.

[65] J. Durand, M. Duarte, and P. Clerens. “European energy storage technology development roadmap towards 2030”. In: *European Association for Storage of Energy (EASE), European Energy Research Alliance (EERA)* (2013).

[66] B. Zakeri and S. Syri. “Electrical energy storage systems: A comparative life cycle cost analysis”. In: *Renewable and Sustainable Energy Reviews* 42 (2015), pp. 569–596.

[67] S. K. Fuller and S. R. Petersen. *Life-Cycle Costing Manual for the Federal Energy Management Program*. National Institute of Standards and Technology Handbook 135. 1996.

[68] PRAMAC. *http://www.pramac.com*. 2015.

[69] SO.DA. *http://www.soda-is.com*. 2015.

[70] I. Hadjipaschalis, A. Poullikkas, and V. Efthimiou. “Overview of current and future energy storage technologies for electric power applications”. In: *Renewable and Sustainable Energy Reviews* 13.6 (2009), pp. 1513–1522.

[71] S. J. Kazempour, M. P. Moghaddam, M. Haghifam, and G. Yousefi. “Electric energy storage systems in a market-based economy: Comparison of emerging and traditional technologies”. In: *Renewable Energy* 34.12 (2009), pp. 2630–2639.

[72] WorldBank. *http://data.worldbank.org*. 2015.

[73] C. Christodoulou, S. C. Michaelides, C. S. Pattichis, et al. “Multifeature texture analysis for the classification of clouds in satellite imagery”. In: *Geoscience and Remote Sensing, IEEE Transactions on* 41.11 (2003), pp. 2662–2668.

[74] G. Pfister, R. McKenzie, J. Liley, A. Thomas, B. Forgan, and C. N. Long. “Cloud coverage based on all-sky imaging and its impact on surface solar irradiance”. In: *Journal of Applied Meteorology* 42.10 (2003), pp. 1421–1434.

[75] C. N. Long, J. Sabburg, J. Calbo, and D. Pages. “Retrieving cloud characteristics from ground-based daytime color all-sky images”. In: *Journal of Atmospheric and Oceanic Technology* 23.5 (2006), pp. 633–652.

[76] G. Pankiewicz. “Pattern recognition techniques for the identification of cloud and cloud systems”. In: *Meteorological Applications* 2.3 (1995), pp. 257–271.

[77] P. M. Tag, R. L. Bankert, and L. R. Brody. “An AVHRR multiple cloud-type classification package”. In: *Journal of Applied Meteorology* 39.2 (2000), pp. 125–134.

[78] R. L. Bankert and R. H. Wade. “Optimization of an instance-based GOES cloud classification algorithm”. In: *Journal of applied meteorology and climatology* 46.1 (2007), pp. 36–49.

[79] A. Kreuter, M. Zangerl, M. Schwarzmann, and M. Blumthaler. “All-sky imaging: a simple, versatile system for atmospheric research”. In: *Applied optics* 48.6 (2009), pp. 1091–1097.

[80] J. E. Shields, M. E. Karr, R. W. Johnson, and A. R. Burden. “Day/night whole sky imagers for 24-h cloud and sky assessment: history and overview”. In: *Applied optics* 52.8 (2013), pp. 1605–1616.

[81] N. Mori and K.-A. Chang. “Introduction to MPIV”. In: *User manual and program available online at http://sauron. civil. eng. osaka-cu. ac. jp/˜ mori/softwares/mpiv* (2003).

[82] Q. Li, W. Lu, and J. Yang. “A hybrid thresholding algorithm for cloud detection on ground-based color images”. In: *Journal of atmospheric and oceanic technology* 28.10 (2011), pp. 1286–1296.

[83] T. E. Hoff and R. Perez. “Quantifying PV power output variability”. In: *Solar Energy* 84.10 (2010), pp. 1782–1793.

[84] R. Marquez and C. F. Coimbra. “Proposed metric for evaluation of solar forecasting models”. In: *Journal of solar energy engineering* 135.1 (2013), p. 011016.